Phase Transitions and Magnetic Properties of Transition Metal Based Magnetocaloric Materials

Gai, H.

DOI
10.4233/uuid:07e1fac3-ae48-4677-8557-693bbb6bbe64

Important note
To cite this publication, please use the final published version (if applicable).
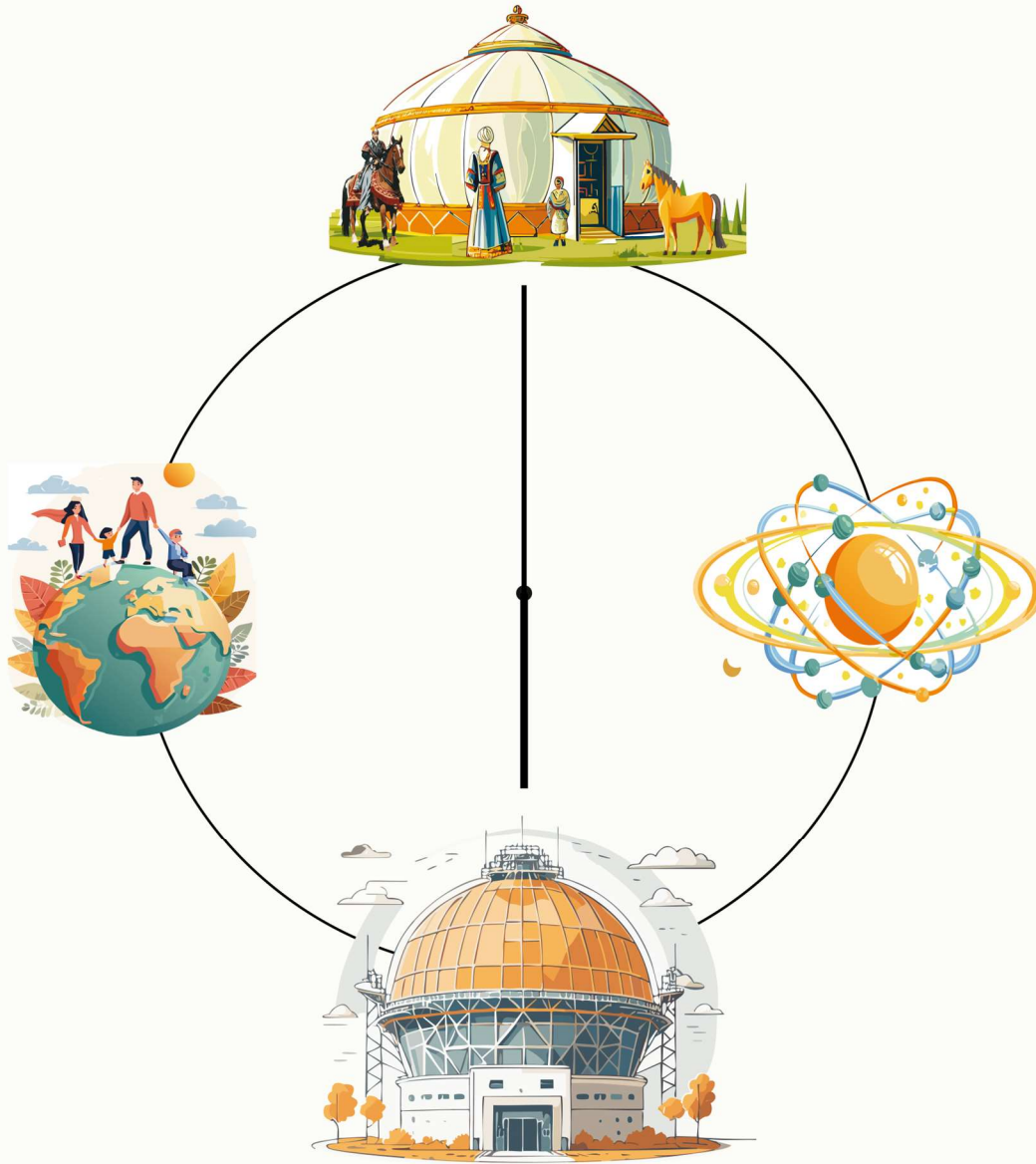Please check the document version above.

Phase Transitions and Magnetic Properties of Transition Metal Based Magnetocaloric Materials

Hanggai

Phase Transitions and Magnetic Properties of Transition Metal Based Magnetocaloric Materials

Phase Transitions and Magnetic Properties of Transition Metal Based Magnetocaloric Materials

Dissertation

for the purpose of obtaining the degree of doctor at

Delft University of Technology by the authority of the Rector Magnificus
prof.dr.ir. T.H.J.J. van der Hagen,

chair of the Board for Doctorates

to be defended publicly on

Monday 23 June 2025 at 12:30

by

HANGGAI

Master of Science in Condensed State Physics,

Inner Mongolia Normal University, China

born in Inner Mongolia, China

Keywords: Magnetocaloric effect, magnetic materials, phase transition, magnetic structures, magnetic cooling, heat capacity.

Dedicated to my family

Propositions

Accompanying the dissertation

Phase Transitions and Magnetic Properties of Transition Metal Based Magnetocaloric Materials

by

HANGGAI

1. Clear goals and timelines are key to stay on track during a PhD.

2. We must prioritize solving the mechanical stability issues of $(Mn,Fe)_2(P,Si)$ materials to facilitate their transition from lab research to practical applications. (this thesis)

3. The development of new materials hinges not only on their innovative properties, but also on their scalability and environmental sustainability.

4. Unveiling the physical insights of existing materials yields more impact than the pursuit of entirely novel ones. (this thesis)

5. Understanding the interplay between micro- and macroscopic properties is crucial to unlocking the full potential of functional materials. (this thesis)

6. Exploring novel materials offers great potential, but often requires a significantly larger time investment than anticipated. (this thesis)

7. Being a good supervisor means helping students to make the right decisions at the right time.

8. Pursuing a PhD is not just an academic endeavour but a journey of self-discovery.

9. Failed experiments are invaluable, as they provide critical lessons on how to refine future approaches and avoid repeating mistakes.

10. Nervousness is not a weakness, but a signal of self-improvement in progress.

These propositions are regarded as opposable and defendable, and have been approved as such by the promoters Dr.ir. N.H. van Dijk and Prof. dr. E.H. Brück.

Contents

Chapter 1

Introduction

Efficient energy utilization has been central to human progress, with each new energy source driving societal and technological advancements. While fossil fuels like coal, oil, and natural gas currently dominate, their environmental impact and finite availability underscore the urgent need for sustainable alternatives. Developing environmentally friendly and efficient energy conversion processes is vital to addressing the challenges of resource scarcity and climate change.

Magnetocaloric materials (MCMs) are at the forefront of research in advanced cooling technologies due to their ability to exhibit a magnetocaloric effect (MCE). This area of study holds both significant fundamental scientific interest and critical application potential. From a scientific point of view, MCMs are highly intriguing due to their ability to exhibit a giant magnetocaloric effect (GMCE). Uncovering the underlying mechanisms of first-order magnetic transitions (FOMT) plays a pivotal role in advancing research and development in this field [1–6]. From an application perspective, related research primarily focuses on developing 3D-printed bulk materials to achieve gradient composites manufacturing of MCMs with enhanced heat transfer coefficients [7]. This approach is particularly relevant given the narrow operating range of FOMTs, which necessitates multiple material layers to achieve optimal efficiency [8]. However, for the successful commercialization of magnetic cooling and heat pump technologies, the primary future challenge lies in ensuring mechanical stability of GMCMs, which is a critical prerequisite.

This thesis explores the unique structure and thermomagnetic properties of Fe_2P-based and potential novel MCM systems using techniques such as magnetization, heat capacity, Mössbauer spectroscopy, Density Functional Theory (DFT), X-ray and neutron diffraction.

1.1 Magnetocaloric Effect

The conventional magnetocaloric effect (MCE) is an intrinsic magneto-thermodynamic phenomenon that couples a change in the magnetic field with a corresponding temperature change in a material, thereby enabling magnetic refrigeration technologies [1,9–17]. The magnetocaloric effect was observed in 1917 by Weiss and Piccard, who reported a 0.7 K temperature increase in a nickel sample subjected to a 1.5 T magnetic field near its Curie temperature ($T_C = 627$ K) [18]. The theoretical foundations of the MCE were subsequently derived by Debye in 1926 [19] and Giauque in 1927 [20]. In 1933, Giauque and MacDougall [21] experimentally achieved magnetic cooling with a reduction in temperature to a lowest temperature of 0.25 K, demonstrating the practical application of the phenomenon. This groundbreaking application of the MCE earned Giauque the Nobel Prize in Chemistry in 1949 and remains one of the most widely used techniques for achieving temperatures below 10 mK. The MCE enables advancements in magnetic refrigeration and related applications, including magnetic cooling, magnetic heat pumps, and thermomagnetic energy harvesting.

To achieve a significant MCE for room temperature applications, it is essential to leverage the entropy anomaly associated with a magnetic transition. The MCE can thus be effectively represented using an entropy-temperature (S-T) diagram. Fig. 1.1 illustrates the total entropy as a function of temperature for the ferromagnetic (FM) to paramagnetic (PM) transition. The application of a magnetic field promotes the formation of the ferromagnetic phase, resulting in a significant net magnetization change during the PM-to-FM transition. Consequently, the temperature increases under an applied magnetic field and decreases when the magnetic field is removed. This process depends on whether the magnetic field is applied under adiabatic or isothermal conditions. The magnitude of the MCE is characterized by two key parameters: the adiabatic temperature change (ΔT_{ad}) and the isothermal entropy change (ΔS). These parameters are critical for evaluating the potential applications of MCMs. To optimize their performance, it is essential to maximize these values in the vicinity of the magnetic phase transition, ideally occurring near room temperature.
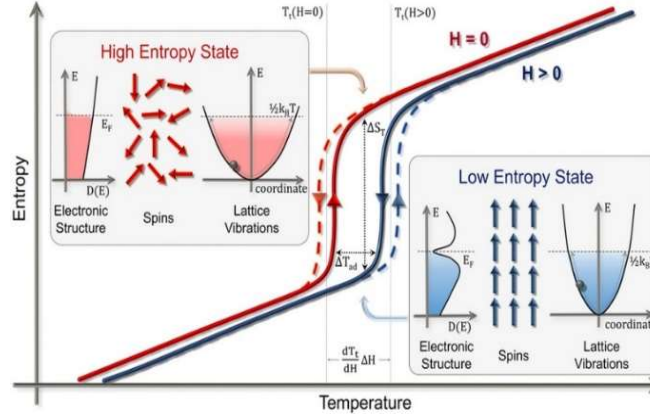
Fig. 1.1. Schematic *S-T* diagram representing a Brayton cycle for the magnetic phase transition materials (with a ferromagnetic-to-paramagnetic transition) [22].

1.2 Classification of Phase Transitions in Magnetocaloric Materials

The nature of the phase transition is a critical parameter for magnetocaloric materials. Magnetic materials can be classified into two types based on the nature of their phase transitions: first-order magnetic phase transition (FOMT) and second-order magnetic phase transition (SOMT). The distinction between FOMT and SOMT is determined by the presence or absence of latent heat. In FOMTs, latent heat amplifies the entropy anomaly at the magnetic phase transition, resulting in a giant magnetocaloric effect (GMCE). Although FOMTs are relatively rare, their occurrence can be induced in a limited number of systems by coupling a structural or elastic transition with a magnetic transition. Depending on their intrinsic physical properties, magnetocaloric materials with a FOMT can be further classified into two types: those associated with a change in crystalline structure, referred to as magneto-structural transitions, and those where the lattice symmetry remains unchanged, known as magneto-elastic transitions. FOMT materials generally exhibit large isothermal entropy changes, that are often associated with a significant thermal hysteresis (ΔT_{hys}). In contrast, SOMT materials display an absence of ΔT_{hys}, but typically also show lower isothermal entropy changes. Ideally, MCMs tailored for practical applications should exhibit transitions without ΔT_{hys}, while maintaining a high isothermal entropy change and a large adiabatic temperature change. However, achieving this combination is highly challenging. Therefore, materials tuned to a state at the border between a FOMT and a SOMT, referred to as the critical point, exhibit a low ΔT_{hys}, while maintaining a high entropy change, representing an effective compromise that leverages the advantages of both types of phase transitions. The distinction between a FOMT and a SOMT is based on the presence of a

3

discontinuity either in the first derivatives or the second derivatives of the Gibbs free energy (G), which will be discussed in the next chapter.

1.3 Scope of Magnetocaloric Materials and Related Applications

Magnetocaloric materials can be classified into two categories based on their operating temperature range: cryogenic magnetocaloric materials (MCMs) and high-temperature MCMs. Low-temperature MCMs primarily consist of binary rare-earth-based intermetallic compounds (e.g., RGa, RNi, RZn, RSi, R_3Co and R_{12}Co$_7$) [23,24], which exhibit low-temperature phase transitions. Additionally, rare-earth-transition metal-main group metal ternary compounds (e.g., RTSi, RTAl, RT_2Si$_2$, RCo$_2$B$_2$ and RCo$_3$B$_2$) [25], where R denotes a rare-earth element and T represents a transition metal. These materials typically exhibit a second-order magnetic transition (SOMT) and are known for their excellent thermal and magnetic reversibility, as well as their high thermal conductivity.

Since the 1990s, research on room-temperature MCMs has received significant attention, driven both by their potential applications and the scientific interest in uncovering the underlying physical mechanisms of the giant magnetocaloric effect (GMCE). The rare-earth element gadolinium (Gd) has been widely used in magnetocaloric refrigeration due to its second order magnetic phase transition temperature T_C near room temperature and its notable ΔT_{ad} values of 2.6 K and 4.0 K for magnetic field changes of 1.0 and 1.5 T, respectively [26,27]. However, the limited availability and high cost of Gd restrict its practical applications. In 1997, Pecharsky and Gschneidner discovered a giant magnetocaloric effect in the Gd-based compound Gd$_5$(Si,Ge)$_4$ [28], demonstrating ΔT_{ad} values approximately 30% higher than that of Gd. Moreover, the T_C of this compound can be tuned by varying the Si/Ge ratio. This compound serves as a prototypical example of magneto-structural transition materials. In addition to Gd$_5$(Si,Ge)$_4$, several other examples exhibiting magneto-structural transitions include NiMn-based Heusler alloys [29,30], MnAs [31], and MnCoGeB [32,33].

Magneto-elastic transitions are characteristic for Fe$_2$P alloys [11], La(Fe,Si)$_{13}$ [34] and FeRh [35] alloys. In 2002 Tegus et al. [1] reported the discovery of a GMCE in the Fe$_2$P-based (Mn,Fe)$_2$(P,As) compound. This material demonstrated a remarkable performance and a wide operational temperature range, with its T_C tuneable between 160 and 340 K via chemical substitution. However, to address the necessity of eliminating the toxic element arsenic, researchers investigated alternative (Mn,Fe)$_2$(P,X) compounds, where X represents Ge or Si. This effort led in 2007 to the identification of second-generation (Mn,Fe)$_2$(P,Ge) compounds and in 2008 to third-generation

(Mn,Fe)$_2$(P,Si) compounds [36,37]. Based on their optimal working temperature range and potential MCE performance current research primarily focusses on household and commercial cooling applications in the vicinity of room temperature. However, to date, only two GMCE systems; (Mn,Fe)$_2$(P,Si) compounds and La(Fe,Si)$_{13}$ compounds are undergoing the required scaling-up processes. Current efforts are focused on using 3D-printing techniques to develop the manufacturing process for gradient composites of MCMs with enhanced heat transfer coefficients [7]. At the same time, the poor mechanical stability of the present material systems remains a major challenge. This thesis aims to identify novel materials to further optimize the performance of MCE materials for magnetic cooling and magnetic heat pump applications.

1.4 Potential Novel Magnetocaloric Materials Identified from Computational Calculations

This thesis explores the YNi$_{4-x}$Co$_x$Si and (Mn,Fe)$_3$Sn systems as promising candidates for novel magnetocaloric materials (MCMs), based on computational searches [38]. These systems are expected to offer significant potential for MCM applications. Rare-earth alloys demonstrate the potential to exhibit both a large magnetocaloric effect and hard magnetic properties [39–41]. The $R M_4$Si alloys, where R represents a rare-earth element (e.g., La, Tb, Gd, Y, Tm) and M is a 3d transition-metal element (e.g., Fe, Co, Ni), form a diverse family of materials with intriguing physical properties, including giant magnetic coercivity, a substantial magnetocaloric effect, and excellent hydrogen storage capabilities [42]. The hexagonal CaCu$_5$-type structure (space group $P6/mmm$) formed in some of these alloys can undergo a hexagonal-to-orthorhombic distortion, forming the orthorhombic YNi$_4$Si-type lattice (space group $Cmmm$). This structural transition represents a potential pathway for optimizing the magnetocaloric effect [43].
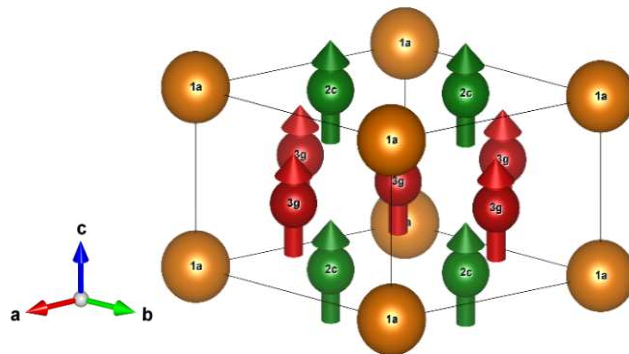
Fig. 1.2. Hexagonal unit cell of Y(Ni,Co)$_4$Si with the CaCu$_5$-type structure (space group $P6/mmm$), with arrows representing ferromagnetic (FM) moments aligned along the c axis.

Density functional theory (DFT) calculations predicted that the Heusler alloy $(Mn,Fe)_3Sn$ is a promising MCE material for magnetic heat pump and thermomagnetic motor applications [44–50]. These alloys exhibit relatively high magnetic moments and transition temperatures near room temperature, which can be continuously tuned by adjusting the Mn/Fe ratio [51]. According to the binary Mn-Sn and Fe-Sn phase diagrams the Mn_3Sn and Fe_3Sn compounds both crystallize in the hexagonal Mg_3Cd-type structure [52–55]. However, the spin structures of these two compounds differ: on the Mn-rich side, the spin configuration exhibits antiferromagnetic ordering, while on the Fe-rich side, the spin configuration transitions to ferromagnetic ordering. The Mg_3Cd-type crystal structure with $P6_3/mmc$ symmetry (space group 194) is composed of two layers, each containing three magnetic (Mn, Fe) atoms at the $6h$ site and one non-magnetic Sn atom at the $2d$ site of the hexagonal unit cell [56,57]. The magnetic atoms are arranged in a triangle in each layer [56], as show in Fig. 1.3.
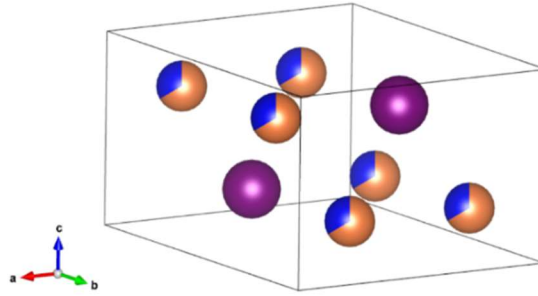
Fig. 1.3. Hexagonal unit cell of $(Mn,Fe)_3Sn$ with the Mg_3Cd-type structure (space group $P6_3/mmc$). Mn and Fe atoms are distributed across the $6h$ magnetic site, while Sn atoms occupy the nonmagnetic $2d$ site.

1.5 Thesis Outline

The aim of this thesis is to optimize and examine the structural and thermo-magnetic properties of Fe_2P-based materials, as well as novel MCMs such as Si-based $Y(Ni,Co)_4Si$ and Sn-based $(Mn,Fe)_3Sn$.

Chapter 2 presents the theoretical background related to the magnetocaloric effect, components of heat capacity in MCMs, as well as the thermodynamic properties near a magnetic phase transition based on the Landau theory.

Chapter 3 presents a brief overview of the experimental methods, experimental techniques and characterization methods.

Chapter 4 presents the preparation and calorimetric measurements of the giant magnetocaloric Fe-rich $(Mn,Fe)_2(P,Si)$ ribbons and bulk. This study focuses on the investigation of the microstructure in ribbon samples and on heat capacity

6

measurements using relaxation techniques to separate the latent heat of the Fe-rich $(Mn,Fe)_2(P,Si)$ compounds, which were then scaled with the transformation strain energy.

Chapter 5 is bridging the gap between microscopic and macroscopic descriptions of the first-order magneto-elastic field-induced transition in $(Mn,Fe)_2(P,Si)$ compounds. We investigated the field-induced transition in the first-order magneto-elastic ferromagnetic transition of a polycrystalline Fe_2P-based $Mn_{0.60}Fe_{1.30}P_{0.66}Si_{0.34}$ sample. To uncover the underlying mechanisms connecting the microscopic and macroscopic physical properties during the field-induced transition, we performed comprehensive simultaneous experiments, including X-ray magnetic circular dichroism (XMCD) measurements combined with simultaneous Hall probe magnetometry, magnetostriction and bulk SQUID magnetometry.

Chapter 6 presents structural and magnetic properties of $YNi_{4-x}Co_xSi$ alloys. In this study we systematically investigated the magnetic properties, as well as the crystal and magnetic structure of novel MCMs, Si-based $YNi_{4-x}Co_xSi$ compounds. A combination of oriented-powder X-ray and free-powder neutron diffraction experiments confirmed the simple ferromagnetic structure, with spins aligned along the hexagonal *c* axis. Magnetic measurements performed on field-oriented polycrystalline materials were used to calculate the magnetocrystalline anisotropy constants K_1 and K_2.

Chapter 7 explores the complex spin structure and magnetic phase transitions of $(Mn,Fe)_3Sn$ compounds. This chapter focuses on characterizing the phase transitions, the nature of the magnetic order, and the magnetocaloric effect in $Mn_{3-x}Fe_xSn$ compounds. The study identified the intricate temperature dependent spin configuration of the Mn_2FeSn compound. A low-temperature transition at T_S is attributed to a spin reorientation. Below T_S, both ferromagnetic (FM) and antiferromagnetic (AFM) contribution form a combined homogeneous state. Above T_S, the spin structure rearranges into a FM configuration with spins oriented in the *a-b* plane.

A summary, acknowledgments, a list of publications, and a brief curriculum vitae are included at the conclusion of this thesis.

References

[1] O. Tegus, E. Brück, K.H.J. Buschow, F.R. De Boer, Transition-metal-based magnetic refrigerants for room-temperature applications, Nature 415 (2002) 150–152. https://doi.org/10.1038/415150a.

[2] E. Liu, W. Wang, L. Feng, W. Zhu, G. Li, J. Chen, H. Zhang, G. Wu, C. Jiang, H. Xu, F. De Boer, Stable magnetostructural coupling with tunable magnetoresponsive effects in hexagonal ferromagnets, Nat Commun 3 (2012) 873. https://doi.org/10.1038/ncomms1868.

[3] K. Klinar, J.Y. Law, V. Franco, X. Moya, A. Kitanovski, Perspectives and Energy Applications of Magnetocaloric, Pyromagnetic, Electrocaloric, and Pyroelectric Materials, Advanced Energy Materials 14 (2024) 2401739. https://doi.org/10.1002/aenm.202401739.

[4] J. Lyubina, R. Schäfer, N. Martin, L. Schultz, O. Gutfleisch, Novel Design of La(Fe,Si)$_{13}$ Alloys Towards High Magnetic Refrigeration Performance, Advanced Materials 22 (2010) 3735–3739. https://doi.org/10.1002/adma.201000177.

[5] F. Guillou, A.K. Pathak, D. Paudyal, Y. Mudryk, F. Wilhelm, A. Rogalev, V.K. Pecharsky, Non-hysteretic first-order phase transition with large latent heat and giant low-field magnetocaloric effect, Nat Commun 9 (2018) 2925. https://doi.org/10.1038/s41467-018-05268-4.

[6] S. Singh, L. Caron, S. W. D'Souza, T. Fichtner, G. Porcari, S. Fabbrici, C. Shekhar, S. Chadov, M. Solzi, C. Felser, Large Magnetization and Reversible Magnetocaloric Effect at the Second-Order Magnetic Transition in Heusler Materials, Adv. Mater. 28 (2016) 3321–3325. https://doi.10.1002/adma.201505571.

[7] L. Xie, C. Liang, Y. Qin, H. Zhou, Z. Yu, H. Chen, M. Z. Naeem, K. Qiao, Y. Wen, B. Zhang, G. Wang, X. Li, J. Liu, V. Franco, K. Chu, M. Yi, H. Zhang, High-Throughput Screening of High-Performance Magnetocaloric Materials by Gradient Additive Manufacturing, Adv. Funct. Mater. 2024, 2414441. https://doi.10.1002/adfm.202414441.

[8] D. Pineda Quijano, C. Infante Ferreira, E. Brück, Layering strategies for active magnetocaloric regenerators using MnFePSi for heat pump applications, Applied Thermal Engineering 232 (2023) 120962. https://doi.org/10.1016/j.applthermaleng.2023.120962.

[9] E. Brück, O. Tegus, D.T.C. Thanh, K.H.J. Buschow, Magnetocaloric refrigeration near room temperature (invited), Journal of Magnetism and Magnetic Materials 310 (2007) 2793–2799. https://doi.org/10.1016/j.jmmm.2006.10.1146.

[10] J.D. Moore, K. Morrison, K.G. Sandeman, M. Katter, L.F. Cohen, Reducing extrinsic hysteresis in first-order La(Fe,Co,Si)$_{13}$ magnetocaloric systems, Applied Physics Letters 95 (2009) 252504. https://doi.org/10.1063/1.3276565.

[11] N.H. Dung, Z.Q. Ou, L. Caron, L. Zhang, D.T.C. Thanh, G.A. De Wijs, R.A. De Groot, K.H.J. Buschow, E. Brück, Mixed Magnetism for Refrigeration and Energy Conversion, Advanced Energy Materials 1 (2011) 1215–1219. https://doi.org/10.1002/aenm.201100252.

[12] F. Guillou, G. Porcari, H. Yibole, N. van Dijk, E. Brück, Taming the first-order transition in giant magnetocaloric materials, Adv. Mater. 26 (2014) 2671–2675, https://doi.org/10.1002/adma.201304788.

[13] N.H. Dung, L. Zhang, Z.Q. Ou, E. Brück, Magnetoelastic coupling and magnetocaloric effect in hexagonal Mn–Fe–P–Si compounds, Scripta Materialia 67 (2012) 975–978. https://doi.org/10.1016/j.scriptamat.2012.08.036.

[14] O. Gutfleisch, T. Gottschall, M. Fries, D. Benke, I. Radulov, K.P. Skokov, H. Wende, M. Gruner, M. Acet, P. Entel, M. Farle, Mastering hysteresis in magnetocaloric materials, Phil. Trans. R. Soc. A. 374 (2016) 20150308. https://doi.org/10.1098/rsta.2015.0308.

[15] T. Gottschall, K.P. Skokov, M. Fries, A. Taubel, I. Radulov, F. Scheibel, D. Benke, S. Riegg, O. Gutfleisch, Making a Cool Choice: The Materials Library of Magnetic Refrigeration, Advanced Energy Materials 9 (2019) 1901322. https://doi.org/10.1002/aenm.201901322.

[16] V. Franco, J.S. Blázquez, J.J. Ipus, J.Y. Law, L.M. Moreno-Ramírez, A. Conde, Magnetocaloric effect: From materials research to refrigeration devices, Progress in Materials Science 93 (2018) 112–232. https://doi.org/10.1016/j.pmatsci.2017.10.005.

[17] V. Zverev, A.M. Tishin, Magnetocaloric Effect: From Theory to Practice, in: Reference Module in Materials Science and Materials Engineering, Elsevier, 2016: p. B9780128035818028137. https://doi.org/10.1016/B978-0-12-803581-8.02813-7.

[18] P. Weiss, A. Piccard, Le phénomène magnétocalorique, J. Phys. Theor. Appl. 7 (1917) 103–109. https://doi.org/10.1051/jphystap:019170070010300.

[19] P. Debye, Einige Bemerkungen zur Magnetisierung bei tiefer Temperatur, Annalen der Physik 386 (1926) 1154–1160. https://doi.org/10.1002/andp.19263862517.

[20] W.F. Giauque, A thermodynamic treatment of certain magnetic effects. A proposed method of producing temperatures considerably below 1° absolute, J Am Chem Soc 49 (1927) 1864-1870.

[21] W.F. Giauque, D.P. MacDougall, Attainment of Temperatures Below 1° Absolute by Demagnetization of $Gd_2(SO_4)_3 \cdot 8H_2O$, Phys. Rev. 43 (1933) 768–768. https://doi.org/10.1103/PhysRev.43.768.

[22] F. Scheibel, T. Gottschall, A. Taubel, M. Fries, K.P. Skokov, A. Terwey, W. Keune, K. Ollefs, H. Wende, M. Farle, M. Acet, O. Gutfleisch, M.E. Gruner, Hysteresis Design of Magnetocaloric Materials—From Basic Mechanisms to Applications, Energy Tech 6 (2018) 1397–1428. https://doi.org/10.1002/ente.201800264.

[23] L. Li, M. Yan, Recent progresses in exploring the rare earth based intermetallic compounds for cryogenic magnetic refrigeration, Journal of Alloys and Compounds 823 (2020) 153810. https://doi.org/10.1016/j.jallcom.2020.153810.

[24] Z.-J. Mo, J. Shen, L.-Q. Yan, C.-C. Tang, J. Lin, J.-F. Wu, J.-R. Sun, L.-C. Wang, X.-Q. Zheng, B.-G. Shen, Low field induced giant magnetocaloric effect in TmGa compound, Applied Physics Letters 103 (2013) 052409. https://doi.org/10.1063/1.4816729.

9

[25] L.-W. Li, Review of magnetic properties and magnetocaloric effect in the intermetallic compounds of rare earth with low boiling point metals, Chinese Phys. B 25 (2016) 037502. https://doi.org/10.1088/1674-1056/25/3/037502.

[26] S.G. Min, K.S. Kim, S.C. Yu, H.S. Suh, S.W. Lee, Magnetocaloric properties of $Gd_{1-x}B_x(x=0, 0.06, 0.09, 0.12)$ alloys, Journal of Magnetism and Magnetic Materials 303 (2006) e440–e442. https://doi.org/10.1016/j.jmmm.2006.01.075.

[27] A.M. Tishin, A.V. Derkach, Y.I. Spichkin, M.D. Kuz'min, A.S. Chernyshov, K.A. Gschneidner, V.K. Pecharsky, Magnetocaloric effect near a second-order magnetic phase transition, Journal of Magnetism and Magnetic Materials 310 (2007) 2800–2804. https://doi.org/10.1016/j.jmmm.2006.10.1056.

[28] V.K. Pecharsky, K.A. Gschneidner, Jr., Giant Magnetocaloric Effect in Gd_5 (Si_2Ge_2), Phys. Rev. Lett. 78 (1997) 4494–4497. https://doi.org/10.1103/PhysRevLett.78.4494.

[29] E. Liu, W. Wang, L. Feng, W. Zhu, G. Li, J. Chen, H. Zhang, G. Wu, C. Jiang, H. Xu, F. De Boer, Stable magnetostructural coupling with tunable magnetoresponsive effects in hexagonal ferromagnets, Nat Commun 3 (2012) 873. https://doi.org/10.1038/ncomms1868.

[30] K. Mandal, D. Pal, N. Scheerbaum, J. Lyubina, O. Gutfleisch, Magnetocaloric Effect in Ni–Mn–Ga Alloys, IEEE Trans. Magn. 44 (2008) 2993–2996. https://doi.org/10.1109/TMAG.2008.2002481.

[31] S. Gama, A.A. Coelho, A. De Campos, A.M.G. Carvalho, F.C.G. Gandra, P.J. Von Ranke, N.A. De Oliveira, Pressure-Induced Colossal Magnetocaloric Effect in MnAs, Phys. Rev. Lett. 93 (2004) 237202. https://doi.org/10.1103/PhysRevLett.93.237202.

[32] T. Krenke, E. Duman, M. Acet, E.F. Wassermann, X. Moya, L. Mañosa, A. Planes, Inverse magnetocaloric effect in ferromagnetic Ni–Mn–Sn alloys, Nature Mater 4 (2005) 450–454. https://doi.org/10.1038/nmat1395.

[33] W. Hanggai, O. Tegus, H. Yibole, F. Guillou, Structural and magnetic phase diagrams of $MnFe_{0.6}Ni_{0.4}(Si,Ge)$ alloys and their giant magnetocaloric effect probed by heat capacity measurements, Journal of Magnetism and Magnetic Materials 494 (2020) 165785. https://doi.org/10.1016/j.jmmm.2019.165785.

[34] E. Lovell, A.M. Pereira, A.D. Caplin, J. Lyubina, L. F. Cohen, Dynamics of the First-Order Metamagnetic Transition in Magnetocaloric $La(Fe,Si)_{13}$: Reducing Hysteresis, Adv. Energy Mater. 5 (2015) 1401639. https://doi.org/10.1002/aenm.201401639.

[35] G. Li, R. Medapalli, J.H. Mentink, R.V. Mikhaylovskiy, T.G.H. Blank, S.K.K. Patel, A.K. Zvezdin, Th. Rasing, E.E. Fullerton, A.V. Kimel, Ultrafast kinetics of the antiferromagnetic-ferromagnetic phase transition in FeRh, Nat Commun 13 (2022) 2998. https://doi.org/10.1038/s41467-022-30591-2.

[36] D.T. Cam Thanh, E. Brück, O. Tegus, J.C.P. Klaasse, K.H.J. Buschow, Influence of Si and Ge on the magnetic phase transition and magnetocaloric properties of MnFe(P,Si,Ge), Journal of Magnetism and Magnetic Materials 310 (2007) e1012–e1014. https://doi.org/10.1016/j.jmmm.2006.11.194.

[37] D. T. Cam Thanh, E. H. Brück, N. T. Trung, J. C. P. Klaasse, K. H. J. Buschow, Z. Q. Ou, O. Tegus, L. Caron, Structure, magnetism, and magnetocaloric properties of MnFeP$_{1-x}$Si$_x$ compounds. Journal of Applied Physics, 103 (2008) 07B318. https://doi.org/10.1063/1.2836958.

[38] I. Batashev, Rational approaches to the design of magnetocaloric materials, PhD thesis Delft University of Technology, 2022. https://doi.org/10.4233/UUID:0F2EE7C8-70D2-43B2-93E7-26A328DED3A9.

[39] J.M.D. Coey, Permanent magnets: Plugging the gap, Scripta Materialia 67 (2012) 524–529. https://doi.org/10.1016/j.scriptamat. 04 (2012) 036.

[40] J. Cui, M. Kramer, L. Zhou, F. Liu, A. Gabay, G. Hadjipanayis, B. Balasubramanian, D. Sellmyer, Current progress and future challenges in rare-earth-free permanent magnets, Acta Materialia 158 (2018) 118–137. https://doi.org/10.1016/j.actamat.2018.07.049.

[41] O. Gutfleisch, M.A. Willard, E. Brück, C.H. Chen, S.G. Sankar, J.P. Liu, Magnetic Materials and Devices for the 21st Century: Stronger, Lighter, and More Energy Efficient, Advanced Materials 23 (2011) 821–842. https://doi.org/10.1002/adma.201002180.

[42] A.V. Morozkin, A.V. Knotko, V.O. Yapaskurt, F. Yuan, Y. Mozharivskyj, R. Nirmala, New orthorhombic derivative of CaCu$_5$-type structure: RNi$_4$Si compounds (R=Y, La, Ce, Sm, Gd–Ho), crystal structure and some magnetic properties, Journal of Solid State Chemistry 208 (2013) 9–13. https://doi.org/10.1016/j.jssc.2013.09.036.

[43] A.V. Morozkin, F. Yuan, Y. Mozharivskyj, O. Isnard, Magnetic order of YNi$_4$Si-type TbNi$_4$Si, Journal of Magnetism and Magnetic Materials 368 (2014) 121–125. http://doi.org/10.1016/j.jmmm.2014.04.057.

[44] A. Karle, The thermomagnetic Curie-motor for the conversion of heat into mechanical energy, International Journal of Thermal Sciences 40 (2001) 834–842. https://doi.org/10.1016/S1290-0729(01)01270-4.

[45] C.S. Alves, F.C. Colman, G.L. Foleiss, G.T.F. Vieira, W. Szpak, Numerical simulation and design of a thermomagnetic motor, Applied Thermal Engineering 61 (2013) 616–622. https://doi.org/10.1016/j.applthermaleng.2013.07.053.

[46] L.D.R. Ferreira, C.V.X. Bessa, I. Da Silva, S. Gama, A heat transfer study aiming optimization of magnetic heat exchangers of thermomagnetic motors, International Journal of Refrigeration 37 (2014) 209–214. https://doi.org/10.1016/j.ijrefrig.2013.09.010.

[47] K. Murakami, M. Nemoto, Some experiments and considerations on the behavior of thermomagnetic motors, IEEE Trans. Magn. 8 (1972) 387–389. https://doi.org/10.1109/TMAG.1972.1067406.

[48] Y. Takahashi, T. Matsuzawa, M. Nishikawa, Fundamental performance of the disc-type thermomagnetic engine, Electrical Engineering Japan 148 (2004) 26–33. https://doi.org/10.1002/eej.10359.

[49] C.S. Alves, F.C. Colman, G.L. Foleiss, W. Szpak, G.T.F. Vieira, A.C. Bento, Simulation of solar Curie wheel using NiFe alloy and Gd, International Journal of Refrigeration 37 (2014) 215–222. https://doi.org/10.1016/j.ijrefrig.2013.09.031.

[50] Y.W. Yin, M. Raju, W.J. Hu, J.D. Burton, Y.-M. Kim, A.Y. Borisevich, S.J. Pennycook, S.M. Yang, T.W. Noh, A. Gruverman, X.G. Li, Z.D. Zhang, E.Y. Tsymbal, Q. Li, Multiferroic tunnel junctions and ferroelectric control of magnetic state at interface (invited), Journal of Applied Physics 117 (2015) 172601. https://doi.org/10.1063/1.4913753.

[51] M.R. Felez, A.A. Coelho, S. Gama, Magnetic properties of $Mn_{3-x}Fe_xSn$ compounds with tuneable Curie temperature by Fe content for thermomagnetic motors, Journal of Magnetism and Magnetic Materials 444 (2017) 280–283. https://doi.org/10.1016/j.jmmm.2017.08.028.

[52] E. Krén, J. Paitz, G. Zimmer, É. Zsoldos, Study of the magnetic phase transformation in the Mn3Sn phase, Physica B+C 80 (1975) 226–230. https://doi.org/10.1016/0378-4363(75)90066-2.

[53] Y. Liu, B. Zhou, C. Wu, H. Peng, J. Wang, X. Su, Experimental Investigation of the Isothermal Section of the Fe-Mn-Sn System at 723 K, J. Phase Equilib. Diffus. 39 (2018) 280–289. https://doi.org/10.1007/s11669-018-0630-7.

[54] B. Fayyazi, K.P. Skokov, T. Faske, I. Opahle, M. Duerrschnabel, T. Helbig, I. Soldatov, U. Rohrmann, L. Molina-Luna, K. Güth, H. Zhang, W. Donner, R. Schäfer, O. Gutfleisch, Experimental and computational analysis of binary Fe-Sn ferromagnetic compounds, Acta Materialia 180 (2019) 126–140. https://doi.org/10.1016/j.actamat.2019.08.054.

[55] B. Fayyazi, K.P. Skokov, T. Faske, D.Y. Karpenkov, W. Donner, O. Gutfleisch, Bulk combinatorial analysis for searching new rare-earth free permanent magnets: Reactive crucible melting applied to the Fe-Sn binary system, Acta Materialia 141 (2017) 434–443. https://doi.org/10.1016/j.actamat.2017.09.036.

[56] M.F.J. Boeije, L. Van Eijck, N.H. Van Dijk, E. Brück, Structural and magnetic properties of hexagonal $(Mn,Fe)_{3-\delta}Ga$, Journal of Magnetism and Magnetic Materials 433 (2017) 297–302. https://doi.org/10.1016/j.jmmm.2017.02.058.

[57] N.H. Sung, F. Ronning, J.D. Thompson, E.D. Bauer, Magnetic phase dependence of the anomalous Hall effect in Mn3Sn single crystals, Applied Physics Letters 112 (2018) 132406. https://doi.org/10.1063/1.5021133.

Chapter 2

Theoretical Aspects

This chapter provides relevant background information regarding the topics covered in this Dissertation. The background information is divided into three Sections. Section 2.1 presents the fundamental thermodynamics involved in the magnetocaloric effect. Section 2.2 presents the heat capacity contributions. Section 2.3 presents the classification of the magnetic phase transitions and their behaviour in terms of the Landau model.

2.1 Thermodynamics of the Magnetocaloric Effect

2.1.1 Gibbs free energy and Maxwell relations for magnetic system

The reversible magnetocaloric effect originates from fundamental thermodynamic principles. The Gibbs free energy is the central thermodynamic potentials that describes the state of a system. In a magnetic system, it can be expressed in terms of the magnetization M and the external magnetic field $\mu_0 H$ as:

$$G = U - TS + pV - \mu_0 HM \tag{2.1}$$

Where U represents the internal energy, T the absolute temperature, S the entropy, p the pressure and V the volume. The differential of the Gibbs free energy can then be expressed as:

$$dG = -SdT + Vdp - Md\mu_0 H \tag{2.2}$$

Conversely, at constant pressure, the differential of the Gibbs free energy can be expressed as:

$$dG(T,H) = \left(\frac{\partial G}{\partial T}\right)_H dT + \left(\frac{\partial G}{\partial \mu_0 H}\right)_T d\mu_0 H \tag{2.3}$$

From equation 2.3, the second derivatives of G can be expressed as:

$$\left[\frac{\partial}{\partial \mu_0 H}\left(\frac{\partial G}{\partial T}\right)_H\right]_T = \left[\frac{\partial}{\partial T}\left(\frac{\partial G}{\partial \mu_0 H}\right)_T\right]_H \tag{2.4}$$

If these partial derivatives exist and are continuous, then according to equation 2.3, internal parameters such as the system's magnetization (M), volume (V), and entropy (S) can be derived in terms of the partial derivatives of G [1–3], leading to:

$$S(T,p,H) = -\left(\frac{\partial G}{\partial T}\right)_{p,H} \tag{2.5}$$

$$V(T,p,H) = \left(\frac{\partial G}{\partial p}\right)_{T,H} \tag{2.6}$$

$$M(T,p,H) = -\left(\frac{\partial G}{\partial \mu_0 H}\right)_{T,p} = -\frac{1}{\mu_0}\left(\frac{\partial G}{\partial H}\right)_{T,p} \tag{2.7}$$

Thus, the Maxwell relations can be derived by combining Equations 2.4, 2.5, 2.6, and 2.7, expressed as:

$$\frac{1}{\mu_0}\left(\frac{\partial S}{\partial H}\right)_{T,p} = \left(\frac{\partial M}{\partial T}\right)_{H,p} \tag{2.8}$$

In magnetic systems, the Maxwell relation of Equation (2.8) is often used to derive the isothermal entropy change based on magnetization data.

2.1.2 Isothermal entropy change derived from magnetization data

At constant pressure, the total entropy change of a magnetic solid material resulting from a change in external field can be expressed as the sum of three entropy components: magnetic (S_m), lattice (S_l) and electronic (S_e) entropy terms:

$$S(T, \Delta\mu_0 H) = S_m(T, \Delta\mu_0 H) + S_l(T, \Delta\mu_0 H) + S_e(T, \Delta\mu_0 H) \qquad (2.9)$$

In systems with localized magnetic moments, such as pure Gd, the entropy change ΔS can be predominantly determined by the isothermal entropy change ΔS. However, for magnetic materials where the magnetic moments are carried by itinerant electrons, it may not be legitimate to separate each entropy term from equation (2.10) for individual estimation, as all three terms contribute and are coupled during the phase transition. In practice, the Maxwell relation remains the most commonly used method to represent the total isothermal entropy change in MCE materials.

Therefore, the integration of equation (2.9) yields the isothermal entropy change induced by varying the applied magnetic field from $\mu_0 H_i$ to $\mu_0 H_f$, expressed as:

$$\Delta S(T, \Delta\mu_0 H) = \int_{\mu_0 H_i}^{\mu_0 H_f} \left(\frac{\partial M(T, \Delta\mu_0 H)}{\partial T} \right)_H \mu_0 dH \qquad (2.10)$$

2.1.3 Magnetocaloric effect derived from calorimetry

The magnetocaloric effect (MCE) can also be determined through calorimetric measurements. The indirect calorimetric method involves constructing the $S(T, \mu_0 H)$ diagram. Based on the first law of thermodynamics, the total differential of the system's internal energy can be expressed as:

$$dU = dQ - dW \qquad (2.11)$$

Where Q represents the thermal energy and W denotes the work input by an external force. According to the second law of thermodynamics, at constant pressure and magnetic field:

$$dS = \frac{dQ}{T} \qquad (2.12)$$

Where dQ represents the heat flow into the sample. On the other hand , the specific heat at constant pressure and magnetic field is defined as:

$$C_{H,p} = \left(\frac{dQ}{T} \right)_{H,p} \qquad (2.13)$$

Thus, based on equations (2.12) and (2.13) and the integral of these terms, the entropy at constant temperature and magnetic field can be obtain :

$$S(T,H) = \int_0^T \frac{C(T,H)}{T} dT \qquad (2.14)$$

Once the $S(T)$ diagram is established by integrating the $C(T, \mu_0 H)$ data, the calculation of the isothermal entropy change (ΔS) and adiabatic temperature change (ΔT_{ad}) corresponds to the vertical and horizontal shifts differences at constant temperature or constant entropy, respectively.

$$\Delta S(T, \Delta \mu_0 H) = S(T, \mu_0 H_f) - S(T, \mu_0 H_i) \qquad (2.15)$$

$$\Delta T_{ad}(\Delta \mu_0 H) = T(S, \mu_0 H_f) - T(S, \mu_0 H_i) \qquad (2.16)$$

2.2 Heat Capacity

The heat capacity is a basic physical quantity. Since in this thesis both the heat capacity and the latent heat are studied, here these entropy contributions are presented in terms of the heat capacity. According to the second law of thermodynamics, the specific heat is defined as:

$$C_{H,p} = T \left(\frac{\partial S}{\partial T} \right)_{H,p} \qquad (2.17)$$

Where T represents the temperature, S is the entropy under a constant field $\mu_0 H$ and pressure p. The thermodynamic relations between the entropy S to the Gibbs free energy G of equation (2.5) leads to:

$$\left(\frac{\partial S}{\partial T} \right)_{H,p} = - \left(\frac{\partial^2 G}{\partial T^2} \right)_{H,p} \qquad (2.18)$$

Inserting equation 2.18 into equation 2.17 results in:

$$C_{H,p} = -T \left(\frac{\partial^2 G}{\partial T^2} \right)_{H,p} \qquad (2.19)$$

In a magnetic material the heat capacity can be defined by different contributions, including magnetic, structural and electronic degrees of freedom. When a material undergoes a first-order magnetic transition (FOMT), latent heat also needs to be considered:

$$C_p^{tot} = C_p^{el} + C_p^{ph} + C_p^{m} + C_p^{m,L} \qquad (2.20)$$

The free-electron model, primarily developed by Arnold Sommerfeld and often referred to as the Sommerfeld model, is used to describe the behaviour of conductive electrons in a material. Within this framework, the electronic contribution to the heat capacity can be calculated as:

16

$$C_p^{el}(T) \cong \gamma\, T \tag{2.21}$$

$$\gamma = \frac{\pi^2 (3\pi^2)^{-2/3} m_e k_B^2}{\hbar^2} \left(\frac{N_{c.e.}}{V}\right)^{1/3} \tag{2.22}$$

where γ is the Sommerfeld constant, m_e is the electron mass and $N_{c.e.}$ is the number of conduction electrons in a volume V.

The Debye model (Debye, 1912 [4]) estimates the contribution of phonons to the heat capacity of a material. This model is based on the concept that lattice vibrations are quantized in quasi-particles known as acoustic phonons with a linear dispersion. The phonon contribution, as calculated using this model, is given by:

$$C_p^{ph}(T) = 9\frac{N_{atoms}}{V} k_B \left(\frac{T}{\Theta_D}\right)^3 \int_0^{\Theta_D/T} \frac{y^4 e^y}{(e^y - 1)^2} dy \tag{2.23}$$

where N_{atoms} is the number of atoms in the volume V and Θ_D is the Debye temperature. While this model effectively describes the heat capacity at low temperatures, discrepancies become more pronounced at higher temperatures, where often optical phonons, described by the Einstein model for dispersion-less phonons, also start to contribute.

When the material exhibits a second-order magnetic transition (SOMT) from the ordered to the disordered state, the magnetic contribution to the heat capacity can be expressed as:

$$C_p^m(T, H) \cong CT^{3/2} \qquad \text{for} \qquad T < T_C \tag{2.24}$$

$$C_p^m(T, H) \cong 0 \qquad \text{for} \qquad T > T_C \tag{2.25}$$

Additionally, when the material undergoes a FOMT, there is a contribution originating from the latent heat L involved in the transformation. This latent heat results in a peak-shaped contribution described by:

$$C_p^{m,L}(T, H) \cong LG(T) \tag{2.26}$$

where $G(T)$ can be described by a normalised Gaussian distribution centred at T_C.

2.3 Magnetic Phase Transitions

2.3.1 Landau model

The type of phase transition can be distinguished using Landau theory, which identifies discontinuities in the derivatives of the Gibbs free energy (G) with respect to thermodynamic variables such as magnetization (M), volume (V) and entropy (S). If the first derivatives of G with respect to the control variables H, p and T (corresponding to M, V and S) exhibit a discontinuous change during the magnetic phase transition, the material is classified as undergoing a first-order magnetic transition (FOMT). In contrast, if the second derivative of G displays a discontinuity in C_p, the material corresponds to a second-order magnetic transition (SOMT), as shown in Fig. 2.1.
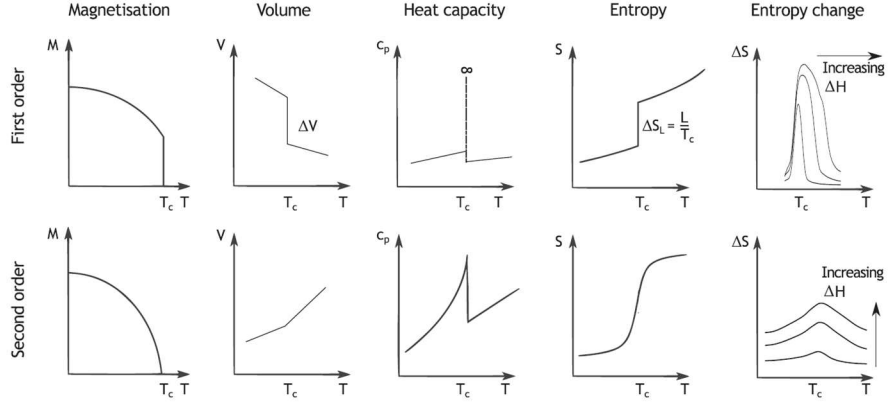
Fig. 2.1. magnetization M, volume V, heat capacity C_p, entropy S and entropy change ΔS for first-order and second-order phase transition [5].

To investigate the thermodynamic properties near a magnetic phase transition, a free-energy functional can be introduced to describe the energy difference between an ordered phase and a disordered phase. In a disordered system, a phase transition to an ordered phase may occur when the temperature decreases. The degree of order in the ordered state is characterized by an order parameter M, which progressively increases as the temperature decreases. This parameter represents the ordered moment in a magnetic phase.

Close to the phase transition temperature the Gibbs free energy can be represented by a Taylor expansion of order parameter M [6]:

$$\Delta G = \frac{\alpha}{2}M^2 + \frac{\beta}{4}M^4 + \frac{\gamma}{6}M^6 - \mu_0 HM \tag{2.27}$$

Where M is the magnetization, $\mu_0 H$ is the applied magnetic field, and $\alpha_0 > 0$, β and $\gamma \geqslant 0$ are constants. At the phase transition, the Gibbs free energy can be evaluated by $\partial \Delta G / \partial M = 0$ resulting in:

$$\alpha M + \beta M^3 + \gamma M^5 = \mu_0 H \qquad (2.28)$$

The nature of the ferromagnetic-to-paramagnetic (FM-PM) phase transition is determined by the value of β:

- When $\beta < 0$: first-order phase transition (FOMT), with a discontinuous change in S, M and V.
- When $\beta > 0$: second-order phase transition (SOMT) with a continuous change in Cp.
- When $\beta = 0$: critical point (CP) at the boundary between the FOMT and SOMT.

2.3.2 Evolution of the field exponent n for the isothermal entropy change

The field exponent (n) for the isothermal entropy change (ΔS) in a magnetic field was determined using the Bean-Rodbell model [7,8] and the Landau model [9], which aids in the classification of the nature of ferromagnetic-to-paramagnetic transitions at the Curie temperature (T_C) in magnetocaloric materials. The isothermal entropy change (ΔS) of the magnetic system at the phase transition can be calculated using Equation (2.10). The field-dependence of the isothermal isothermal entropy change follows a power law of the type:

$$|\Delta S| \propto H^n \qquad (2.29)$$

where the field exponent n is a temperature- and magnetic field-dependent function that can be expressed as [7]:

$$n(T,H) = \frac{d \ln(|\Delta S|)}{d \ln(H)} \qquad (2.30)$$

Van Dijk [9] derived the field exponent for ΔS_m using the Landau model, characterizing its dependence on temperature and magnetic field for the SOMT, CP and FOMT. In the low temperatures limit, $n \approx 1$ and in the high temperature limit n tends toward 2. Below the phase transition, the minimum values of n were determined to be 2/3, 2/5 and 0 for SOMT, CP and FOMT, respectively, as shown in Fig. 2.2. Across the phase transition, the maximum value of n tends toward 2 for the SOMT and CP, whereas theory predicts that maximum of $n \to \infty$ for the FOMT. However, experimental observations define $n > 2$ as indicative of the FOMT.
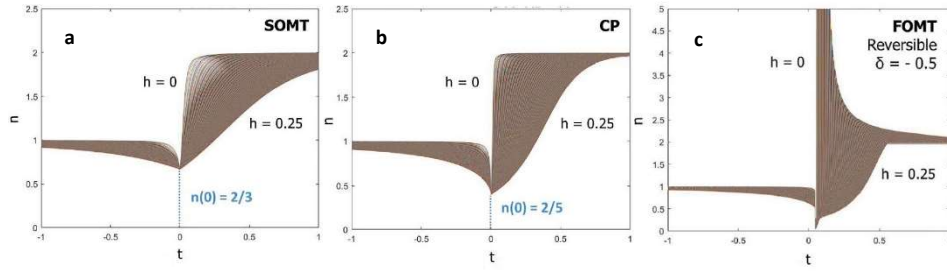
Fig. 2.2. Field exponent of the entropy change $n = \mathrm{d} \ln (|\Delta S_\mathrm{m}|)/\mathrm{d} \ln (h)$, is analysed as a function of the reduced temperature t for SOPT, CP and reversible FOPT. This analysis is conducted for various reduced magnetic fields h ranging from 0 to 0.25, where $t = (T - T_0)/T_0$ and $h = \mu_0 H/\mu_0 H_0$ [9].

References

[1]   A.M. Tishin and Y. I. Spichkin, *The magnetoclaoric effect and its Applications* (Bristol:Institute of Physics Publishing, 2003).

[2]   R. A. Swalin, *Thermodynamics of Solids* (New York: Wiley, 1962).

[3]   M.D. Kuz'min, A.M. Tishin, Magnetocaloric effect. Part 1: An introduction to various aspects of theory and practice, Cryogenics 32 (1992) 545–558. https://doi.org/10.1016/0011-2275(92)90041-8.

[4]   P. Debye, Zur Theorie der spezifischen Wärmen, Annalen der Physik 344 (1912) 789–839. https://doi.org/10.1002/andp.19123441404.

[5]   J. Lyubina, Magnetocaloric materials for energy efficient cooling, J. Phys. D: Appl. Phys. 50 (2017) 053002. https://doi.org/10.1088/1361-6463/50/5/053002.

[6]   J. M. D. Coey, Magnetism and Magnetic Materials, Cambridge University Press, New York, (2009).

[7]   J.Y. Law, V. Franco, L.M. Moreno-Ramírez, A. Conde, D.Y. Karpenkov, I. Radulov, K.P. Skokov, O. Gutfleisch, A quantitative criterion for determining the order of magnetic phase transitions using the magnetocaloric effect, Nat Commun 9 (2018) 2680. https://doi.org/10.1038/s41467-018-05111-w.

[8]   V. Franco, J.S. Blázquez, A. Conde, Field dependence of the magnetocaloric effect in materials with a second order phase transition: A master curve for the magnetic entropy change, Applied Physics Letters 89 (2006) 222512. https://doi.org/10.1063/1.2399361.

[9]   N.H. van Dijk, Landau model evaluation of the magnetic entropy change in magnetocaloric materials, J. Magn. Magn. Mater. 529, (2021) 167871.

Chapter 3

Experimental Methods

This chapter provides a brief overview of the sample preparation methods and characterization techniques employed in this thesis. Several different material systems have been investigated using different preparation techniques, including high-energy ball milling, melt spinning and arc melting in the fundamental aspects of materials and energy (FAME) group at the faculty of applied sciences, delft university of technology (TU-Delft).

Magnetic measurements, including SQUID and VSM magnetometry, heat capacity, Mössbauer spectroscopy and X-ray diffraction measurements were performed in the department of Radiation, Science and Technology (RST). The neutron powder diffraction measurements were performed at the Reactor Institute Delft (RID). The scanning electron microscopy (SEM) coupled with energy-disperse X-ray spectroscopy (EDS) and electron backscatter diffraction (EBSD) were performed in the department of materials science at TU Delft. X-ray absorption spectroscopy measurements were performed at the ID12 beamline of the European Synchrotron Radiation Facility (ESRF) in France.

3.1 Sample Preparation Methods

3.1.1 High energy ball milling

Ball milling is a commonly employed technique for grinding and synthesizing alloys from powders. In **Chapters 4** and **5**, (Mn, Fe)$_2$(P, Si) compounds were initially homogenized using a planetary ball mill (PM100, Retsch). The starting materials (powders) were placed into grinding pots along with seven iron balls, maintaining a ball-to-sample mass ratio of 5:1. The milling process was conducted for 10 hours at a rotational speed of 380 rpm. To prevent oxidation during the milling process, the jars were sealed under an argon (Ar) atmosphere, ensuring an inert environment. The grinding jars were mounted on a counter-rotating disc, trapping powders between the jar walls and iron balls. This induced mechanical deformation, altering atomic coordination shells, triggering structural excitations, and enhancing chemical reactivity by disrupting thermodynamic equilibrium [1]. Fig. 3.1 provides a schematic representation of the planetary ball-milling process.
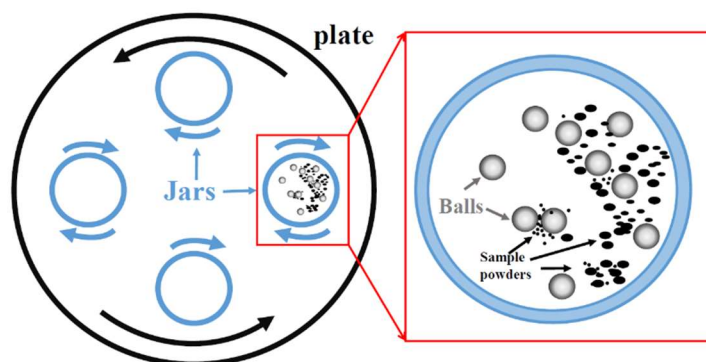
Fig. 3.1. schematic drawing of the planetary ball-milling process [2].

3.1.2 Arc-melting

Arc melting is a widely utilized technique for synthesizing alloys and intermetallic compounds by melting metallic components under a controlled environment. A schematic drawing of the arc-melting setup is shown in Fig 3.2. This process involves the generation of an electric arc between a tungsten electrode and a conductive base to achieve the high temperatures required for melting. The arc is generated in an inert atmosphere, typically argon, or under a vacuum to minimize contamination from oxidation or other chemical reactions with the surrounding environment. In **Chapters 6** and **7**, YNi$_{4-x}$Co$_x$Si and (Mn,Fe)$_3$Sn compounds were initially homogenized using arc melting. The total mass of 5 g starting materials, in the form of elemental powders, chips, or small

pieces, are weighed according to the desired composition and placed on the copper crucible. The chamber is sealed, evacuated down to 1×10^{-7} mbar and then the chamber is filled with 500 mbar high purity argon gas. An electric current is passed through a water-cooled tungsten electrode, creating a high-energy arc. The intense heat melts the sample on the copper crucible. To ensure the homogeneity of the molten sample, it is flipped and remelted five times to minimize inhomogeneities arising from variations in cooling rates within the copper crucible. The melted material rapidly solidifies upon cooling, often forming a homogeneous alloy.
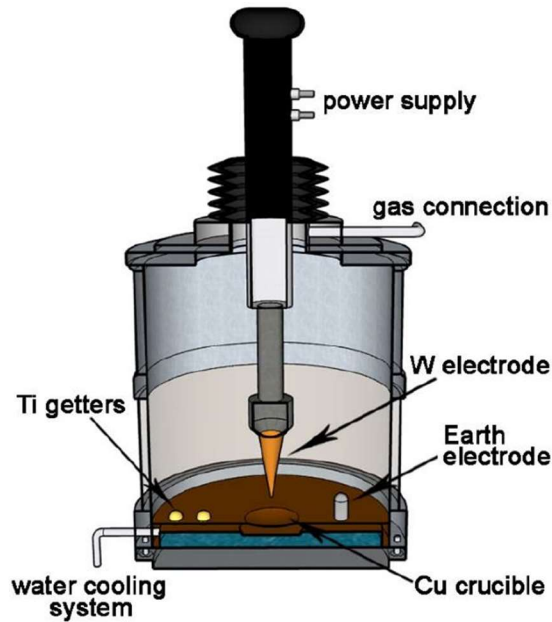
Fig. 3.2. schematic drawing of the arc melting process [3].

3.1.3 Melt spinning

Melt spinning is a rapid solidification technique commonly employed to produce metallic materials with refined microstructures, often used to enhance the properties of metals and alloys. In this process, a molten metal is extruded through a small nozzle and subjected to rapid cooling of 10^6 K/s, typically using a rotating cooled copper-wheel. This high cooling rate induces the formation of fine microstructures, which can include amorphous or nanocrystalline phases, depending on the material and cooling conditions. Melt spinning allows for the production of thin ribbons or fibres with improved mechanical properties, such as higher strength, hardness, and wear resistance, compared to conventionally

cast materials. All the materials studied in this thesis were initially prepared using ball milling and arc melting, followed by melt spinning. The melt spinning device used in this work was produced by Edmund Bühler GmbH [4]. The samples were melted in an Ar atmosphere (750 mbar) by applying radio frequency (RF) current through a water-cooled induction coil, which induced a temperature rise and melted the materials placed in a quartz tube. Upon completion of the melting process, the liquid phase was ejected through a nozzle by Ar overpressure onto a rapidly rotating copper wheel at a speed of approximately 30 m/s. The resulting ribbons were then sealed in a quartz tube under an Ar atmosphere of 200 mbar and annealed at 1373, 873, and 773 K for $(Mn,Fe)_2(P,Si)$, $YNi_{4-x}Co_xSi$ and $(Mn,Fe)_3Sn$ before being quenched to room temperature. The primary advantage of samples prepared using this technique is the improved purity of the main phase. In particularly, oxide impurities are rejected during the melt spinning process, leading to enhanced magnetic properties in the final product [5]. A schematic drawing of the melt-spinning process is shown in Fig 3.2.
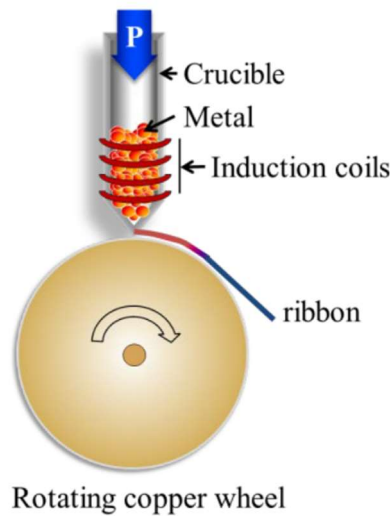
Fig. 3.3. schematic drawing of the melt spinning process [6].

3.2 Sample Characterization

3.2.1 Superconducting quantum interference device

A Superconducting Quantum Interference Device (SQUID) is an ultra-sensitive magnetometer used to measure extremely weak magnetic fields down to 10^{-14} T. SQUIDs exploit the quantum mechanical properties of superconducting materials, particularly Josephson junctions, to achieve a remarkable sensitivity. These devices are widely used in various fields, including physics and material science. At its core, a SQUID consists of a closed loop made of a superconducting material, which exhibits zero electrical resistance below a critical temperature. A SQUID includes one or more Josephson junctions—narrow insulating barriers separating two superconductors. These junctions allow the quantum tunnelling of Cooper pairs (pairs of electrons in a superconducting state) and give the device its unique properties. Changes in the external magnetic field modify the phase of the superconducting wavefunction, generating a measurable voltage across the SQUID. A SQUID magnetometer is employed to measure the magnetization of a specimen as a function of both temperature and applied magnetic field [7,8]. Transition temperatures (T_C) and thermal hysteresis (ΔT_{hys}) were determined from measurements at 0.01 T. Isothermal entropy change (ΔS) was calculated using Maxwell relations from magnetization-temperature (M-T) measurements at different magnetic fields. Magnetic measurements were performed with MPMS-XL magnetometers (Quantum Design) in fields up to 7 T and temperatures ranging from 5 to 370 K at a 2 K/min sweep rate, using the reciprocating sample option (RSO) mode. Samples weighing 1–3 mg were placed in a gelatine capsule and secured in a polypropylene (PP) straw.

3.2.2 Vibrating sample magnetometer

A Vibrating Sample Magnetometer (VSM) is an advanced laboratory instrument used to measure the magnetic properties of materials. It is especially useful for determining the magnetization of a sample as a function of an applied magnetic field. The VSM operates on the principle of detecting the change in magnetic flux generated by a vibrating magnetic sample in the presence of an external magnetic field. In our experimental measurements, a vibrating sample magnetometer (VSM) integrated into the Quantum Design VersaLab for the Physical Property Measurement System (PPMS) was employed to investigate the magnetic properties of compounds with T_C above the calibration range of the SQUID magnetometer [9]. The VSM enables the measurement of magnetic properties over a temperature range of 50-650 K and magnetic fields of 0-3 T. During VSM operation, the specimen (5-10 mg) oscillates at a frequency of 40 Hz near a detection coil, inducing a voltage due to changes in the magnetic flux.

3.2.3 Semi adiabatic heat capacity measurements

Heat capacity measurements were performed using a semi adiabatic heat capacity measurements [10], based on the standard "2τ" relaxation method of a physical properties measurement system (PPMS VersaLab, Quantum Design), supplemented by a scanning single pulse method (SPM) with $\Delta T = \pm 7$ K at the transition. This approach ensures covering the full transition to avoid overestimation or underestimation of the latent heat (L) [11]. The thermal analysis models for heat capacity measurements are central to converting raw data into heat capacity. These models rely on a mathematical framework that describes the temperature response of the platform as a function of time.

Two distinct models, so-called the 1τ and 2τ models, are available for analysis. The 1τ model, being the simpler of the two, represents the most basic approach to analysing raw measurement data. It assumes that the sample and the sample platform are in excellent thermal contact and maintain the same temperature throughout the measurement process. In this model, the platform's temperature T as a function of time t is governed by the following equation:

$$C_{total} \frac{dT}{dt} = -K_w(T - T_b) + P(t) \tag{3.1}$$

where C_{total} represents the total heat capacity of the sample and the sample platform, K_w denotes the thermal conductance of the supporting wires, T_b is the temperature of the thermal bath (puck frame) and $P(t)$ is the power applied by the heater. During the heating portion of the measurement, the heater power $P(t)$ is equal to P_0, while it becomes zero during the cooling portion. The solution to this equation involves exponential functions characterized by a time constant τ, which is defined as $\tau = C_{total}/K$.

The heat capacity option employs the 2τ model to measure the heat capacity of a sample when poor thermal contact between the sample and the platform results in a temperature gradient between them. The 2τ model accounts for the heat transfer dynamics both between the sample and the sample platform, and between the sample platform and the puck. The model is mathematically represented by the following equations:

$$C_{platform} \frac{dT_p}{dt} = P(t) - K_w[T_p(t) - T_b] + K_g[T_s(t) - T_p(t)] \tag{3.2}$$

$$C_{sample} \frac{dT_s}{dt} = -K_g[T_s(t) - T_p(t)] \tag{3.3}$$

Here, $C_{platform}$ represents the heat capacity of the sample platform, C_{sample} denotes the heat capacity of the sample and K_g is the thermal conductance between them, attributed to the grease. The temperatures of the platform and the sample are

expressed as $T_p(t)$ and $T_s(t)$, respectively. In this thesis, heat capacity measurements were performed using a vertical sample puck. The compacted thin ribbon samples were sintered at 1373 K for 24 hours, then weighed (5-10 mg) and mounted using Apiezon H grease. For each experiment, measurements of the addenda (i.e., the platform and grease) were preformed prior to measuring the heat capacity of the sample.

3.2.4 Mössbauer spectroscopy

Mössbauer spectroscopy is widely used to study magnetic materials, such as ferromagnets, ferrimagnets, and antiferromagnets. It can provide information about the local magnetic fields and magnetic interactions at the atomic level, allowing for detailed studies of the magnetic properties of materials. Mössbauer spectroscopy is based on the Mössbauer effect, which refers to the resonant and recoil-free absorption and emission of gamma radiation by atomic nuclei in a solid. The fundamental features of the Mössbauer effect that make it distinct from other forms of spectroscopy are the isomer shift, quadrupole splitting and magnetic hyperfine splitting. The isomer shift is sensitive to the electronic environment of the nucleus, especially the electron density around the nucleus. This sensitivity allows the technique to detect slight changes in the electron configuration, which is useful for studying chemical bonding, oxidation states, and coordination environments of specific elements, such as iron (Fe), tin (Sn), and others. Quadrupole splitting occurs when the nuclear energy levels interact with the electric field gradients generated by the surrounding atoms. The presence of these gradients causes the energy levels to split, leading to two distinct peaks in the Mössbauer spectrum. The magnitude of this splitting offers insights into the symmetry of the atomic environment surrounding the nucleus. If the nucleus has a magnetic moment and the material is placed in an external magnetic field, the interaction between the nuclear spin and the magnetic field can split the energy levels into multiple components, producing a magnetic hyperfine field. This is used to study the magnetic properties of the material, such as the magnetic moment of specific atoms and the local magnetic environment [12,13]. In the present study, Mössbauer spectroscopy was employed to investigate the complex spin structure of $(Mn,Fe)_3Sn$ compounds. Transmission [57]Fe Mössbauer spectra were recorded at temperatures from 5 K up to 350 K. A constant-acceleration spectrometer, equipped with a sinusoidal velocity drive and utilizing a [57]Co(Rh) source, was used for the measurements. The spectra were analysed and fitted using the Mosswinn 4.0 software.

28

3.2.5 X-ray diffraction

X-ray Diffraction (XRD) is the most common analytical technique employed to study the crystallographic structure, chemical composition, and physical properties of materials. It provides detailed information about the atomic arrangement and symmetry in crystalline substances by measuring the X-rays interact with the material. In the preset research, X-ray diffraction patterns were collected using an PANalytical X-pert Pro diffractometer with Cu K_α radiation ($\lambda = 1.5406$ Å) in the 2θ range from 10 to 100° at a step size of 0.02°. Temperature-dependent XRD measurements were conducted using an Anton Paar TTK450 sample chamber. The obtained diffraction patterns were refined using the Rietveld refinement implemented in the Fullprof software [14,15]. The refined XRD results allowed for the identification of the main and impurity phases, determination of phase fractions, indexing, and calculation of lattice constants and site occupancies.

3.2.6 X-ray absorption

X-ray absorption (XAS) provides detailed information about the local atomic environment, including oxidation states, coordination geometries, and the electronic structure around a specific atom in the material. When the energy of the absorption edge (a sharp rise in absorption) matches the binding energy of a core state in the absorber, electrons are excited from the core state to the lowest available unoccupied state just above the Fermi level. These absorption edges occur at different energies due to the varying nuclear charges of the absorbing element and the specific orbitals involved, which makes XAS an element-specific and orbital-specific probe. In general XAS can be divided into two regions: X-ray absorption near-edge structure (XANES) and Extended X-ray absorption fine structure (EXAFS). In this study XAS measurements were performed at the ID12 beamline of the European Synchrotron Radiation Facility (ESRF) in France [16]. The X-ray absorption spectra at the K edge of Mn and Fe were recorded using the total fluorescence yield detection mode in backscattering geometry. From the difference in absorption of right and left circularly polarized X-rays, we can obtain the X-ray magnetic circular dichroism (XMCD) signal.

3.2.7 Neutron powder diffraction

Neutrons are neutral particles, and their interaction with atomic nuclei is governed by the nuclear scattering cross-section. Unlike X-rays, which are primarily scattered by the electron cloud surrounding atoms, neutrons interact with the nucleus of atoms, making neutron diffraction sensitive to the positions

of different elements, including those with low atomic numbers like hydrogen. Neutron powder diffraction (NPD) is uniquely suited to studying the magnetic properties of materials. Since neutrons have a magnetic moment, they interact with the magnetic moments of atoms within a material. This allows NPD to investigate the magnetic structure and determine the magnitude of the magnetic moment at specific magnetic sites within the material. In this thesis, neutron diffraction was conducted using the neutron powder diffractometer PEARL at the Reactor Institute Delft (the Netherlands) with a neutron wavelength of $\lambda = 1.667$ Å. The experiments employed to study the spin structure and magnitude of the spin in the $YNi_{4-x}Co_xSi$ and $(Mn,Fe)_3Sn$ material systems. The samples, each with a mass of approximately 5 g, were placed in a vanadium sample can and measured at various temperature points. The Rietveld refinement implemented in the Fullprof software was used to refine nuclear and magnetic structures [14,15].

3.2.8 Electron microscopy

Scanning Electron Microscopy (SEM, JEOL JSM 6500 F, Japan), coupled with Energy Dispersive X-ray Spectroscopy (EDS), was employed to investigate the microstructure and chemical composition of selected compounds. Additionally, measurements performed using the Backscattered Electron (BSE) detector were used to investigate the distribution of various phases within the samples. During measurements, an accelerating voltage ranging from 10 to 15 kV was applied. Lower voltages provided greater surface sensitivity, whereas higher voltages offered detailed insights into subsurface layers, albeit with a reduction in surface morphology resolution. Electron Backscatter Diffraction (EBSD) is a powerful microstructural characterization technique widely used in materials science to determine the crystallographic properties of materials. It is an extension of SEM that provides detailed information about the orientation of the grains, phase and texture of crystalline materials at the microscale. Following synchrotron measurements, the locations of small beam spots were identified in SEM images. Consequently, EBSD measurements were preformed to analyse the grain orientation of the $Mn_{0.60}Fe_{1.30}P_{0.66}Si_{0.34}$ bulk sample.

References

[1] F. K. Ukrakaev, "Mechanism and kinetics of mechanochemical processes". High-energy ball milling – mechanochemical processing of nanopowders. Woodhead Publishing Limited, 2010.

[2] H. Mutu, Magnetocaloric effect in $M_{5-x}B_2$ family compounds, PhD Thesis, Delft University of Technology, 2024. https://doi.org/10.4233/UUID:7974F26D-00E7-4B4B-9123-21DECB4C6570.

[3] D. Barsuk, Metallurgical Design of New Nanoporous Structures, PhD Thesis, Université Grenoble Alpes, 2017.

[4] Melt spinning, 2022. Retrieved from: https://www.edmund-buehler.de/en/materials-science/melt-spinning.

[5] M.R. Pagnola, J.U. Vivero, A.G. Marrugo, Magnetic Materials by Melt Spinning Method, Structural Characterization, and Numerical Modeling, New Uses of Micro and Nanomaterials, 2018. https://doi.org/10.5772/intechopen.77368.

[6] X. You, Design of efficient magnetocaloric materials for energy conversion, PhD Thesis, Delft University of Technology, 2020. https://doi.org/10.4233/UUID:49700510-47B3-4450-85DA-C99B4D14878F.

[7] H. Lueken, Superconducting Quantum Interference Device Magnetometry, Methods in Physical Chemistry, 1 (2012) 763–795. https://doi.org/10.1002/9783527636839.ch25.

[8] M. Buchner, K. Höfler, B. Henne, V. Ney, A. Ney, Tutorial: Basic principles, limits of detection, and pitfalls of highly sensitive SQUID magnetometry for nanomagnetism and spintronics, Journal of Applied Physics 124 (2018) 161101. https://doi.org/10.1063/1.5045299.

[9] "Vibrating Sample Magnetometer (VSM) Option User's Manual", *Quantum Des. Inc.*, Part Number 1096-100, B0, 2011.

[10] J.C. Lashley, M.F. Hundley, A. Migliori, J.L. Sarrao, P.G. Pagliuso, T.W. Darling, M. Jaime, J.C. Cooley, W.L. Hults, L. Morales, D.J. Thoma, J.L. Smith, J. Boerio-Goates, B.F. Woodfield, G.R. Stewart, R.A. Fisher, N.E. Phillips, Critical examination of heat capacity measurements made on a Quantum Design physical property measurement system, Cryogenics 43 (2003) 369–378. https://doi.org/10.1016/S0011-2275(03)00092-4.

[11] V. Hardy, Y. Bréard, C. Martin, Derivation of the heat capacity anomaly at a first-order transition by using a semi-adiabatic relaxation technique, J. Phys.: Condens. Matter 21 (2009) 075403. https://doi.org/10.1088/0953-8984/21/7/075403.

[12] Y. Yoshida, G. Langouche, eds., Mössbauer Spectroscopy: Tutorial Book, Springer Berlin Heidelberg, Berlin, Heidelberg, 2013. https://doi.org/10.1007/978-3-642-32220-4.

[13] E. Kuzmann, Z. Homonnay, Z. Klencsár, R. Szalay, ^{57}Fe Mössbauer Spectroscopy as a Tool for Study of Spin States and Magnetic Interactions in Inorganic Chemistry, Molecules 26 (2021) 1062. https://doi.org/10.3390/molecules26041062.

[14] H.M. Rietveld, A profile refinement method for nuclear and magnetic structures, J Appl Crystallogr 2 (1969) 65–71. https://doi.org/10.1107/S0021889869006558.

[15] J. Rodríguez-Carvajal, Recent advances in magnetic structure determination by neutron powder diffraction, Physica B: Condensed Matter 192 (1993) 55–69. https://doi.org/10.1016/0921-4526(93)90108-I.

[16] E. Beaurepaire, H. Bulou, L. Joly, F. Scheurer, eds., Magnetism and Synchrotron Radiation: Towards the Fourth Generation Light Sources: Proceedings of the 6th International School "Synchrotron Radiation and Magnetism", Mittelwihr (France), 2012, Springer International Publishing, Cham, 2013. https://doi.org/10.1007/978-3-319-03032-6.

Chapter 4

Preparation and calorimetric measurements of the first order magnetic phase transformation in giant magnetocaloric Fe-rich (Mn,Fe)$_2$(P,Si) ribbons and bulk

Abstract

The (Mn,Fe)$_2$(P,Si) compounds are one of the rare materials systems that exhibit an isostructural first-order ferromagnetic transition (FOMT) near ambient temperature. Since its giant magnetocaloric effect (GMCE) was discovered, this system has garnered ongoing interest, both for its promising applications and for the scientific interest in uncovering the fundamental mechanisms driving the FOMT. In particular, in elastic FOMTs, magnetic interactions, lattice deformation and electronic redistribution endure cooperative changes leading to a discontinuous transition with latent heat. This study examines the evolution of microstructure and thermomagnetic properties in Mn$_{0.60+x}$Fe$_{1.3-x}$P$_{0.66-y}$Si$_{0.34+y}$ (with x=0.02, y=0.01) compounds prepared by the melt-spun technique. The simultaneous increase in Mn and Si concentrations reflects to a 40% enhancement in the isothermal entropy change ΔS (equation 2.9) compared to parent compound. Furthermore, we separate the pure latent heat (L) from the reversible specific heat. This allows us to establish a convincing correlation of intrinsic quantities between latent heat (L) and elastic strain energy (U_e). Notably, our results demonstrate that both the latent heat (L) and thermal hysteresis (ΔT_{hys}) are proportionally linked and vanish simultaneously at a supercritical end point.

4.1 Introduction

The conventional magnetocaloric effect (MCE) is an intrinsic magneto-thermodynamic phenomenon that links a change in the magnetic field with a corresponding temperature change in a material, thereby enabling magnetic refrigeration technologies [1–10]. Integrating this effect opens up novel possibilities for magnetic cooling [2,4,11,12], heat pumping [13–17], and energy conversion, such as thermomagnetic harvesting applications [18,19]. These applications are particularly useful for household and commercial cooling applications in the vicinity of room temperature. Magnetic refrigeration is beneficial for reducing greenhouse gas emissions, to mitigate global warming and to stabilize climate change. A giant magnetocaloric effect (GMCE) is typically associated with a first-order magnetic transition (FOMT). Depending on their intrinsic mechanisms, the FOMT can be classified into two types: the magneto-elastic transition that do no change the crystal symmetry, observed in materials like La(Fe,Si)$_{13}$ [20–22], FeRh [23,24], Eu$_2$In [25] and (Mn,Fe)$_2$(P,Si) [4,6], and the magneto-structural transition, where the change in magnetic state is associated with one of crystal symmetry, found in compounds such as Gd$_5$(Si,Ge)$_4$ [26], MnMX [27,28] and NiMn-based Heusler alloys [29,30], etc. Among these different material systems, Fe$_2$P-based compounds, particularly (Mn,Fe)$_2$(P,Si), stand out as one of the most promising for real application due to their low raw material costs, absence of rare earth elements, no toxic elements and a tuneable Curie temperature near room temperature. These features make this system especially suitable for eco-sustainable applications.

From a materials point of view, minimizing thermal hysteresis (ΔT_{hys}) is crucial to enhance the reversibility under cycling conditions [7,31]. Another challenge with GMCE materials is their mechanical stability. At the FOMT, not only a sharp magnetization jump is observed, but also discontinuities in other physical parameters are found [32]. For example, the for the (Mn,Fe)$_2$(P,Si) system the unit-cell contracts in the hexagonal basal plane across the FOMT, while it expands along the hexagonal axis. This overall lattice deformation results in a discontinuities of the c/a ratio of up to 10%, with a negligible unit-cell volume change of $\Delta V/V = 0.1$-0.3% at the ferromagnetic transition temperature (T_C). Previous studies indicate that, on the Fe-rich side, higher Si concentrations result in smaller discontinuities in Δa and Δc across the FOMT [6,33]. Such discontinuities can induce strong shear strains and stresses at the grain boundaries of random orientated polycrystals, particularly for larger grains.

Thermal or magnetic field cycling potentially results in the formation of fractures or even the destruction of the bulk materials. These issues can be addressed through various technical solutions, such as embedding the MCE

material in a resin or using porous shaping techniques. However, these approaches often dilute the MCE effect, which is not satisfactory as this results in an inefficient use of the magnet's capabilities and it reduces the thermal conductivity required for an effective heat transfer. Therefore, in recent years, numerous studies have explored the introduction of a fifth element to go from quaternary to quinary alloys. This includes doping with $3d$ through $5d$ transition metals [31,34–38], which can potentially fine-tune the Curie temperature (T_C) and reduce ΔT_{hys}. On the non-metallic side, elements such as As, Ge, Al and B have also been investigated as potential dopants [39–43]. In particularly, Guillou *et al*. reported that even a small amount of boron doping can significantly reduce ΔT_{hys}, and simultaneously enhance the mechanical stability [5,32]. However, from a commercialization or scaling-up perspective, this approach is not prioritized due to challenges in controlling tiny amounts of added B to tune T_C. Even slight variations in concentration can significantly impact the performance and introduce impurity phases. This is particularly critical for active magnetic regenerator (AMR) systems, which require multiple layers of material for optimal efficiency [44], as FOMT materials exhibit a GMCE over a finite temperature range. Therefore, additional research is required to manipulate the microstructure of quaternary compounds without doping by employing different synthesis methods to optimize and tailor their properties. Understanding this mechanism is crucial for the successful commercialization of the magnetic cooling technology.

FOMTs are defined by the presence of a latent heat (L) at the phase transition, connected to the transition entropy as $L = |\Delta S_{tr}|\ T_C$, stacked (superimposed) over a reversible specific heat background. As such, the latent heat is an intrinsic quantity most relevant for the development of GMCMs. Previous heat capacity measurements on the binary parent compound Fe$_2$P have shown a relatively small L at the FOMT [45–47], while (Mn,Fe)$_2$(P,Si) compounds potentially exhibit much stronger FOMTs with a larger L. Early theoretical studies suggested that L is predominantly of magnetic origin [48]. In contrast, recent inelastic scattering experiments and phonon calculations indicate that nearly all of the transition entropy (ΔS) has a structural origin [49,50]. However, the origin of L is difficult to determine because magnetic ordering, structural distortions and electron redistribution are all involved simultaneously in the FOMT of Fe$_2$P-based materials. Moreover, as these degrees of freedom can be coupled, it may be not legitimate to separate them. The relation between intrinsic quantities, such as L and U_e (magneto-elastic coupling) in these compounds, it still not fully resolved. Therefore, it is important to find an accurate method to quantify L from the thermal response of the material. Understanding the driving mechanisms controlling the strength of L in GMCMs is crucial for practical applications, as optimization largely involves maximizing the response

in L with minimal changes in the external magnetic field. The MCE is characterized by the isothermal isothermal entropy change ΔS (equation 2.9) or the adiabatic temperature change (ΔT_{ad}), depending on whether the magnetic field change is applied isothermally or adiabatically. When the MCE for different materials are compared, it is important to note that a large $|\Delta S|$ does not always correspond to a large ΔT_{ad}, so both quantities must be optimized simultaneously. These parameters directly influence the temperature span of the working device and are critical to enhance the heat transfer from the cold end to the hot end during each cycle [5,51].

In the present work, precisely this approach has been used to investigate three problems of the previous generation of $(Mn,Fe)_2(P,Si)$ materials. (*i*) The first improvement needed is manipulating the microstructure to achieve smaller grain sizes. This is directly linked to the thermal hysteresis and the mechanical stability. Hysteresis is known to be influenced by external features like microstructure. It is important to note that a large thermal hysteresis is not an intrinsic property for a FOMT, as materials with nearly negligible hysteresis, but with a sizable L can be observed in vanadium and boron doped $(Mn,Fe)_2(P,Si)$ compounds [52]. Additionally, smaller grains can help alleviate shear strains and stresses at grain boundaries, leading to improve mechanical stability, particularly considering the inherent brittleness of this type of materials. (*ii*) The second target is to separate the pure L from total specific heat observed in $(Mn,Fe)_2(P,Si)$ compounds to explore its relationship with structural deformations (elastic strain energy) across the FOMT. These two parameters serve as intrinsic quantities to distinguish strong and weak FOMTs. We propose a convenient method based on commercial calorimeter to separate L from the total thermal response of the material in $(Mn,Fe)_2(P,Si)$ bulk samples. (*iii*) The last objective is to demonstrate that materials with a FOMT show a change in the nature of the phase transition when the applied magnetic field causes T_C to reach a critical end point, leading to a gradual reduction of both ΔT_{hys} and L with applied magnetic field, vanishing at the field of the critical end point. For this purpose, we investigates the effect of simultaneously varying the Mn/Fe and P/Si ratios on the microstructure and the magnetic properties by employing the melt spinning technique.

4.2 Materials and Methods

The $Mn_{0.60+x}Fe_{1.3-x}P_{0.66-y}Si_{0.34+y}$ alloys (with $x = 2y$ ranging from $x = 0.00$ until $x = 0.08$) were synthesized by ball milling from powders of high-purity starting materials of Mn (99.7%), Fe (99.8%), Fe_2P (99.5 %), and Si (99.6%), using a ball-to-sample mass ratio of 5:1 and ball milling for 10 hours at 380 rpm. Subsequently, the resulting powders were compacted into cylinders of approximately 2.5 g each using a uniaxial press with a force of 8 tons. Then the pallets were melted and quenched by melt spinning with a copper-wheel speed of $v \approx 30$ m/s. Melt spun ribbons with widths of 2-3 mm and a thickness of the 20-40 μm were produced. Following this, the samples were sealed in quartz tubes filled with argon gas at a pressure of 200 mbar. Sintering of the samples took place in a vertical furnace, which had been preheated to 1100°C. This sintering process lasted for 2 hours before the samples were quenched in room temperature water. The choice of the sintering temperature of 1100°C was based on previous studies, which identified it as the optimal temperature for sintering [53,54].

Powder X-Ray Diffraction (XRD) was carried out on a PANalytical X-Pert PRO diffractometer, using Cu-K_α radiation with a wave length of 1.5405 Å (probing an angular range of 10°- 90°, with an angular step of 0.02°, 1s exposure per step). Temperature-dependent XRD measurements were performed with an Anton Paar TTK450 temperature chamber. The Rietveld method [55], as implemented in the FullProf software, was used for the crystal structure refinement [56].

SEM measurements were performed on the free side of the ribbon samples and on eroded surfaces of compacted pellets, using a Nital etchant. For the grain size evaluation, about 15 SEM images per samples were analysed using the MIPAR software [57] for a quantitative estimate of the average grain size.

The temperature- and field-dependent magnetization was measured with a superconducting quantum interference device (Quantum Design MPMS XL) magnetometer, using the reciprocating sample option mode (RSO) were employed to collect the magnetization data in the temperature range of 5 to 370 K with a constant sweep rate of 2 K/min and in applied magnetic fields up to 5 T. Isofield magnetization curves were recorded as a function of the temperature in sweep mode at a rate of ± 1.0 K/min. Heat capacity measurements were performed using a semi adiabatic heat capacity measurements, based on the standard "2τ" relaxation method of a physical properties measurement system (PPMS VersaLab, Quantum Design), supplemented by a scanning single pulse method (SPM) with $\Delta T = \pm 7$ K at the transition. This approach ensures covering

the full transition to avoid overestimation or underestimation of the latent heat (L) [58].

4.3 Results and Discussion

4.3.1 Crystal structural information and average crystallite size

The X-ray diffraction patterns at 400 K shown in Fig. 4.1a confirm that the synthesized $Mn_{0.60+x}Fe_{1.3-x}P_{0.66-y}Si_{0.34+y}$ ($x = 0.02$, $y = 0.01$) samples were found to be single phase with the expected hexagonal P_{-62m} symmetry. With a simultaneous increase in Mn and Si content no secondary phase is observed indicating that all samples are single phase. As shown in Fig. 4.1b and 4.1c the lattice parameter a and the unit-cell volume V present a clear increasing trend for an increase in Mn and Si contents, while the c/a ratio shows a simultaneous decrease for an increase in Mn and Si contents. In contrast, the lattice parameter c only shows a very minor change for an increase in Mn and Si contents, as shown in Fig. 4.1b. The structural refinement parameters obtained from the XRD data are summarized in Table 4.1. The temperature evolution of the (300), (211) and (002) powder XRD reflections upon heating is illustrated in Fig. 4.1d for the $Mn_{0.66}Fe_{1.24}P_{0.63}Si_{0.37}$ compound. The effect of temperature on the unit cell dimensions is directly visible in Fig. S4.1 (Supplementary Information). Across the magnetic phase transition the a and c axes undergo discontinuous changes with a phase coexistence region for the paramagnetic (PM) and ferromagnetic (FM) phases, which is a distinctive feature of the isostructural FOMT in Fe_2P-type materials [59–61]. The FM and PM phases show a phase transition centred at T_{tr} = 320 K with step-like anomalies of: $\Delta a/a$ = -0.98%, $\Delta c/c$ = 1.88%, $\Delta(c/a)/(c/a)$ = 2.81 %, $\Delta V/V = 2(\Delta a/a) + \Delta c/c \approx$ -0.1%, as shown in Fig. S1 (Supplementary Information). Theoretical calculations have noted that the c/a ratio bears a significant correlation with the magnetic exchange interactions governing the magnetoelastic coupling in Fe_2P-type materials [62,63].

When comparing the grains size of the hexagonal phase between samples with $x = 0.60$ and 0.68, no clear trend is observed for a simultaneous increase of Mn and Si contents. As shown in Fig. 4.2 both samples show low porosity and a similar log-normal distribution of grain size with an average size of about 8 μm. Numerous publications have highlighted that ball-milled bulk samples on the Mn-rich side exhibit an average grain size of about 27 μm [64], whereas for compounds with an Mn/Fe = 1 ratio, the grain size slightly diminishes, resulting in an average grain size in the range of 24-26 μm [65,66]. In contrast, the microstructure of melt-spun ribbons demonstrates significantly smaller average grain sizes and a finer overall structure compared to materials synthesized via ball milling. This is critical for the stabilization of the mechanical properties, as the

reduction in grain size reduces the maximum shear strain at grain boundaries, thereby enhancing the mechanical stability of these materials. However, grain sizes are also influenced by the sintering temperature and the annealing time. A recent study by Qianbai *et al.* [67] investigated the microstructure of materials with a Mn/Fe = 1 ratio as a function of the sintering duration and observed a significant increase in grain size with time. This increase results from grain growth during sintering, where grains merge with neighbouring grains. Using these ribbons samples, we reconstructed a bulk sample, sintered it at the 1100°C for 24 h, and re-examined the average grain size. Encouragingly, the average grain size remained constant, as shown in Fig. S4.2 (Supplementary Information), highlighting the potential of shaping bulk samples from ribbon materials.
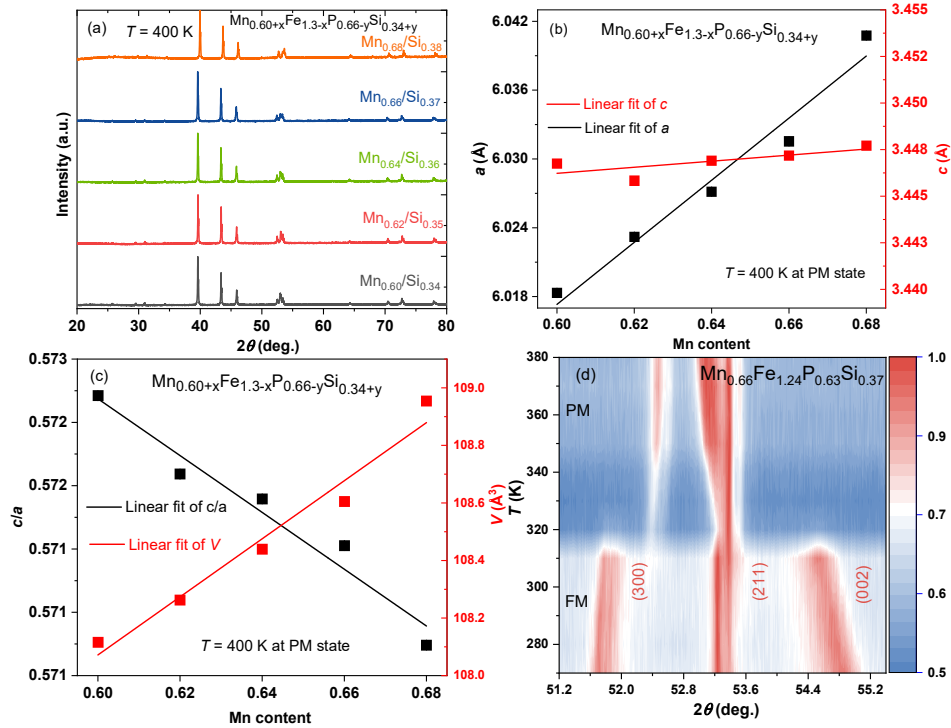
Fig. 4.1. (a) Powder XRD patterns collected at 400 K for samples of $Mn_{0.60+x}Fe_{1.3-x}P_{0.66-y}Si_{0.34+y}$ ($x = 2y$), with simultaneous changes in the Mn/Fe and P/Si ratios. (b) Lattice parameter a and c, (c) Unit-cell volume V and c/a ratio derived from XRD as a function of the Mn concentration for $Mn_{0.60+x}Fe_{1.3-x}P_{0.66-y}Si_{0.34+y}$ ($x = 2y$). (d) Intensity versus scattering angle 2Θ (°) as a function of temperature T (K) for the $Mn_{0.66}Fe_{1.24}P_{0.63}Si_{0.37}$ compound.

Table 4.1. Lattice parameters *a* and *c, c/a* ratio and unit-cell volume *V* obtained from XRD at 400 K, saturation magnetization M_s and Curie temperature T_C for the $Mn_{0.60+x}Fe_{1.3-x}P_{0.66-y}Si_{0.34+y}$ ($x = 2y$) compounds. M_s is obtained from magnetisation measurements at 5 K and the transition temperature T_C is defined as the minimum in dM/dT in an applied field of 0.01T.

x	a	c	c/a	V	$M_{s,\,5\,K@5\,T}$	$T_{tr}^{Heating}$
	(Å)	(Å)		(Å³)	(Am² kg⁻¹)	(K)
0.60	6.01832(4)	3.44676(6)	0.57271(14)	108.116(3)	162.38	295.3
0.62	6.02322(8)	3.44584(5)	0.57209(11)	108.263(2)	166.39	305.2
0.64	6.02715(9)	3.44692(5)	0.5719(11)	108.439(3)	151.93	312.3
0.66	6.03154(8)	3.44719(5)	0.57153(11)	108.605(3)	161.38	322.1
0.68	6.04076(8)	3.44771(5)	0.57074(11)	108.954(3)	153.38	331.2
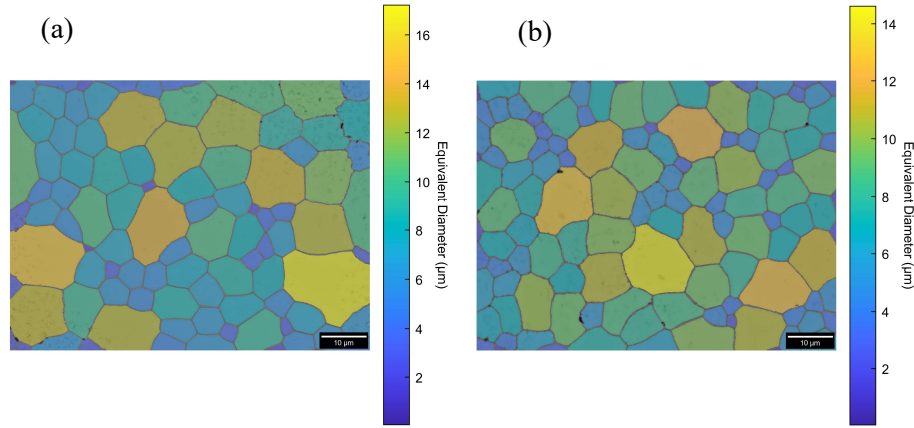
Fig. 4.2. SEM images of (a) $Mn_{0.60}Fe_{1.30}P_{0.66}Si_{0.34}$ and (b) $Mn_{0.68}Fe_{1.22}P_{0.62}Si_{0.38}$ samples sintered at 1100 °C for 2 h. The colour code highlighting the equivalent diameter of each grain is superposed on the images.

4.3.2 Magnetic and magnetocaloric properties

The temperature dependence of magnetization $M(T)$, is shown in Fig. 4.3a for zero-field-cooled (ZFC) and field-heating (FH) conditions. The overall magnetic response with a relatively sharp ferromagnetic FOMT of finite thermal hysteresis (ΔT_{hys}) is found for all samples. As shown in Fig. 4.3b the saturation magnetization does not exhibit a distinct trend with varying Mn/Si concentration, falling within the range of 140–160 Am²kg⁻¹ at 5 K in an applied field of 5 T, and saturated at an applied field of 1 T. This aligns well with literature values reported for similar Fe_2P-based compounds [37,68,69]. The transition temperature (T_C) increases linearly with the simultaneous increase in Mn and Si concentrations, leading to a slightly increase in ΔT_{hys}, as shown in Fig. 4.3c. The value of T_C is

estimated from the minimum in the temperature derivative of the magnetization (dM/dT), as shown in the inset of Fig. 4.3c. The FOMTs are always accompanied by thermal hysteresis associated with the metastability of the two phases across the transition. However, the observed ΔT_{hys} was relatively small, remaining within 5 K for all compounds. For the parent compound $Mn_{0.6}Fe_{1.3}P_{0.66}Si_{0.34}$, ΔT_{hys} was observed to be 3 K. The origin of the thermal hysteresis can be separated into intrinsic (associated with electronic properties on the atomic scale [7]) and extrinsic contributions related to microstructure; the presence of nano-precipitates [70], micro-cracks [71] or micro-pores [72], strains and stresses at interfaces [7], etc. Besides this, recent studies by Suye *et al*. [65] and Fengqi *et al*. [73] have reported that ΔT_{hys} was influenced by the particle size and found that ΔT_{hys} shows a continuous decrease for a reduction in particle size. It is found that smaller fragments require less elastic energy to complete the transformation, and consequently, a reduced ΔT_{hys} is observed [3,21].
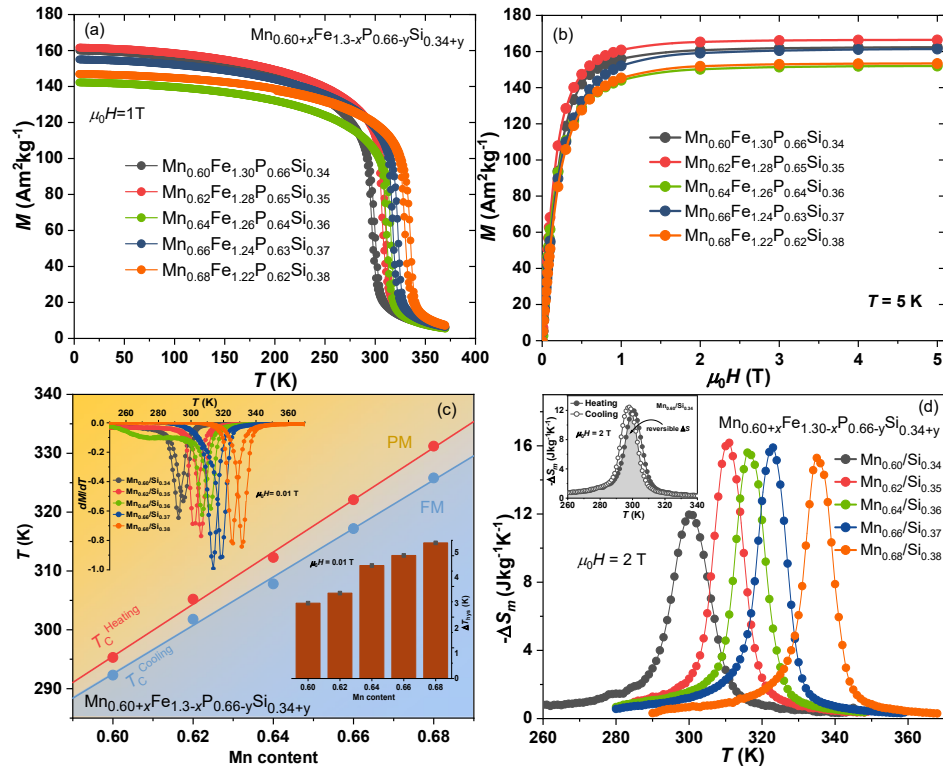

Fig. 4.3. (a) Magnetization as a function of temperature in an applied field of 1 T and (b) magnetization as a function of magnetic field at 5 K of $Mn_{0.60+x}Fe_{1.3-x}P_{0.66-y}Si_{0.34+y}$ ($x = 2y$). (c) Values of $T_{tr}^{\,Heating}$ and $T_{tr}^{\,cooling}$ as a function of the Mn content (inset shows dM/dT curves and thermal hysteresis ΔT_{hys} as a function of the Mn content at an applied field of 0.01T). (d) Isothermal entropy change $-\Delta S$ from the temperature-dependent

magnetization $M(T)$ upon heating for a magnetic field change of 2 T for $Mn_{0.60+x}Fe_{1.3-x}P_{0.66-y}Si_{0.34+y}$ ($x = 2y$).

The magnetocaloric performance expressed as the isothermal entropy change ΔS is shown in Fig. 4.3d. The isothermal entropy change is calculated by applying the Maxwell relation $\Delta S_m(T)_{\Delta H} = \int_{H_i}^{H_f} \mu_0 \left(\frac{\partial M(T,H)}{\partial T} \right)_H dH$ [26,74] to the isofield $M(T)$ data. All samples show high $|\Delta S_{max}|$ values typical of the GMCE observed at the FOMT in $Mn_{0.60+x}Fe_{1.3-x}P_{0.66-y}Si_{0.34+y}$ compounds. For the parent compound $Mn_{0.6}Fe_{1.3}P_{0.66}Si_{0.34}$ exhibiting the $|\Delta S_{max}| = 12$ J kg^{-1} K^{-1} for an applied field change of 2 T, with the simultaneous increase of Mn and Si concentrations, the $|\Delta S_{max}|$ value increased by 40% and remained constant for the subsequent compounds. Furthermore, due to the hysteresis, a reversible ΔS effect can only be obtained from the overlapping area of the heating and cooling processes, as showed in the inset of Fig. 4.3d. This indicates that a large ΔT_{hys} is a major obstacle for the application of giant MCMs. A large ΔT_{hys} significantly reduces the MCE under cycling conditions when the magnetic field is applied [75–77], and therefore significant efforts are focused on overcoming the transitional hysteresis. The present results demonstrate a well-balanced combination of a small hysteresis and a large $|\Delta S_{max}|$ in the Fe-rich Mn-Fe-P-Si quaternary system, achieved without other doping with other elements.
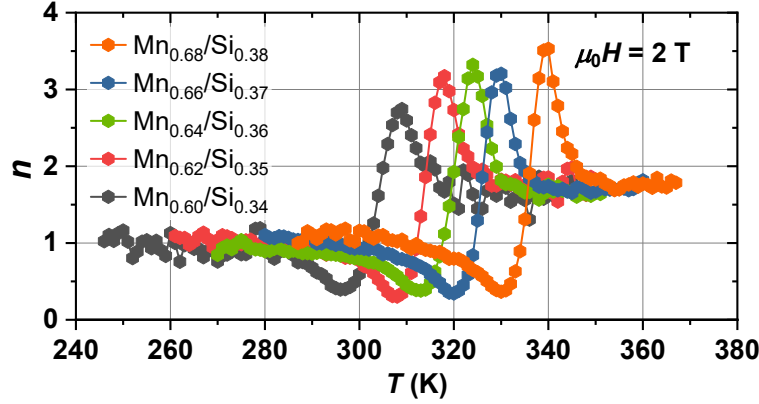
Fig. 4.4. Field exponent of the isothermal entropy change $n = \frac{d \ln(|\Delta S|)}{d \ln(H)}$ for the $Mn_{0.60+x}Fe_{1.3-x}P_{0.66-y}Si_{0.34+y}$ ($x = 2y$) compounds.

To qualitatively evaluate the order of the magnetic phase transition in $Mn_{0.60+x}Fe_{1.3-x}P_{0.66-y}Si_{0.34+y}$ compounds the field exponent of the entropy change is examined. As proposed by Franco and coworkers [78,79] and Van Dijk [80] the field-dependence of the isothermal entropy change follows a power law of the form $|\Delta S| \propto H^n$. The field exponent n can be employed to determine the FOMT or SOMT nature of the magnetic phase transition can be established. The field

exponent has a minimum value of $n = 0$ and a divergent maximum value ($n \to \infty$) near the transition [80]. This behavior is due to the step change in entropy (S) associated with the FOMT. In experimental studies, a maximum value of the field exponent n above 2 is taken as indication of a FOMT. Fig. 4.4 shows the field exponent n of the isothermal entropy change (ΔS) for the $Mn_{0.60+x}Fe_{1.3-x}P_{0.66-y}Si_{0.34+y}$ compounds. The field exponent n is consistently above 2 near T_C for all compounds and for all the applied magnetic field changes. This is line with a finite ΔT_{hys} in the $M(T)$ curves for these materials. Note that the minimum value of n remains above zero near the transition due to the persistence of short-range ferromagnetic fluctuations above T_C.

4.3.3 Indirect measurements of the giant magnetocaloric effect from specific heat

To evaluate the MCE performance, both the isothermal entropy change (ΔS) and the adiabatic temperature change (ΔT_{ad}) are considered simultaneously. The methods for measuring ΔT_{ad} are generally divided into direct and indirect approaches. In indirect measurements, ΔT_{ad} can be derived from a conventional S-T diagram based on heat capacity (C_p) measurements, which reflects the system's thermal equilibrium state [7]. So far, only few studies have been performed heat capacity measurements on $(Mn,Fe)_2(P,Si)$ compounds [66,81]. Therefore, experimental data of ΔT_{ad} on $(Mn,Fe)_2(P,Si)$ compounds are rather scarce. For this purpose, in-field heat capacity measurements were carried out to indirectly determine the ΔS and ΔT_{ad} for all five compounds over applied magnetic fields ranging from 0-3 T. The total C_p upon heating in different applied magnetic fields is illustrated in Fig. 4.5a for the $Mn_{0.66}Fe_{0.24}P_{0.63}Si_{0.37}$ compound. An intense specific heat peak with a maximum value of 3.12 $Jg^{-1}K^{-1}$ is found at 320 K. The maximum value of C_p decreases continuously with increasing applied magnetic field. At the same time the applied magnetic field stabilises the ferromagnetic order, causing a shift in T_C to higher temperatures [82]. The shift of T_{tr} with the applied magnetic field corresponds to $dT_{tr}/\mu_0 dH \approx 3.9$ K T^{-1}, as listed in Table 4.2. The S-T diagram derived from total C_p is divided by temperature T and integrated to give the total entropy $S_{total}(T) = \int_{301}^{350} \frac{C_{total}}{T} dT$, as show in Fig. 4.5b. Calorimetric measurements revealed a $|\Delta S_{max}| = 16.5$ J kg^{-1} K^{-1} at 2 T, as show in Fig. 4.5c, which aligns well with magnetization measurements showing $|\Delta S_{max}| = 16.2$ J kg^{-1} K^{-1}. This agreement confirms that the ΔS data from magnetization measurements are unaffected by spike artifacts. Furthermore, an indirectly determined ΔT_{ad} of 5.4 K was observed at 2 T, as show in Fig. 4.5d and Table 4.2, which is in good overall agreement with former studies reported by Suye *et al*. [66]. The high values of both $|\Delta S_{max}|$ and ΔT_{ad} underscore

the potential of $(Mn,Fe)_2(P,Si)$ type materials for heat pump applications, particularly given the ability to fine tune the transition temperature.
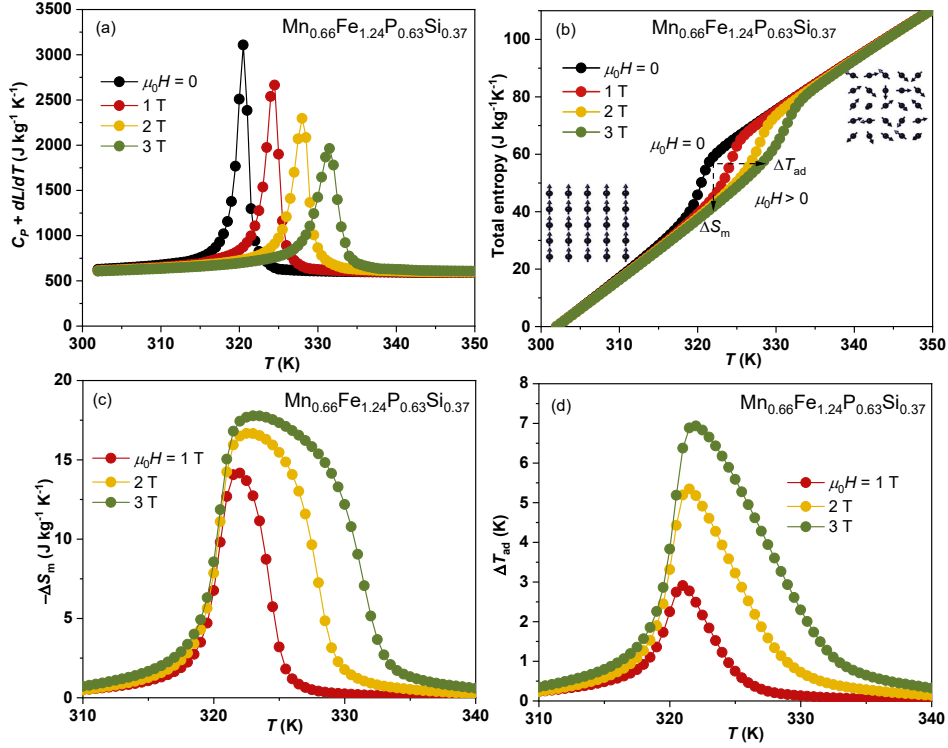
Fig. 4.5. Thermal and magnetocaloric properties of $Mn_{0.66}Fe_{1.24}P_{0.63}Si_{0.37}$. (a) In-field heat capacity measurements upon heating. (b) Total entropy change versus temperature (S-T diagram) in a magnetic field of 0, 1, 2 and 3 T. (c) Isothermal entropy change. (d) Adiabatic temperature change from calorimetry measurements.

4.3.4 Correlation of pure latent heat with strain energy

The heat capacity is a basic physical quantity reflected by magnetic, structural and electronic degrees of freedom; $C_p^{tot} = C_p^{el} + C_p^{ph} + C_p^{m}$. In metallic systems it can be decomposed into several contributions: the electronic contribution $C_p^{el} \cong \gamma T$ (where γ is a constant), the phonon contribution with a high temperature limit of $C_p^{ph} \cong 3R/M$ (where R is the gas constant and M is the molar mass), and the magnetic contribution with $C_p^{m} \cong CT^{\frac{3}{2}}$ for $T<T_C$, and $C_p^{m} \cong 0$ for $T>T_C$. Additionally, when the material undergoes a FOMT, there is a contribution of the latent heat L involved in the transformation. This latent heat results in a peak-shaped contribution of the form $C_p^{m,L} \cong LG(T)$, where $G(T)$ is a normalised Gaussian distribution centred at T_C. Recently, Guillou *et al*. [81]

investigated the influence of latent heat and magnetic contributions in Fe_2P-based compounds by theoretical calculations to separate electronic and lattice contributions from the experimental heat capacity. In order to separate the latent heat L we must also account for the magnetic specific heat. Therefore, we performed two types of specific experiments that probe: the total contribution $C_p^{total}(T) = C_p(T) + dL/dT(T)$ and the specific heat only $C_p(T)$ in zero applied magnetic field, as show in Fig. S4.3 (Supplementary Information). The difference gives the temperature derivative of the latent heat (dL/dT), which is demonstrated to show a symmetric peak, as shown in Fig. 4.6a. Integration of this term yields the latent heat L at the transition, which decreases with increasing applied field and eventually vanishes at a critical field $\mu_0 H_{cr}$. The critical field corresponds to the critical endpoint of the phase line $T_C(\mu_0 H)$. Detailed in-field calorimetry results and their data analysis are provided in Fig. S4.4 (Supplementary Information). A linear extrapolation of L indicates that the critical field is 6.4 T for the $Mn_{0.66}Fe_{1.24}P_{0.63}Si_{0.37}$ compound, as shown in the inset of Fig. 4.6a. The full width at half maximum (*FWHM*), derived from a Gaussian fit of dL/dT, increases with the applied magnetic field due to a broadening of the transition in higher fields, as shown in Fig. 4.6b. Estimating the critical end point based on only four points is challenging due to the limitations of the applied magnetic field range in the heat capacity measurements. Complementary, the temperature (T) and field ($\mu_0 H$) dependence of the magnetisation near the FOMT were used to quantitatively investigate the critical field of the present compounds. A magnetic phase diagram was constructed from temperature-dependent magnetization M for different applied fields ($\mu_0 H = 0.1$-7 T), as show in the Fig. S4.5a-b (Supplementary Information). The thermal hysteresis ΔT_{hys} decreases as the first-order nature of the transition is gradually suppressed by the applied magnetic field, with a linear extrapolation indicating that ΔT_{hys} vanishes at 6.4 T, as show in Fig. 4.6c. In contrast, the field induced transition reveals that hysteresis loop gradually closes as temperature increases, with the derivative $dM/d\mu_0 H$ clearly demonstrating that hysteresis vanishes beyond 6.6 T, as show in Fig. S4.5c-d (Supplementary Information). Both the magnetization and the calorimetric results identify the critical field value within the range of 6.4-6.6 T. Beyond this critical field L and ΔT_{hys} are no longer observed and (in analogy with supercritical liquid-vapour systems) the FM and PM states can no longer be distinguished. The overall behaviour aligns with previous findings that the FOMT vanishes above the critical endpoint [64,83]. Fig. 4.6d shows the correlation of L and ΔT_{hys} at different fields, indicating that these two parameters are proportionally linked and vanish simultaneously at the critical endpoint.

Table 4.2. FOMT parameters as a function of the Mn concentration, showing changes in the lattice parameters Δa and Δc at T_C, thermal hysteresis determined from isofield magnetic data recorded in $\mu_0 H = 0.01$ T, shift of the transition in magnetic field ($dT_{tr}/\mu_0 dH$) from isofield magnetization data. Latent heat (L) upon heating by integration of dL/dT data at $\mu_0 H = 0$; Elastic strain energy calculated from the step changes in lattice parameters observed from the XRD vs T at $\mu_0 H = 0$.

| x	$|\Delta S_{max,2T}|$	$\Delta T_{ad,2T}$	$dT_{tr}/\mu_0 dH$	L	Δa	Δc	ΔT_{hys}	Ue
Units	(Jkg^{-1}K^{-1})	(K)	(KT^{-1})	(Jg^{-1})	(Å)	(Å)	(K)	(Jg^{-1})
0.60	11.96	3.6	3.9(1)	2.02	-0.047	0.050	3.0	2.49
0.62	16.18	5.1	4.0(1)	3.29	-0.051	0.054	3.4	3.20
0.64	15.61	4.8	4.2(1)	3.83	-0.053	0.058	4.5	3.49
0.66	16.20	5.4	3.9(1)	4.35	-0.060	0.064	4.9	4.37
0.68	15.89	5.1	4.2(1)	5.79	-0.065	0.069	5.4	5.13
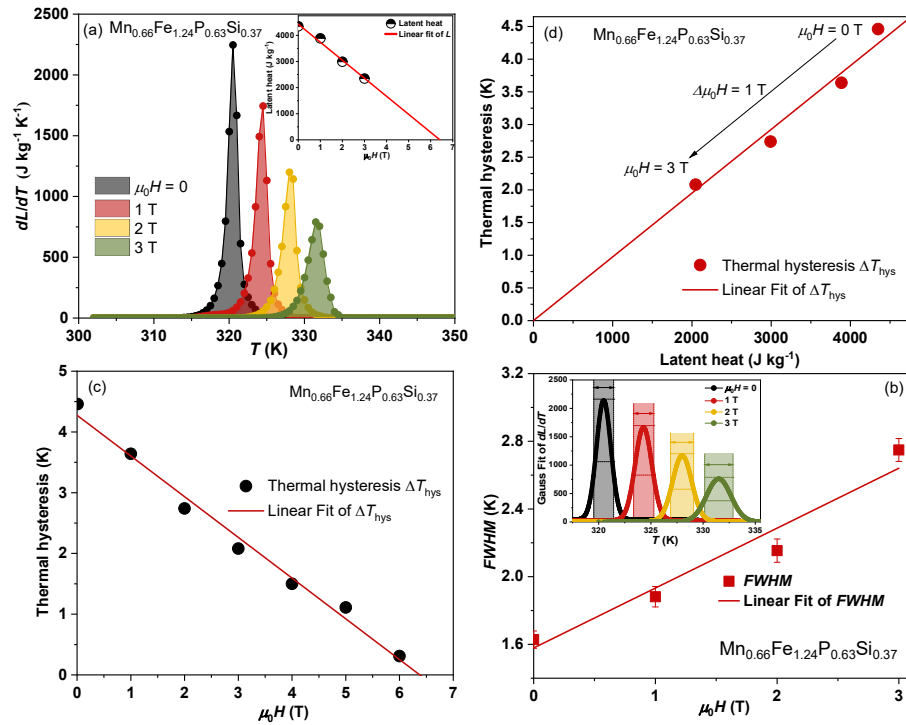
Fig. 4.6. Thermal and magnetocaloric properties of the Mn$_{0.66}$Fe$_{1.24}$P$_{0.63}$Si$_{0.37}$ compound (a) dL/dT peak from substruction of the latent heat (L) (insert shows an value of L at different magnetic field). (b) Full width at half maximum ($FWHM$) of the dL/dT peak for recorded in different applied field. (c) Thermal hysteresis (ΔT_{hys}) versus magnetic fields, derived from magnetization measurements, with ±1K/min of heating and cooling curves recorded at different applied field. (d) Proportional relation between latent heat (L) and thermal hysteresis (ΔT_{hys}) in the presence of an applied field, as derived from calorimetric and magnetization measurements.

Fig. 4.7a. demonstrates that all compounds follow the same trend, where the latent heat L decrease as the applied field increases. A simultaneous increase in Mn and Si (with $x = 2y$) results in an increase in L from 2.02 Jg^{-1} to 5.79 Jg^{-1}, serving as an intrinsic parameter to quantity the strength of the FOMT. This trend is consistent with the observed increase in ΔT_{hys} for increasing Mn and Si concentrations. In former studies [6,60,84] an attempt was made to establish a relation between various factors involved in the FOMT of Fe$_2$P-based compounds. These studies primarily focused on the relation between thermal magnetic properties and structural deformation parameters. However, it must be emphasized, that all these previous observations carry some ambiguities. A recent studies by Miao *et al.* [31] proposed the existence of a relation between ΔT_{hys} and U_e for a large panel of Fe$_2$P-based compounds. However the ΔT_{hys} is cannot be regarded as an intrinsic quantity for a FOMTs as we disused above. In contrast, a report by Guillou *et al.* [85] demonstrates a striking relation between entropy change at the transition (ΔS_{tr}) and the lattice deformation (c/a ratio). As these two are intrinsic physical quantities, they provide a more reliable basis for scaling relations. This prompted us to investigated the relationship between the latent heat and the elastic strain energy (magneto-elastic coupling). The transition-induced elastic strain energy could be expressed as: $U_e = (C_{11} + C_{12})e_1^2 + 2C_{13}e_1e_3 + C_{33}e_3^2/2$ where e_{ij} represents the tensile strains and C_{ij} corresponds to the elastic constants [31,60]. For an hexagonal lattice: $e_1 = e_2 = \Delta a/a$ within the *a-b* plane and $e_3 = \Delta c/c$ along the *c* axis. For the evaluation of the elastic strain energy we applied the elastic constants from DFT calculations reported by Roy *et al.* [86] and the experimental elastic strain values for $\Delta a/a$ and $\Delta c/c$ at T_C, as show in Fig. S4.1 (Supplementary Information).

A striking proportional relation is observed between L and U_e, with data points aligning along the diagonal, as show in Fig. 4.7b. The direct scaling of intrinsic quantities of L and U_e suggest that these quantities are equivalent. This correlation indicates that, in the FOMT of these compounds both L and U_e originate from the same sources (magnetic transition, lattice distortion and electronic distribution), which simultaneously influence both quantities during the phase transition. However, the dominant factor that controls the FOMT remains under discussion. To strengthen the statistical robustness of our analysis, we incorporated findings from previous studies on the Fe$_2$P-based system [31,32,87–89] , as shown in Fig. 4.8. As expected, the values of the latent heat from previous studies are generally higher than those for our current data. This difference is due to the method of subtraction a linear background in DSC experiments. As this also contains the contribution of the magnetic specific heat near the transition it generally overestimates the latent heat. Nevertheless, the slope remains consistent with the diagonal, supporting our proposition that an

intrinsic correlation exists between these two quantities. Further experiments are needed to refine these results. The present scaling strategy may also be extended to other magnetoelastic FOMT materials, such as La(Fe,Si)$_{13}$ [20–22], FeRh [23,24], and Eu$_2$In [25], where elastic strains energy similarly impact the first-order magnetic phase transition.
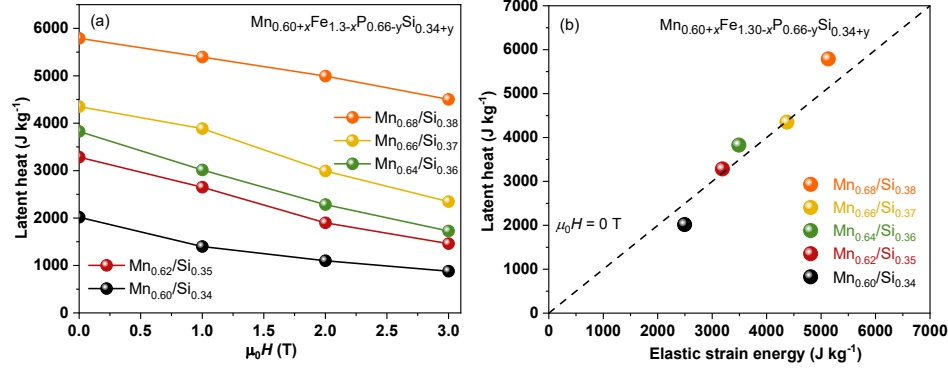
Fig. 4.7. (a) Latent heat (L) versus applied magnetic field of the Mn$_{0.60+x}$Fe$_{1.3-x}$P$_{0.66-y}$Si$_{0.34+y}$ ($x = 2y$) compounds. (b) Proportional relation between latent heat (L) and elastic strain energy (U_e) of the FOMT in the Mn$_{0.60+x}$Fe$_{1.3-x}$P$_{0.66-y}$Si$_{0.34+y}$ ($x = 2y$) compounds.
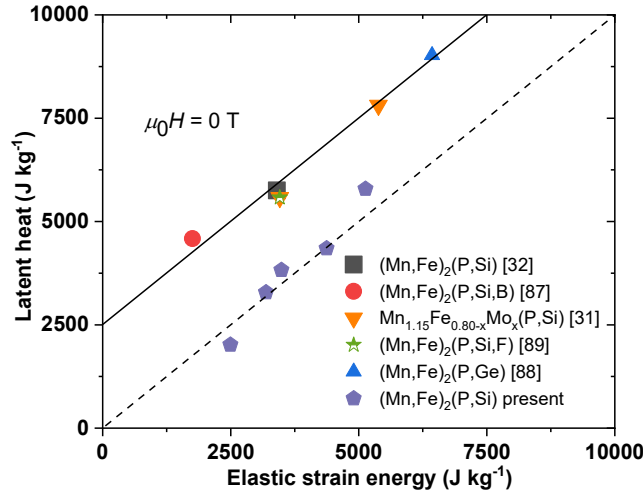
Fig. 4.8. Latent heat (L) of the FOMT as a function of elastic strain energy (U_e) for the Fe$_2$P-based system, with the current data compared to reference data from earlier generations of (Mn,Fe)$_2$(P,Si) compounds.

4.4 Conclusions

In summary, the present findings reveal that the Fe-rich $(Mn,Fe)_2(P,Si)$ quaternary system exhibits an good balance between a minimal thermal hysteresis (ΔT_{hys}) and a substantial isothermal entropy change ($|\Delta S_m|$), which can be achieved without the introduction of additional doping elements. Melt spinning can be used to tailor the microstructure of the $(Mn,Fe)_2(P,Si)$ alloys, demonstrating its viability as a method to shape high-performance bulk samples from ribbon precursors. Both the adiabatic temperature change (ΔT_{ad}) and the isothermal entropy change ($|\Delta S_{max}|$) are markedly enhanced with a simultaneous increase in Mn and Si concentrations. To uncover the underlying mechanism of the latent heat (L) and elastic strain energy (U_e) associated with the FOMT we performed two different types of calorimetry measurements to separate the latent heat and the heat capacity and quantified the elastic transformation strain energy by XRD. Consequently, a direct correlation between the latent heat L and the elastic transformation strain energy U_e was established in the $(Mn,Fe)_2(P,Si)$ family. The application of an external magnetic field was found to gradually weaken the first-order character of the transition, with both L and ΔT_{hys} decreasing proportionally and disappearing simultaneously at the critical end point. However, achieving a GMCE requires a sizable latent heat, which is inherently accompanied by significant lattice deformations that can introduce undesirable effects, such as thermal hysteresis or mechanical embrittlement. Therefore, we propose that utilizing melt spinning to tailoring the microstructure, combined with simultaneous increases in Mn and Si concentrations to fine-tune the latent heat (L), are critical strategies for the development of magnetocaloric materials compatible with practical applications.

References

[1] O. Tegus, E. Brück, K.H.J. Buschow, F.R. De Boer, Transition-metal-based magnetic refrigerants for room temperature applications, Nature 415 (2002) 150–152. https://doi.org/10.1038/415150a.

[2] E. Brück, O. Tegus, D.T.C. Thanh, K.H.J. Buschow, Magnetocaloric refrigeration near room temperature (invited), J. Magn. Magn. Mater. 310 (2007) 2793–2799. https://doi.org/10.1016/j.jmmm.2006.10.1146.

[3] J.D. Moore, K. Morrison, K.G. Sandeman, M. Katter, L.F. Cohen, Reducing extrinsic hysteresis in first-order La(Fe,Co,Si)$_{13}$ magnetocaloric systems, Appl. Phys. Lett. 95 (2009) 252504. https://doi.org/10.1063/1.3276565.

[4] N.H. Dung, Z.Q. Ou, L. Caron, L. Zhang, D.T.C. Thanh, G.A. De Wijs, R.A. De Groot, K.H.J. Buschow, E. Brück, Mixed magnetism for refrigeration and energy conversion, Adv. Energy Mater. 1 (2011) 1215–1219. https://doi.org/10.1002/aenm.201100252.

[5] F. Guillou, G. Porcari, H. Yibole, N. van Dijk, E. Brück, Taming the first-order transition in giant magnetocaloric materials, Adv. Mater. 26 (2014) 2671–2675, https://doi.org/10.1002/adma.201304788.

[6] N.H. Dung, L. Zhang, Z.Q. Ou, E. Brück, Magnetoelastic coupling and magnetocaloric effect in hexagonal Mn–Fe–P–Si compounds, Scr. Mater. 67 (2012) 975–978. https://doi.org/10.1016/j.scriptamat.2012.08.036.

[7] O. Gutfleisch, T. Gottschall, M. Fries, D. Benke, I. Radulov, K.P. Skokov, H. Wende, M. Gruner, M. Acet, P. Entel, M. Farle, Mastering hysteresis in magnetocaloric materials, Phil. Trans. R. Soc. A. 374 (2016) 20150308. https://doi.org/10.1098/rsta.2015.0308.

[8] T. Gottschall, K.P. Skokov, M. Fries, A. Taubel, I. Radulov, F. Scheibel, D. Benke, S. Riegg, O. Gutfleisch, Making a Cool Choice: The materials library of magnetic refrigeration, Adv. Energy Mater. 9 (2019) 1901322. https://doi.org/10.1002/aenm.201901322.

[9] V. Franco, J.S. Blázquez, J.J. Ipus, J.Y. Law, L.M. Moreno-Ramírez, A. Conde, Magnetocaloric effect: From materials research to refrigeration devices, Prog. Mater. Sci. 93 (2018) 112–232. https://doi.org/10.1016/j.pmatsci.2017.10.005.

[10] V. Zverev, A.M. Tishin, Magnetocaloric Effect: From Theory to Practice, in: Reference Module in Materials Science and Materials Engineering, Elsevier, 2016: p. B9780128035818028137. https://doi.org/10.1016/B978-0-12-803581-8.02813-7.

[11] M.F.J. Boeije, P. Roy, F. Guillou, H. Yibole, X.F. Miao, L. Caron, D. Banerjee, N.H. Van Dijk, R.A. De Groot, E. Brück, Efficient room-temperature cooling with magnets, Chem. Mater. 28 (2016) 4901–4905. https://doi.org/10.1021/acs.chemmater.6b00518.

[12] J. Lyubina, Magnetocaloric materials for energy efficient cooling, J. Phys. D: Appl. Phys. 50 (2017) 053002. https://doi.org/10.1088/1361-6463/50/5/053002.

[13] A. Kitanovski, Energy applications of magnetocaloric materials, Adv. Energy Mater. 10 (2020) 1903741. https://doi.org/10.1002/aenm.201903741.

[14] C. Zimm, A. Boeder, B. Mueller, K. Rule, S.L. Russek, The evolution of magnetocaloric heat-pump devices, MRS Bull. 43 (2018) 274–279. https://doi.org/10.1557/mrs.2018.71.

[15] E. Brück, H. Yibole, V.T. Nguyen, X.F. Miao, M. Boeije, N. Van Dijk, Transition metal based magneto caloric materials for energy efficient heat pumps, SSP 257 (2016) 129–134. https://doi.org/10.4028/www.scientific.net/SSP.257.129.

[16] E. Brück, H, Yibole, L. Zhang, A universal metric for ferroic energy materials, Phil.Trans.R.Soc.A374: 20150303. http://dx.doi.org/10.1098/rsta.2015.0303.

[17] D.J. Silva, J.S. Amaral, V.S. Amaral, Cooling by sweeping: A new operation method to achieve ferroic refrigeration without fluids or thermally switchable components, INT. J. REFRIG. 101 (2019) 98–105. https://doi.org/10.1016/j.ijrefrig.2019.02.029.

[18] R.A. Kishore, S. Priya, A review on design and performance of thermomagnetic devices, Renew. Sustain. Energy Rev. 81 (2018) 33–44. https://doi.org/10.1016/j.rser.2017.07.035.

[19] A. Waske, D. Dzekan, K. Sellschopp, D. Berger, A. Stork, K. Nielsch, S. Fähler, Energy harvesting near room temperature using a thermomagnetic generator with a pretzel-like magnetic flux topology, Nat Energy 4 (2018) 68–74. https://doi.org/10.1038/s41560-018-0306-x.

[20] F. Hu, B. Shen, J. Sun, Z. Cheng, G. Rao, X. Zhang, Influence of negative lattice expansion and metamagnetic transition on magnetic entropy change in the compound $LaFe_{11.4}Si_{1.6}$, Appl. Phys. Lett. 78 (2001) 3675–3677. https://doi.org/10.1063/1.1375836.

[21] F.X. Hu, L. Chen, J. Wang, L.F. Bao, J.R. Sun, B.G. Shen, Particle size dependent hysteresis loss in $La_{0.7}Ce_{0.3}Fe_{11.6}Si_{1.4}C_{0.2}$ first-order systems, Appl. Phys. Lett. 100 (2012) 072403. https://doi.org/10.1063/1.3684244.

[22] E. Lovell, A.M. Pereira, A.D. Caplin, J. Lyubina, L. F. Cohen, Dynamics of the first-order metamagnetic transition in magnetocaloric $La(Fe,Si)_{13}$: reducing hysteresis, Adv. Energy Mater. 5 (2015) 1401639. https://doi.org/10.1002/aenm.201401639.

[23] G. Li, R. Medapalli, J.H. Mentink, R.V. Mikhaylovskiy, T.G.H. Blank, S.K.K. Patel, A.K. Zvezdin, Th. Rasing, E.E. Fullerton, A.V. Kimel, Ultrafast kinetics of the antiferromagnetic-ferromagnetic phase transition in FeRh, Nat Commun. 13 (2022) 2998. https://doi.org/10.1038/s41467-022-30591-2.

[24] A. Aubert, K. Skokov, G. Gomez, A. Chirkova, I. Radulov, F. Wilhelm, A. Rogalev, H. Wende, O. Gutfleisch, K. Ollefs, Simultaneous multi-property probing during magneto-structural phase transitions: an element-specific and macroscopic hysteresis characterization at ID12 of the ESRF, IEEE Trans. Instrum. Meas. 71 (2022) 1–9. https://doi.org/10.1109/TIM.2022.3157001.

[25] F. Guillou, A.K. Pathak, D. Paudyal, Y. Mudryk, F. Wilhelm, A. Rogalev, V.K. Pecharsky, Non-hysteretic first-order phase transition with large latent heat and

giant low-field magnetocaloric effect, Nat Commun. 9 (2018) 2925. https://doi.org/10.1038/s41467-018-05268-4.

[26] V.K. Pecharsky, K.A. Gschneidner, Jr., Giant magnetocaloric effect in $Gd_5(Si_2Ge_2)$, Phys. Rev. Lett. 78 (1997) 4494–4497. https://doi.org/10.1103/PhysRevLett.78.4494.

[27] T. Krenke, E. Duman, M. Acet, E.F. Wassermann, X. Moya, L. Mañosa, A. Planes, Inverse magnetocaloric effect in ferromagnetic Ni–Mn–Sn alloys, Nat Mater. 4 (2005) 450–454. https://doi.org/10.1038/nmat1395.

[28] W. Hanggai, O. Tegus, H. Yibole, F. Guillou, Structural and magnetic phase diagrams of $MnFe_{0.6}Ni_{0.4}(Si,Ge)$ alloys and their giant magnetocaloric effect probed by heat capacity measurements, J. Magn. Magn. Mater. 494 (2020) 165785. https://doi.org/10.1016/j.jmmm.2019.165785.

[29] E. Liu, W. Wang, L. Feng, W. Zhu, G. Li, J. Chen, H. Zhang, G. Wu, C. Jiang, H. Xu, F. De Boer, Stable magnetostructural coupling with tunable magnetoresponsive effects in hexagonal ferromagnets, Nat Commun. 3 (2012) 873. https://doi.org/10.1038/ncomms1868.

[30] K. Mandal, D. Pal, N. Scheerbaum, J. Lyubina, O. Gutfleisch, Magnetocaloric effect in Ni–Mn–Ga alloys, IEEE Trans. Magn. 44 (2008) 2993–2996. https://doi.org/10.1109/TMAG.2008.2002481.

[31] X. Miao, Y. Gong, F. Zhang, Y. You, L. Caron, F. Qian, W. Guo, Y. Zhang, Y. Gong, F. Xu, N. Van Dijk, E. Brück, Enhanced reversibility of the magnetoelastic transition in $(Mn,Fe)_2(P,Si)$ alloys via minimizing the transition-induced elastic strain energy, J. Mater. Sci. Technol. 103 (2022) 165–176. https://doi.org/10.1016/j.jmst.2021.05.087.

[32] F. Guillou, H. Yibole, N.H. Van Dijk, L. Zhang, V. Hardy, E. Brück, About the mechanical stability of MnFe(P,Si,B) giant-magnetocaloric materials, J. Alloys Compd. 617 (2014) 569–574. https://doi.org/10.1016/j.jallcom.2014.08.061.

[33] Z.Q. Ou, L. Zhang, N.H. Dung, L. Caron, E. Brück, Structure, magnetism and magnetocalorics of Fe-rich $(Mn,Fe)_{1.95}P_{1-x}Si_x$ melt-spun ribbons, J. Alloys Compd. 710 (2017) 446–451. https://doi.org/10.1016/j.jallcom.2017.03.266.

[34] Z.Q. Ou, N.H. Dung, L. Zhang, L. Caron, E. Torun, N.H. Van Dijk, O. Tegus, E. Brück, Transition metal substitution in Fe_2P-based $MnFe_{0.95}P_{0.50}Si_{0.50}$ magnetocaloric compounds, J. Alloys Compd. 730 (2018) 392–398. https://doi.org/10.1016/j.jallcom.2017.09.315.

[35] J. Lai, B. Huang, X. Miao, N. Van Thang, X. You, M. Maschek, L. Van Eijck, D. Zeng, N. Van Dijk, E. Brück, Combined effect of annealing temperature and vanadium substitution for mangetocaloric $Mn_{1.2-x}V_xFe_{0.75}P_{0.5}Si_{0.5}$ alloys, J. Alloys Compd. 803 (2019) 671–677. https://doi.org/10.1016/j.jallcom.2019.06.239.

[36] S. Hu, X. Miao, J. Liu, Z. Ou, M. Cong, O. Haschuluu, Y. Gong, F. Qian, Y. You, Y. Zhang, F. Xu, E. Brück, Small hysteresis and giant magnetocaloric effect in Nb-substituted $(Mn,Fe)_2(P,Si)$ alloys, Intermetallics 114 (2019) 106602. https://doi.org/10.1016/j.intermet.2019.106602.

[37] F. Zhang, I. Batashev, N. Van Dijk, E. Brück, Effect of off-stoichiometry and Ta doping on Fe-rich (Mn,Fe)$_2$(P,Si) based giant magnetocaloric materials, Scr. Mater. 226 (2023) 115253. https://doi.org/10.1016/j.scriptamat.2022.115253.

[38] F. Zhang, P. Feng, A. Kiecana, Z. Wu, Z. Bai, W. Li, H. Chen, W. Yin, X. Yan, F. Ma, N.H. Van Dijk, E. Brück, Yang Ren, Achieving tunable high-performance giant magnetocaloric effect in hexagonal Mn-Fe-P-Si materials through different D-block doping, Adv. Funct. Mater. 2024, 2409270. https://doi.org/10.1002/adfm.202409270.

[39] D.M. Liu, H. Zhang, S.B. Wang, W.Q. Xiao, Z.L. Zhang, N. Tian, C.X. Liu, M. Yue, Q.Z. Huang, J.X. Zhang, J.W. Lynn, The effect of Al doping on the crystal structure and magnetocaloric behavior of $Mn_{1.2}Fe_{0.8}P_{1-x}Ge_x$ compounds, J. Alloys Compd. 633 (2015) 120–126. https://doi.org/10.1016/j.jallcom.2015.01.141.

[40] D.T. Cam Thanh, E. Brück, O. Tegus, J.C.P. Klaasse, K.H.J. Buschow, Influence of Si and Ge on the magnetic phase transition and magnetocaloric properties of MnFe(P,Si,Ge), J. Magn. Magn. Mater. 310 (2007) e1012–e1014. https://doi.org/10.1016/j.jmmm.2006.11.194.

[41] P. Wlodarczyk, L. Hawelek, M. Kowalczyk, M. Kaminska, P. Zackiewicz, M. Polak, M. Hreczka, A. Kolano-Burian, Impact of silicon doping on the magnetocaloric effect of $MnFeP_{0.35}As_{0.65}$ powder, Solid State Sci. 56 (2016) 23–28. https://doi.org/10.1016/j.solidstatesciences.2016.04.003.

[42] S. Kim, H. Shin, I. Chu, K. Lee, K.H. Lee, W. Lee, Tunable Curie temperature in $Mn_{1.15}Fe_{0.85}P_{0.55}Si_{0.45}$ via lattice engineering by Al addition, J. Alloys Compd. 890 (2022) 161798. https://doi.org/10.1016/j.jallcom.2021.161798.

[43] H. Yibole, F. Guillou, L. Zhang, N.H. Van Dijk, E. Brück, Direct measurement of the magnetocaloric effect in MnFe(P,X) (X=As,Ge,Si) materials, J. Phys. D: Appl. Phys. 47 (2014) 075002. https://doi.org/10.1088/0022-3727/47/7/075002.

[44] D. Pineda Quijano, C. Infante Ferreira, E. Brück, Layering strategies for active magnetocaloric regenerators using MnFePSi for heat pump applications, Appl. Therm. Eng. 232 (2023) 120962. https://doi.org/10.1016/j.applthermaleng.2023.120962.

[45] O. Beckman, L. Lundgren, P. Nordblad, P. Svedlindh, A. Törne, Y. Andersson, S. Rundqvist, Specific heat of the ferromagnet Fe_2P, Phys. Scr. 25 (1982) 679–681. https://doi.org/10.1088/0031-8949/25/6A/005.

[46] M. Hudl, D. Campanini, L. Caron, V. Höglin, M. Sahlberg, P. Nordblad, A. Rydh, Thermodynamics around the first-order ferromagnetic phase transition of Fe_2P single crystals, Phys. Rev. B 90 (2014) 144432. https://doi.org/10.1103/PhysRevB.90.144432.

[47] J. Cedervall, M.S. Andersson, E.K. Delczeg-Czirjak, D. Iuşan, M. Pereiro, P. Roy, T. Ericsson, L. Häggström, W. Lohstroh, H. Mutka, M. Sahlberg, P. Nordblad, P.P. Deen, Magnetocaloric effect in Fe_2P: Magnetic and phonon degrees of freedom, Phys. Rev. B 99 (2019) 174437. https://doi.org/10.1103/PhysRevB.99.174437.

[48] P. Roy, E. Brück, R.A. De Groot, Latent heat of the first-order magnetic transition of MnFeSi$_{0.33}$P$_{0.66}$, Phys. Rev. B 93 (2016) 165101. https://doi.org/10.1103/PhysRevB.93.165101.

[49] D. Bessas, M. Maschek, H. Yibole, J.-W. Lai, S.M. Souliou, I. Sergueev, A.I. Dugulan, N.H. Van Dijk, E. Brück, Lattice dynamics across the magnetic transition in (Mn,Fe)$_{1.95}$(P,Si), Phys. Rev. B 97 (2018) 094303. https://doi.org/10.1103/PhysRevB.97.094303.

[50] B. Wurentuya, S. Ma, B. Narsu, O. Tegus, Z. Zhang, Lattice dynamics of FeMnP$_{0.5}$Si$_{0.5}$ compound from first principles calculation, J. Mater. Sci. Technol. 35 (2019) 127–133. https://doi.org/10.1016/j.jmst.2018.09.009.

[51] K.P. Skokov, A.Yu. Karpenkov, D.Yu. Karpenkov, O. Gutfleisch, The maximal cooling power of magnetic and thermoelectric refrigerators with La(FeCoSi)$_{13}$ alloys, J. Appl. Phys. 113 (2013) 17A945. https://doi.org/10.1063/1.4801424.

[52] J. Lai, X. You, J. Law, V. Franco, B. Huang, D. Bessas, M. Maschek, D. Zeng, N. Van Dijk, E. Brück, Ultra-low hysteresis in giant magnetocaloric Mn$_{1-x}$V$_x$Fe$_{0.95}$(P,Si,B) compounds, J. Alloys Compd. 930 (2023) 167336. https://doi.org/10.1016/j.jallcom.2022.167336.

[53] N.V. Thang, H. Yibole, N.H. Van Dijk, E. Brück, Effect of heat treatment conditions on MnFe(P,Si,B) compounds for room-temperature magnetic refrigeration, J. Alloys Compd. 699 (2017) 633–637. https://doi.org/10.1016/j.jallcom.2016.12.402.

[54] F. Guillou, S. Liting, O. Haschuluu, Z.Q. Ou, E. Brück, O. Tegus, H. Yibole, Room temperature magnetic anisotropy in Fe$_2$P-type transition metal based alloys, J. Alloys Compd. 800 (2019) 403–411. https://doi.org/10.1016/j.jallcom.2019.05.327.

[55] H.M. Rietveld, The Rietveld method, Phys. Scr. 89 (2014) 098002. https://doi.org/10.1088/0031-8949/89/9/098002.

[56] J. Rodríguez-Carvajal, Recent advances in magnetic structure determination by neutron powder diffraction, Physica B: Condensed Matter 192 (1993) 55–69. https://doi.org/10.1016/0921-4526(93)90108-I.

[57] J.M. Sosa, D.E. Huber, B. Welk, H.L. Fraser, Development and application of MIPAR^{TM}: a novel software package for two- and three-dimensional microstructural characterization, Integr. Mater. Manuf. Innov. 3 (2014) 123–140. https://doi.org/10.1186/2193-9772-3-10.

[58] V. Hardy, Y. Bréard, C. Martin, Derivation of the heat capacity anomaly at a first-order transition by using a semi-adiabatic relaxation technique, J. Phys.: Condens. Matter 21 (2009) 075403. https://doi.org/10.1088/0953-8984/21/7/075403.

[59] M.F.J. Boeije, M. Maschek, X.F. Miao, N.V. Thang, N.H. Van Dijk, E. Brück, Mixed magnetism in magnetocaloric materials with first-order and second-order magnetoelastic transitions, J. Phys. D: Appl. Phys. 50 (2017) 174002. https://doi.org/10.1088/1361-6463/aa5db9.

[60] M. Maschek, X. You, M.F.J. Boeije, D. Chernyshov, N.H. Van Dijk, E. Brück, Charge redistribution and the magnetoelastic transition across the first-order

magnetic transition in (Mn,Fe)$_2$(P,Si,B), Phys. Rev. B 98 (2018) 224413. https://doi.org/10.1103/PhysRevB.98.224413.

[61] A. Pasko, A. Bartok, K. Zehani, L. Bessais, F. Mazaleyrat, M. LoBue, X-ray diffraction analysis of the magnetoelastic phase transition in the Mn-Fe-P-Si magnetocaloric alloy, AIP Advances 6 (2016) 056204. https://doi.org/10.1063/1.4943245.

[62] E.K. Delczeg-Czirjak, Z. Gercsi, L. Bergqvist, O. Eriksson, L. Szunyogh, P. Nordblad, B. Johansson, L. Vitos, Magnetic exchange interactions in B-, Si-, and As-doped Fe$_2$P from first-principles theory, Phys. Rev. B 85 (2012) 224435. https://doi.org/10.1103/PhysRevB.85.224435.

[63] Z. Gercsi, E.K. Delczeg-Czirjak, L. Vitos, A.S. Wills, A. Daoud-Aladine, K.G. Sandeman, Magnetoelastic effects in doped Fe$_2$P, Phys. Rev. B 88 (2013) 024417. https://doi.org/10.1103/PhysRevB.88.024417.

[64] M. Fries, L. Pfeuffer, E. Bruder, T. Gottschall, S. Ener, L.V.B. Diop, T. Gröb, K.P. Skokov, O. Gutfleisch, Microstructural and magnetic properties of Mn-Fe-P-Si (Fe$_2$P -type) magnetocaloric compounds, Acta Mater. 132 (2017) 222–229. https://doi.org/10.1016/j.actamat.2017.04.040.

[65] B. Suye, H. Yibole, W. Meijuan, B. Wurentuya, F. Guillou, Influence of the particle size on a MnFe(P,Si,B) compound with giant magnetocaloric effect, AIP Advances 13 (2023) 025203. https://doi.org/10.1063/9.0000371.

[66] B. Suye, H. Yibole, Z.Q. Song, B. Tana, W. Wei, O. Haschuluu, O. Tegus, F. Guillou, Influence of cold compaction pressure on intergranular secondary phase distribution and magnetocaloric/thermomagnetic performances of MnFe(P,Si,B) compounds, Journal of Alloys and Compounds 976 (2024) 172918. https://doi.org/10.1016/j.jallcom.2023.172918.

[67] T. Qianbai, H. Yibole, F. Guillou, Structure, Microstructure and Magnetocaloric/Thermomagnetic Properties at the Early Sintering of MnFe(P,Si,B) Compounds, Metals 14 (2024) 385. https://doi.org/10.3390/met14040385.

[68] A. Kiecana, I. Batashev, A.I. Dugulan, C. Kwakernaak, L. Pieter, F. Zhang, N.H. Van Dijk, E. Brück, Effect of Co and Ni doping on the structure, magnetic and magnetocaloric properties of Fe-rich (Mn,Fe)$_2$(P,Si) compounds, Journal of Magnetism and Magnetic Materials 561 (2022) 169710. https://doi.org/10.1016/j.jmmm.2022.169710.

[69] A. Kiecana, C. Kwakernaak, N.H. Van Dijk, E. Brück, Effect of the heat treatment on the microstructure, magnetism and magnetocaloric effect in Fe-rich (Mn,Fe)$_2$(P,Si) melt-spun ribbons, Journal of Alloys and Compounds 932 (2023) 167635. https://doi.org/10.1016/j.jallcom.2022.167635.

[70] R. Niemann, S. Hahn, A. Diestel, A. Backen, L. Schultz, K. Nielsch, M.F.-X. Wagner, S. Fähler, Reducing the nucleation barrier in magnetocaloric Heusler alloys by nanoindentation, APL Materials 4 (2016) 064101. https://doi.org/10.1063/1.4943289.

[71] A. Waske, L. Giebeler, B. Weise, A. Funk, M. Hinterstein, M. Herklotz, K. Skokov, S. Fähler, O. Gutfleisch, J. Eckert, Asymmetric first-order transition and

interlocked particle state in magnetocaloric La(Fe,Si)$_{13}$, Phys. Status Solidi RRL 9, No. 2, (2015) 136–140. https://doi.org/10.1002/pssr.201409484.

[72] J. Lyubina, R. Schäfer, N. Martin, L. Schultz, O. Gutfleisch, Novel Design of La(Fe,Si)$_{13}$ Alloys Towards High Magnetic Refrigeration Performance, Advanced Materials 22 (2010) 3735–3739. https://doi.org/10.1002/adma.201000177.

[73] F. Zhang, C. Taake, B. Huang, X. You, H. Ojiyed, Q. Shen, I. Dugulan, L. Caron, N.H. van Dijk, E. Brück, Magnetocaloric effect in the (Mn,Fe)$_2$(P,Si) system: From bulk to nano, Acta Mater. 224 (2022) 117532. https://doi.org/10.1016/j.actamat.2021.117532.

[74] K.A. GschneidnerJr, V.K. Pecharsky, A.O. Tsokol, Recent developments in magnetocaloric materials, Rep. Prog. Phys. 68 (2005) 1479–1539. https://doi.org/10.1088/0034-4885/68/6/R04.

[75] V.V. Khovaylo, K.P. Skokov, O. Gutfleisch, H. Miki, R. Kainuma, T. Kanomata, Reversibility and irreversibility of magnetocaloric effect in a metamagnetic shape memory alloy under cyclic action of a magnetic field, Appl. Phys. Lett. 97 (2010) 052503. https://doi.org/10.1063/1.3476348.

[76] K.P. Skokov, K.-H. Müller, J.D. Moore, J. Liu, A.Yu. Karpenkov, M. Krautz, O. Gutfleisch, Influence of thermal hysteresis and field cycling on the magnetocaloric effect in LaFe$_{11.6}$Si$_{1.4}$, J. Alloys Compd. 552 (2013) 310–317. https://doi.org/10.1016/j.jallcom.2012.10.008.

[77] A. Chirkova, K.P. Skokov, L. Schultz, N.V. Baranov, O. Gutfleisch, T.G. Woodcock, Giant adiabatic temperature change in FeRh alloys evidenced by direct measurements under cyclic conditions, Acta Mater. 106 (2016) 15–21. https://doi.org/10.1016/j.actamat.2015.11.054.

[78] V. Franco, J.S. Blázquez, A. Conde, Field dependence of the magnetocaloric effect in materials with a second order phase transition: A master curve for the magnetic entropy change, Appl. Phys. Lett. 89 (2006) 222512. https://doi.org/10.1063/1.2399361.

[79] J.Y. Law, V. Franco, L.M. Moreno-Ramírez, A. Conde, D.Y. Karpenkov, I. Radulov, K.P. Skokov, O. Gutfleisch, A quantitative criterion for determining the order of magnetic phase transitions using the magnetocaloric effect, Nat Commun. 9 (2018) 2680. https://doi.org/10.1038/s41467-018-05111-w.

[80] N.H. Van Dijk, Landau model evaluation of the magnetic entropy change in magnetocaloric materials, J. Magn. Magn. Mater. 529 (2021) 167871. https://doi.org/10.1016/j.jmmm.2021.167871.

[81] F. Guillou, R. Hamane, H. Yibole, J.Y. Xu, B. Narsu, V. Hardy, Heat capacity of a MnFe(P,Si,B) compound with first-order magnetic transition, J. Magn. Magn. Mater. 541 (2022) 168513. https://doi.org/10.1016/j.jmmm.2021.168513.

[82] H.E. Karaca, I. Karaman, B. Basaran, Y. Ren, Y.I. Chumlyakov, H.J. Maier, Magnetic field-induced phase transformation in NiMnCoIn magnetic shape-memory alloys—A new actuation mechanism with large work output, Adv. Funct. Mater. 19 (2009) 983–998. https://doi.org/10.1002/adfm.200801322.

[83] P. Sarkar, P. Mandal, A.K. Bera, S.M. Yusuf, L.S. Sharath Chandra, V. Ganesan, Field-induced first-order to second-order magnetic phase transition in $Sm_{0.52}Sr_{0.48}MnO_3$, Phys. Rev. B 78 (2008) 012415. https://doi.org/10.1103/PhysRevB.78.012415.

[84] X. You, M. Maschek, N.H.H. Van Dijk, E. Brück, Magnetic Phase Diagram of the $Mn_xFe_{2-x}P_{1-y}Si_y$ System, Entropy 24 (2021) 2. https://doi.org/10.3390/e24010002.

[85] F. Guillou, H. Yibole, B. Narsu, V. Hardy, Correlation between deformation and total entropy change at the first-order magnetic transition of Fe_2P-based magnetocaloric materials, Results Phys. 44 (2023) 106203. https://doi.org/10.1016/j.rinp.2022.106203.

[86] P. Roy, E. Torun, R.A. De Groot, Effect of doping and elastic properties in $(Mn,Fe)_2(Si,P)$, Phys. Rev. B 93 (2016) 094110. https://doi.org/10.1103/PhysRevB.93.094110.

[87] F. Guillou, H. Yibole, N.H. Van Dijk, E. Brück, Effect of boron substitution on the ferromagnetic transition of $MnFe_{0.95}P_{2/3}Si_{1/3}$, J. Alloys Compd. 632 (2015) 717–722. https://doi.org/10.1016/j.jallcom.2015.01.308.

[88] M. Yue, D. Liu, Q. Huang, T. Wang, F. Hu, J. Li, G. Rao, B. Shen, J.W. Lynn, J. Zhang, Structure evolution and entropy change of temperature and magnetic field induced magneto-structural transition in $Mn_{1.1}Fe_{0.9}P_{0.76}Ge_{0.24}$, J. Appl. Phys. 113 (2013) 043925. https://doi.org/10.1063/1.4788803.

[89] F. Zhang, I. Batashev, Q. Shen, Z. Wu, R.I. Smith, G.A. De Wijs, N. Van Dijk, E. Brück, Impact of F and S doping on $(Mn,Fe)_2(P,Si)$ giant magnetocaloric materials, Acta Mater. 234 (2022) 118057. https://doi.org/10.1016/j.actamat.2022.118057.

Supplementary Material for Chapter 4
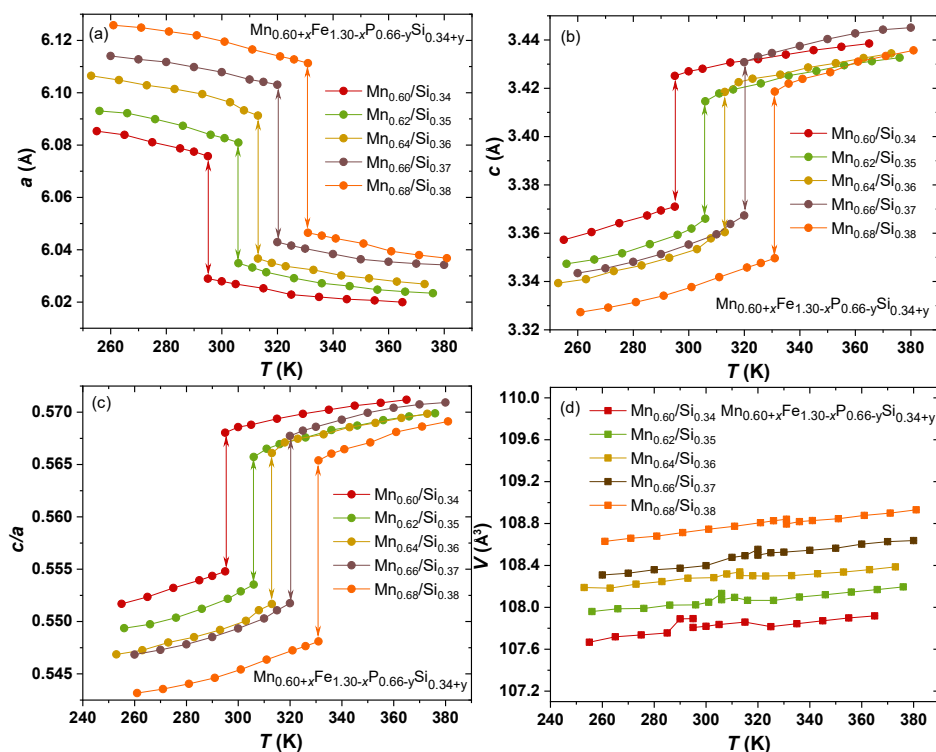
Fig. S4.1. Temperature dependence of the lattice parameters a, c, the ration c/a and the unit-cell volume (V) of the $Mn_{0.60+x}Fe_{1.3-x}P_{0.66-y}Si_{0.34+y}$ compounds derived from X-ray diffraction patterns measured upon heating at zero field $\mu_0H = 0$ T (arrows indicate the jump in lattice parameter in the two-phase region).
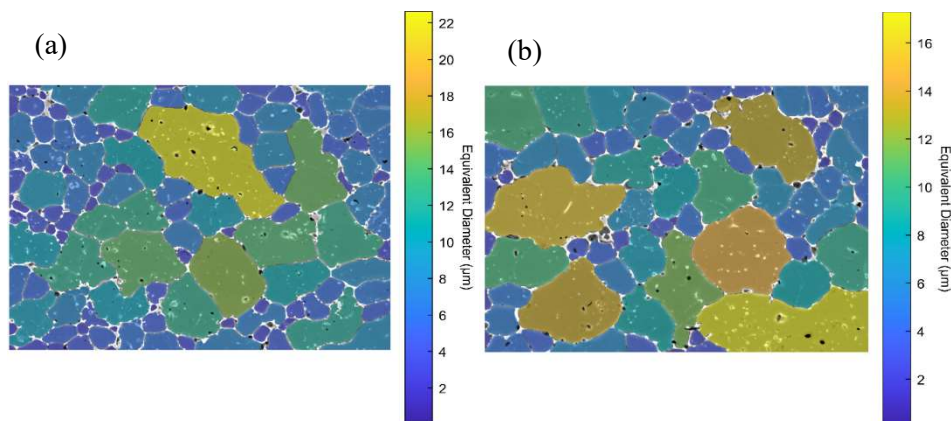

Fig. S4.2. SEM images of bulk ribbons of (a) $Mn_{0.60}Fe_{1.30}P_{0.66}Si_{0.34}$ and (b) $Mn_{0.68}Fe_{1.22}P_{0.62}Si_{0.38}$, sintered at 1100 °C for 24 h. The colour code indicating the equivalent diameter of each grain is superimposed on the images.
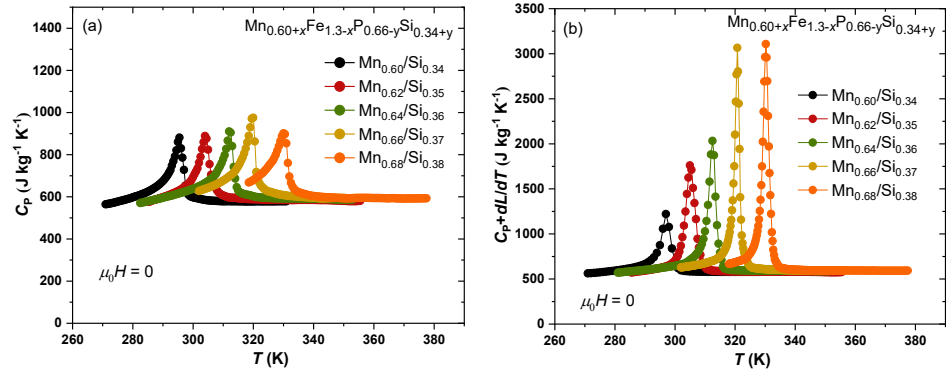
Fig. S4.3. (a) Specific heat only (C_p) of $Mn_{0.60+x}Fe_{1.3-x}P_{0.66-y}Si_{0.34+y}$ compounds at $\mu_0H = 0$ T. (b) Total specific heat ($C_p + dL/dT$) of $Mn_{0.60+x}Fe_{1.3-x}P_{0.66-y}Si_{0.34+y}$ compounds at $\mu_0H = 0$ T.
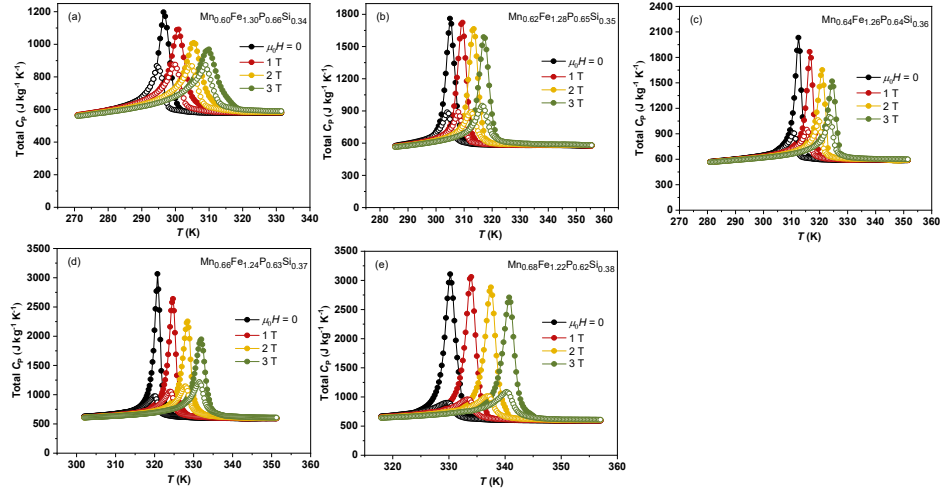
Fig. S4.4. Thermal and magnetocaloric properties of $Mn_{0.60+x}Fe_{1.3-x}P_{0.66-y}Si_{0.34+y}$ compounds. The two different types of heat capacity measurements represent $C_p + dL/dT$ (close symbols) and C_p without latent heat (open symbols) at applied fields of 0, 1, 2 and 3 T, respectively.

59
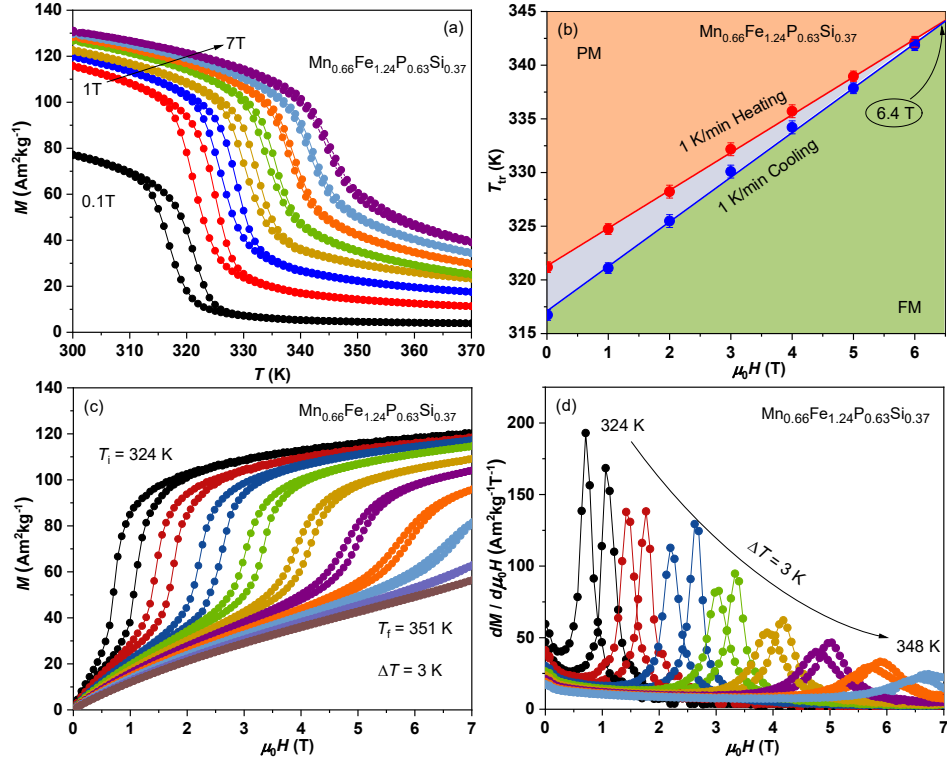
Fig. S4.5. (a) Temperature-dependent phase transition of the $Mn_{0.66}Fe_{1.24}P_{0.63}Si_{0.37}$ compound in applied fields ranging from 0.1 to 7 T. (b) Transition temperature T_{tr} versus applied field obtained from the inflection points of the heating and cooling $M(T)$ curves up to 6 T. (c) Field-induced transition of the $Mn_{0.66}Fe_{1.24}P_{0.63}Si_{0.37}$ compound at different temperatures (324-351 K). (d) Field derivative of the magnetization, $dM/d\mu_0H$, plotted as a function of the applied magnetic field.

Chapter 5

Bridging the gap between microscopic and macroscopic descriptions of the first-order magneto-elastic field-induced transition in $(Mn,Fe)_2(P,Si)$

Abstract

A first-order magnetic phase transition (FOMT) involves structural, magnetic and electronic changes that affect the crystal lattice defined by the unit cell. The FOMTs generally demonstrate dramatic changes in bulk physical properties such as the magnetization, thermal properties, and transport properties, which often form the basis of their applications. However, the intermediate microscopic length scale of the microstructure often remains widely unexplored and poorly described. To understand how the field induced paramagnetic-to ferromagnetic first-order magnetic phase transition in $(Mn,Fe)_2(P,Si)$ develops on different length scales X-ray magnetic circular dichroism (XMCD) measurements are conducted with an X-ray beam that could be focussed from a millimetre to a micrometre size. The micro-beam signals show significant differences compared to the macro-beam signal, indicating that the local field-induced transition varies substantially depending on the location. The XANES spectra at the K edge of both Mn and Fe are found to be temperature independent, particularly in the edge region. When the XMCD spectra at the K edge of Mn and Fe are compared for temperatures of 250 and 320 K across the FOMT, it is found that the spectral features of the XMCD spectra are largely unchanged, indicating that no valence change takes place for both Mn and Fe during the FOMT.

5.1 Introduction

$(MnFe)_2(P,Si)$ belongs to one of the rare material families presenting an isostructural first-order magnetic transition (FOMT) at the ferromagnetic (FM) to paramagnetic (PM) transition at ambient conditions. Since the discovery of their giant magnetocaloric effect [1–6], these materials attract continuing attention both for their potential applications and for the scientific interest to unravel the underlying mechanisms responsible for the FOMT. Experimental and theoretical studies have shown that the FOMT involves an anisotropic deformation of the hexagonal unit cell with a change in the lattice parameter ratio c/a of up to 10%. The change in c/a ratio at the FOMT is accompanied by an electronic structure reconstruction and an instability of the magnetic moments. The FOMT is reflected by a sharp change in magnetization, a large latent heat, a noticeable electrical resistivity anomaly and a giant magnetocaloric effect. The influence of microstructural features on the FOMT remains however largely unaddressed. Recent single-crystal magnetization measurements revealed magnetization jumps when the FOMT is crossed [7,8]. These steps fingerprint local burst-like developments of the FOMT. The lattice mismatch for a partial FM-to-PM transition necessarily generates strains at the FM-PM interfaces. The formation of elastic energy associated with the FOMT opposes the chemical driving force for the transition. For single crystals it was found that such metastable states can be particularly robust, and that the transition front between the two phases will only propagate further if sufficient additional driving force is applied (in the form of a temperature or field change).

Even though the basic origin of these steps is intrinsic (structural mismatch), the sample response necessary involves microstructural features, which are extrinsic. Due to a low defect concentration, the magnetization steps are prominent in single crystals and correspond to relatively large fractions being transformed at each event. In polycrystalline samples, the microstructure (secondary phases, porosity, grain boundaries, etc.) provides local features that affect how the FOMT progresses in space. While bulk macroscopic magnetization measurements on polycrystalline samples do not resolve individual steps due to averaging, the transition path is likely not linear and should also involve local burst-like conversions between the two magnetic states. No detailed description of how the transition develops is currently available for materials with a FOMT. Most of the available models and experimental studies neglect the role of the microstructure [9–11]. Previous studies on transport [12], magnetization [10], magneto-optical imaging [13], and X-ray microtomography and Hall probe imaging [14] have highlighted the role of magnetic interactions and their competing influence with strains during the FOMT in $La(Fe,Si)_{13}$ alloys.

However, extending these findings to $(Mn,Fe)_2(P,Si)$ compounds, which have a markedly different metallurgy and microstructure, still remains unexplored. A direct micrometre-scale observation of how the FOMT develops locally with a simultaneous comparison to the behaviour on the macroscopic length scale is therefore required. In this experiment we aim to gain new insights into the local evolution of the field-induced FOMT in $(Mn,Fe)_2(P,Si)$ by using the complementarity between the local magnetic contrast offered by a X-ray magnetic circular dichroism (XMCD) beam focussed to a micrometre length scale and simultaneous bulk physical property measurements.

5.2 Materials and Methods

A fresh batch of $Mn_{0.60}Fe_{1.30}P_{0.66}Si_{0.34}$ was synthesized by ball milling the elemental starting material powders, including Mn (99.7%), Fe (99.8%), Fe_2P (99.5 %), and Si (99.6%) at a ball-to-sample mass ratio of 5:1 for 10 hours at 380 rpm. Subsequently, the resulting powders were compacted into cylinders of approximately 2.5 g each, using a uniaxial press with a force of 8 tons. Then the pallets were melted and quenched by melt spinning with a copper-wheel speed of $v \approx 30$ m/s. The melt spun ribbons showed a width of the 2-3 mm and a thickness of 20-40 µm. After this, the as-cast ribbons were pressed into pallets with a diameter of 3 mm, sealed in quartz tubes filled with argon gas at a pressure of 200 millibars. Sintering of the samples took place in a vertical tube furnace, which had been preheated to 1100°C. This sintering process lasted for 2 hours before the samples were quenched in room temperature water. The sintering temperature of 1100°C was selected based on previous studies, which identified it as the optimal temperature for sintering [15,16]. Powder X-Ray Diffraction (XRD) was carried out on a PANalytical X-Pert PRO diffractometer, using Cu-K_α radiation with a wave length of 1.5405 Å (angular range 10°- 90°, angular step 0.02°, exposure time 1 s per step). Temperature-dependent XRD measurements were performed with an Anton Paar TTK450 temperature chamber. The Rietveld method [17], as implemented in the FullProf software, was used for the crystal structure refinement [18]. Scanning Electron Microscopy (SEM) measurements were conducted on polished pellets using a Nital etchant. For the grain size evaluation, about 15 SEM images per samples were analysed using the MIPAR software [19] for a quantitative estimate of the average grain size. The temperature- and field-induced magnetization was measured with a superconducting quantum interference device (Quantum Design MPMS XL) magnetometer, using the reciprocating sample option mode (RSO) to collect the magnetization data in the temperature range from 250 to 350 K with a constant sweep rate of 1 K/min and in applied magnetic fields up to 7 T. Isothermal

magnetization curves were recorded as a function of the field in a temperature sweep mode with a ±3 K variation from 294 to 324 K.

To remove the virgin effect for the FOMT, the samples were thermally cycled five times between liquid N_2 and room temperature. The X-ray absorption measurements were carried out on pellets of polycrystalline $Mn_{0.60}Fe_{1.30}P_{0.66}Si_{0.34}$ material. XAS and XMCD measurements were performed at the ID12 beamline of the European Synchrotron Radiation Facility, France [20]. The source was the helical undulator Hu52a or Hu38c at ID12 (Helios-II). The X-ray absorption spectra at the K edge of Mn and Fe were recorded using the total fluorescence yield detection mode in backscattering geometry. For the XMCD measurements, X-ray absorption spectra were collected consecutively for right and left circularly polarized X-rays with the external magnetic field flipped between -6 and 6 T at each energy point (the magnetic field was applied parallel to the direction of the X-ray beam).

5.3 Experimental Results and Discussion

Fig. 5.1 (a) presents powder XRD patterns for the sintered $Mn_{0.60}Fe_{1.30}P_{0.66}Si_{0.34}$ sample prepared using compacted ribbons. Rietveld refinement confirmed that the synthesized $Mn_{0.60}Fe_{1.30}P_{0.66}Si_{0.34}$ sample was single phase with the expected hexagonal symmetry (space group P-$62m$) phase. No secondary phase was detected. The X-ray diffraction patterns were recorded in the PM state at $T = 400$ K to avoid the coexistence of FM and PM states at room temperature. SEM measurements coupled with EDS confirmed that the synthesized $Mn_{0.60}Fe_{1.30}P_{0.66}Si_{0.34}$ samples were single-phase. The grain size distribution of the hexagonal $Mn_{0.60}Fe_{1.30}P_{0.66}Si_{0.34}$ sample shows a log-normal distribution, with an average size of about 8 μm, as shown in Fig. 5.1(b). A significant amount of porosity (5-6%) is visible in the SEM images, which is commonly observed in compacted samples [21,22].


64
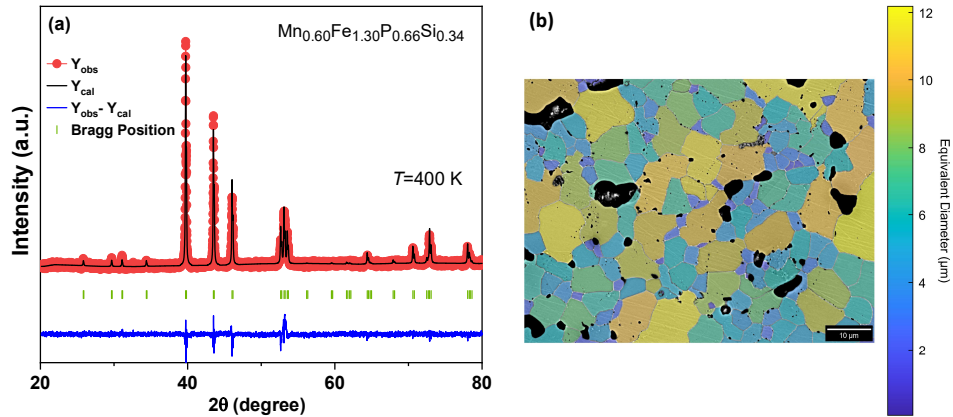
Fig. 5.1. (a) Powder XRD pattern collected at 400 K for the $Mn_{0.60}Fe_{1.30}P_{0.66}Si_{0.34}$ compound. (b) Microstructure of the $Mn_{0.60}Fe_{1.30}P_{0.66}Si_{0.34}$ sample sintered at 1100 °C for 2 h. The colour code highlights the equivalent diameter of each grain. Black regions indicate the pores.

To establish the temperature (T) and field (μ_0H) dependence of the FOMT, we have first analysed the temperature-dependent magnetization M for different fields μ_0H. As shown in Fig. 5.2(a) it is clear that the ferromagnetic transition is sharp in low field and gradually loses its sharpness for increasing fields. The applied magnetic field stabilises the ferromagnetic order, causing a shift in Curie temperature (T_C) to higher temperatures, as shown in Fig. 5.2(b). To quantitatively describe the FOMT, we derived the thermal hysteresis (ΔT_{hys}) from the difference in dM/dT between heating and cooling, and determined the full width at half maximum (*FWHM*) from dM/dT at different fields, as shown in the insert of Fig. 5.2(b). The value of ΔT_{hys} decreases linearly with the applied magnetic field and vanished at 5.2 T, while the *FWHM* increases linearly up to $\mu_0H = 4$ T, after which it increases sharply due to the broadening of the transition. These results indicate that $\mu_0H_{cr} = 5.2$ T is the critical field where the nature of the magnetic phase transition changes. The field-induced steplike jump in M together with the hysteresis are key characteristics of the FOMT, as shown in Fig. 5.2c. For increasing magnetic field (and increasing temperature) the jump progressively reduces in size, and vanishes at the critical end point for the PM-FM phase line.

Theoretical calculations indicate that quenched Fe moments in the PM state near the FM phase transition induce short-range order, resulting in an inhomogeneous state. When a external magnetic force is applied in this PM state with short-range order, it can potentially induce FM order. This transition causes a redistribution of electron density, favouring the magnetically ordered state (FM) from the unordered state (PM), results in a distinct change in the c/a ratio during this process. The field derivative, $dM/d\mu_0H$, clearly shows that the hysteresis gradually vanishes beyond 5.6 T, as illustrated in Fig. 5.2(d). This indicates that the system possesses a critical end point $\mu_0H_{cr} = 5.2$-5.6 T, that separates the boundary between a PM-FM phase line with a FOMT (with hysteresis) and a supercritical state (without hysteresis). The overall behaviour agrees with previous observations that the FOMT features disappear above the critical point [21]. As the estimates for the critical field from the hysteresis in temperature and field slightly differ, some uncertainty is unavoidable.
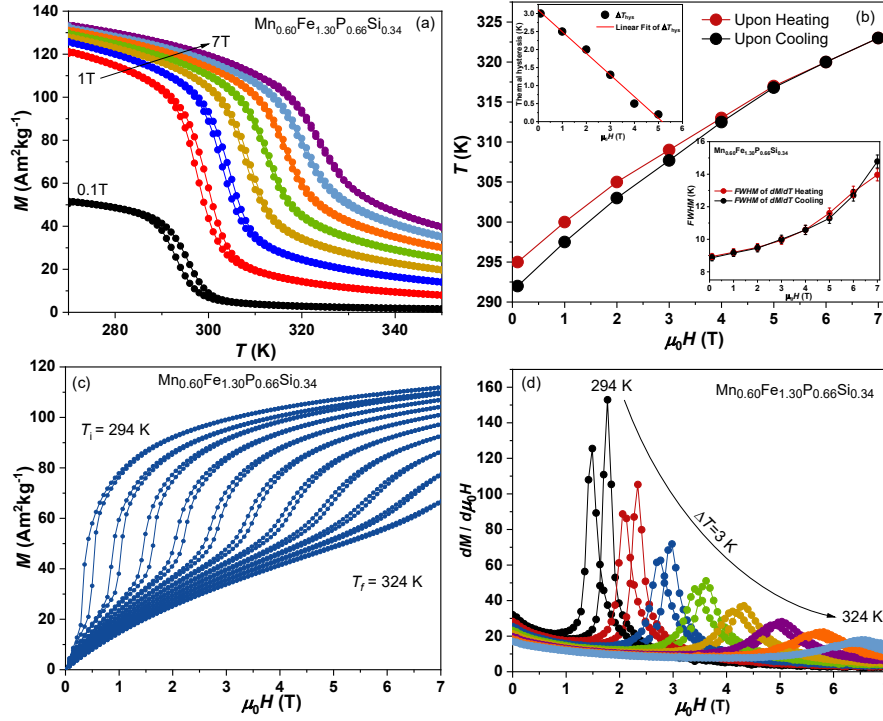
Fig. 5.2. (a) Temperature-dependent phase transition of the $Mn_{0.60}Fe_{1.30}P_{0.66}Si_{0.34}$ compound in applied fields ranging from 0.1 to 7 T. (b) Transition temperature as a function of the applied field during heating and cooling. The inset shows the variation of thermal hysteresis with the applied magnetic field, along with the full width at half maximum (*FWHM*) of dM/dT in relation to the field. (c) Field-induced transition of the $Mn_{0.60}Fe_{1.30}P_{0.66}Si_{0.34}$ compound at different temperatures (294-324 K). (d) Field derivative of the magnetisation, $dM/d\mu_0H$, plotted against the applied magnetic field.

Through the analysis of the structural and magnetic properties, we have gained valuable insight into the bulk physical properties. However, bridging the gap between atomic and macroscopic descriptions still requires investigation at the intermediate scales. A key focus point is understanding how the field-induced transition evolves locally. To address this, we utilized X-ray absorption spectroscopy (XAS) to conduct XMCD measurements with both macro- and micro-beams, enabling a deeper investigation of the local field-induced transitions. Fig. 5.3(a,b) illustrates the XAS spectra recorded in an applied magnetic field of 6 T below (FM state) and above (PM state) the FOMT. The XANES spectra at the *K* edge of both Fe and Mn are found to be temperature independent. In the rising edge region pre-edge structures are absent. When the XMCD spectra at *K* edge of Mn and Fe at temperatures of 250 and 320 K are compared, it is found that the maxima in the XMCD signals remain at the same energy and that the spectral features remain roughly the same, as illustrated in

66

Fig. 5.3(c,d). This observation indicates that there is no valence change for Mn and Fe across the FOMT, which is in good agreement with previous findings reported by Guillou et al. [23]. Furthermore, it indicates that the $4p$ states of both Fe and Mn are not significantly affected by the FOMT. In contrast, Guillou et al. [23] reported that the XAS at the P K edge ($1s{\rightarrow}3p$) was strongly modified across the FOMT, providing another key indicator for the electronic changes at the transition [23]. Both the Fe and Mn XMCD signals become weaker at high temperature and thereby mimic the temperature dependence of the magnetization.

Based on these pre-characteristics, we focused on studying the field-induced transition through field-dependent XMCD measurements at fixed energy and temperature, along with simultaneous (Hall probe) magnetisation and (strain gauge) magnetostriction measurements on the $Mn_{0.60}Fe_{1.30}P_{0.66}Si_{0.34}$ polycrystalline sample. Fig. 5.4 compares the field-dependent XMCD signal at the Fe K edge using a large beam ($500{\times}500~\mu m^2$), along with simultaneous Hall magnetometry and bulk SQUID magnetometry measurements on the $Mn_{0.60}Fe_{1.30}P_{0.66}Si_{0.34}$ polycrystalline sample at 305 K. After normalizing all signals, a good overall agreement for the amplitude of the FOMT is observed between XMCD and the macroscopic magnetic properties. Magnetostriction measurements of the strain as a function of the applied magnetic field show a similar profile, with a weaker relative field dependence in the low field region ($\leq$ 1.5 T). The magnetic response in this field range originates from the susceptibility of the paramagnetic state. The relatively low magnetostriction in the paramagnetic state signals a weak magneto-elastic coupling in this state.
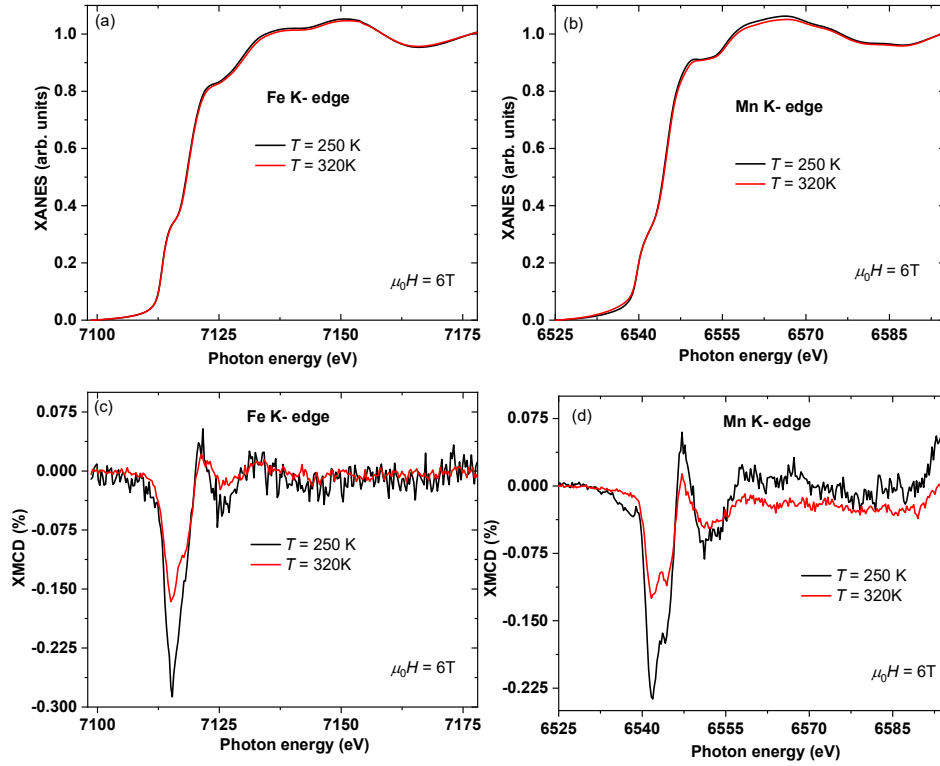
Fig. 5.3. (a),(b) XANES spectra for $Mn_{0.60}Fe_{1.30}P_{0.66}Si_{0.34}$ at $T = 250$ K (black) and 320 K (red) at the K edge of Fe and Mn, respectively. (c),(d) XMCD spectra for $Mn_{0.60}Fe_{1.30}P_{0.66}Si_{0.34}$ at $\mu_0H = 6$ T for the K edge of Mn and Fe, respectively. The XMCD signal is normalized to the edge jump.
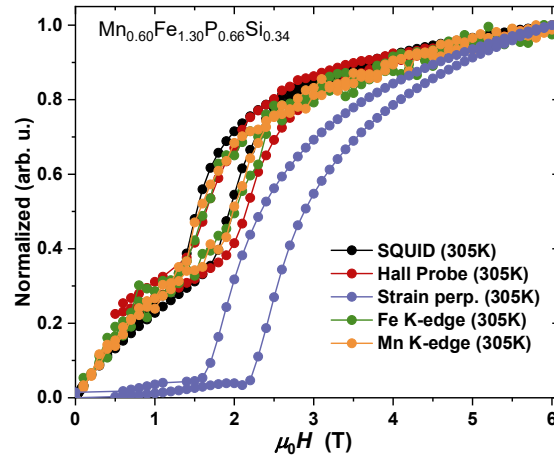

Fig. 5.4. Comparison of the large beam field-induced transition probed by XMCD at the K edge of Fe and Mn together with simultaneous Hall probe magnetisation and magnetostriction (strain as a function of field) measurements for the $Mn_{0.60}Fe_{1.30}P_{0.66}Si_{0.34}$ polycrystal sample.

To investigate the local field-induced transition, the beam size was reduced to a micro-beam (5×5 µm^2) and the field dependence of the XMCD was recorded at 11 individual spots within the large beam area, as shown in Fig. 5.5. The micro-beam signals show a significantly different profile in terms of the hysteresis and critical field of the FOMT at different spots, which is incompatible with the macro-beam signal. This indicates that the local field-induced transition varies substantially depending on the location. To identify the causes of these differences, we are considering the following factors: (*i*) variations in local chemical composition, (*ii*) different relative grain orientation and (*iii*) different strain levels. The small beam positions are visible in the SEM image due to local changes in colour. EDS mapping and line scans of the elemental analysis at each spot showed no differences in chemical composition, with a uniform distribution of Fe, Mn, P, and Si, as show in Fig. 5.6. It was found that surface carbon deposition caused the colour change observed on the surface. Complementary electron backscatter diffraction (EBSD) mapping is shown in Fig. S5.1 (Supplementary Information). The grain orientation map clearly indicates that reddish regions are close to the *c*-axis orientation, while bluish regions correspond to the *ab*-plane orientation. The inverse pole figure suggests a slight preferential orientation toward the *c*-axis. In contrast, the ribbon samples exhibit a random orientation, as shown in Fig. S5.2 (Supplementary Information). However, addressing possibilities (*ii*) and (*iii*) based on the EBSD results is challenging, as some grain sizes are similar to the micro-beam size, resulting in multiple grains involved within a micro-beam area. Nonetheless, we believe that the grain orientation and strain levels in different grains play a significant role in the local field-induced transition.

Fig. 5.7 also shows the sum of the micro-beam signals which is in reasonable agreement with the macro-beam signal, demonstrating that the average of these 11 spots is representative for the macro-beam signal and the macroscopic magnetic properties. However, for some spots the noise level was on par with the XMCD signal, likely due to the presence of holes or other surface imperfections in the microstructure. For a complete reconstruction of the macroscopic magnetic properties additional micro-beam measurements would be required to cover the complete surface area of the macro-beam measurements.
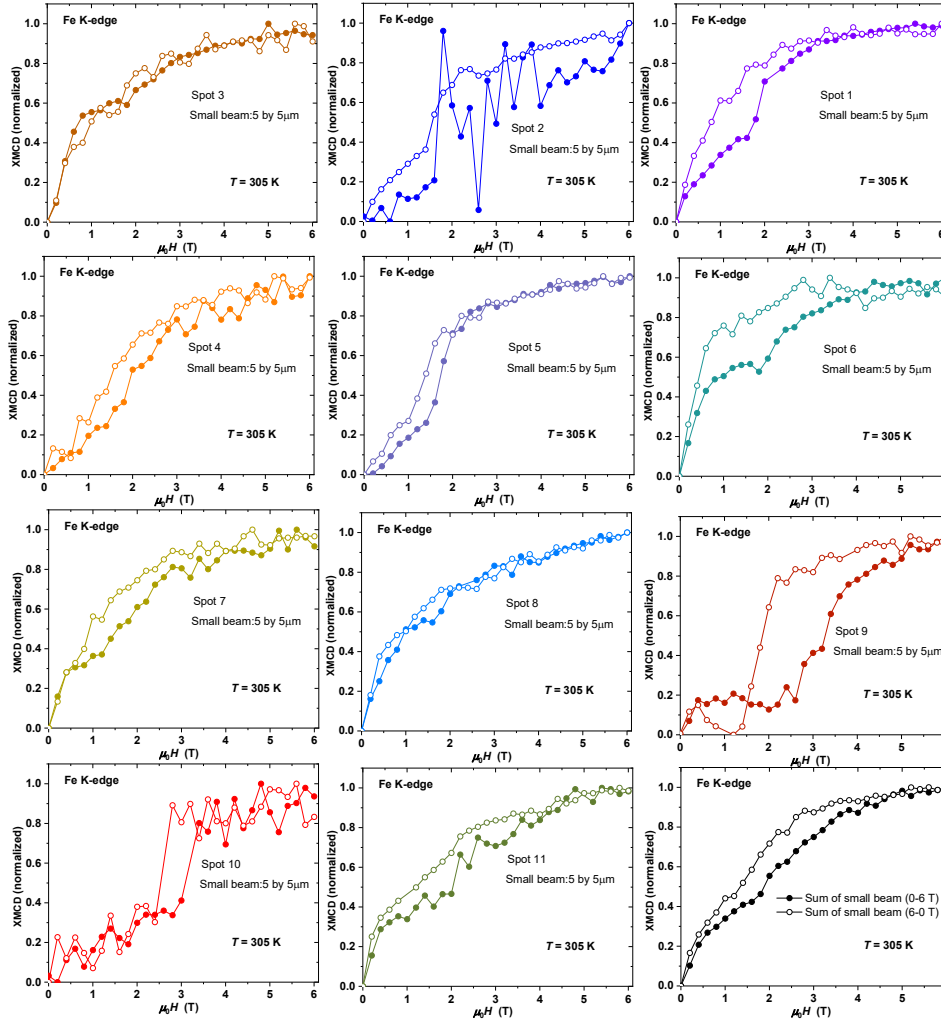
Fig. 5.5. Field-dependent XMCD signals of 11 individual spots at the Fe K edge, using a small beam (5×5 μm^2) at fixed energy (7.115 keV) and fixed temperature (305 K), along with the normalised sum of the XMCD signals from all spots.
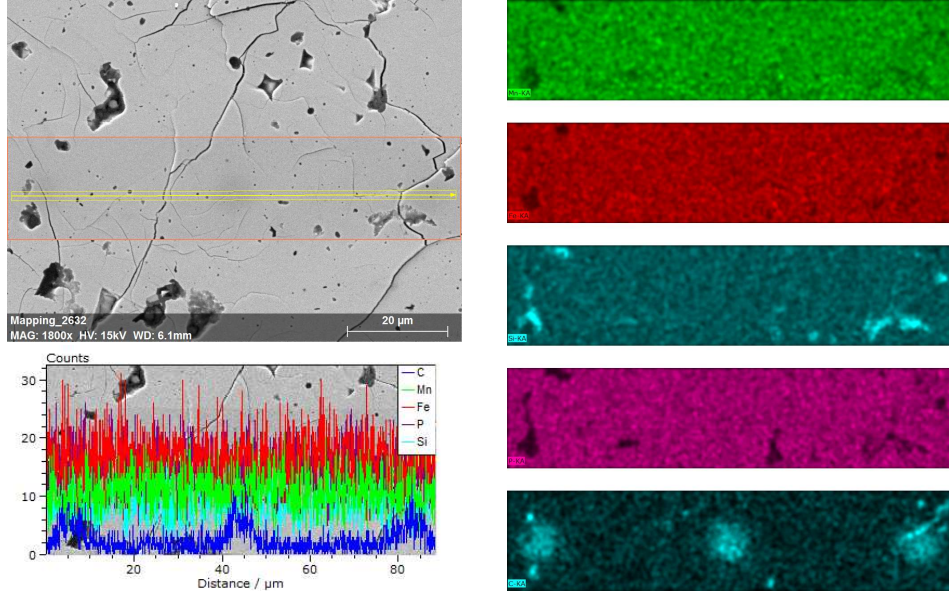
Fig. 5.6. Energy dispersive X-ray spectroscopy (EDS) mapping of the elemental analysis, showing the distribution of Mn, Fe, P, Si and C.
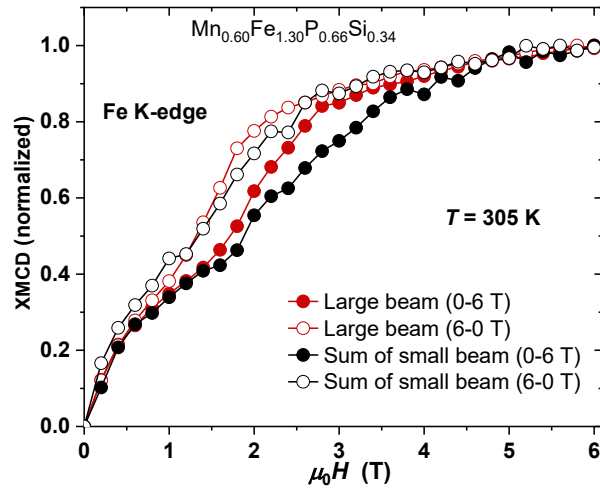
Fig. 5.7. Large beam XMCD signal compared with the reconstructed XMCD signal from small beam for the field-induced transition in $Mn_{0.60}Fe_{1.30}P_{0.66}Si_{0.34}$.

5.4 Conclusions

We have investigated the field-induced transition in the first-order magneto-elastic ferromagnetic transition of a polycrystalline Fe_2P-based $Mn_{0.60}Fe_{1.30}P_{0.66}Si_{0.34}$ sample. To uncover the underlying mechanisms connecting the microscopic and macroscopic physical properties during the field-induced transition, we performed comprehensive simultaneous experiments, including polarized X-ray absorption measurements combined with simultaneous Hall probe magnetometry, magnetostriction and bulk SQUID magnetometry on the $Mn_{0.60}Fe_{1.30}P_{0.66}Si_{0.34}$ polycrystalline sample. The temperature-induced and field-induced transitions up to 7 T indicate the presence of a critical end point at an applied field of 5.2–5.6 T, where the first-order magneto-elastic transition changes into a supercritical state without hysteresis. The field-dependent XMCD signal from several micro-beams and a macro-beam shows significant differences, suggesting that the mechanisms of the field-induced transition strongly depends on the local conditions, like the grain orientation, variations in chemical composition and local strain. It is found that the reconstruction based on the sum of 11 spots is quantitively representative of the macro-beam signal and the macroscopic bulk magnetic properties. Further complementary research is needed to fully understand the observed local variation in behaviour in detail.

References

[1] O. Tegus, E. Brück, K.H.J. Buschow, F.R. De Boer, Transition-metal-based magnetic refrigerants for room temperature applications, Nature 415 (2002) 150–152. https://doi.org/10.1038/415150a.

[2] N.H. Dung, L. Zhang, Z.Q. Ou, E. Brück, Magnetoelastic coupling and magnetocaloric effect in hexagonal Mn-Fe-P-Si compounds, Scripta Materialia 67 (2012) 975–978. https://doi.org/10.1016/j.scriptamat.2012.08.036.

[3] N.H. Dung, Z.Q. Ou, L. Caron, L. Zhang, D.T.C. Thanh, G.A. De Wijs, R.A. De Groot, K.H.J. Buschow, E. Brück, Mixed Magnetism for Refrigeration and Energy Conversion, Adv. Energy Mater. 1 (2011) 1215–1219. https://doi.org/10.1002/aenm.201100252.

[4] H. Yibole, F. Guillou, L. Zhang, N.H. Van Dijk, E. Brück, Direct measurement of the magnetocaloric effect in MnFe-(P,X)(X=As,Ge,Si) materials, J. Phys. D: Appl. Phys. 47 (2014) 075002. https://doi.org/10.1088/0022-3727/47/7/075002.

[5] F. Guillou, H. Yibole, G. Porcari, L. Zhang, N.H. Van Dijk, E. Brück, Magnetocaloric effect, cyclability and coefficient of refrigerant performance in the MnFe(P, Si, B) system, J. Appl. Phys. 116 (2014) 063903. https://doi.org/10.1063/1.4892406.

[6] F. Guillou, H. Yibole, A. Kamantsev, G. Porcari, J. Cwik, V. Koledov, N.H. Van Dijk, E. Brick, Field Dependence of the Magnetocaloric Effect in MnFe(P,Si) Materials, IEEE Trans. Magn. 51 (2015) 1–4. https://doi.org/10.1109/TMAG.2015.2445975.

[7] H. Yibole, F. Guillou, Y.K. Huang, G.R. Blake, A.J.E. Lefering, N.H. Van Dijk, E. Brück, First-order ferromagnetic transition in single-crystalline $(Mn,Fe)_2(P,Si)$, Appl. Phys. Lett. 107 (2015) 162403. https://doi.org/10.1063/1.4934500.

[8] L.L. Bao, W. Meijuan, H. Yibole, Z.Q. Ou, F. Guillou, Magnetization steps at the ferromagnetic transition of $(Mn,Fe)_2(P,Si)$ single crystals, J. Alloys Compd. 970 (2024) 172612. https://doi.org/10.1016/j.jallcom.2023.172612.

[9] T. Gottschall, D. Benke, M. Fries, A. Taubel, I.A. Radulov, K.P. Skokov, O. Gutfleisch, A matter of size and stress: understanding the first-order transition in materials for solid-state refrigeration, Adv. Funct. Materials 27 (2017) 1606735. https://doi.org/10.1002/adfm.201606735.

[10] E. Lovell, A.M. Pereira, A.D. Caplin, J. Lyubina, L.F. Cohen, Dynamics of the first-order metamagnetic transition in magnetocaloric $La(Fe,Si)_{13}$: reducing hysteresis, Adv. Energy Mater. 5 (2015) 1401639. https://doi.org/10.1002/aenm.201401639.

[11] A. Waske, L. Giebeler, B. Weise, A. Funk, M. Hinterstein, M. Herklotz, K. Skokov, S. Fähler, O. Gutfleisch, J. Eckert, Asymmetric first-order transition and interlocked particle state in magnetocaloric $La(Fe,Si)_{13}$, Phys. Status Solidi RRL 9, No. 2, (2015) 136–140. https://doi.org/10.1002/pssr.201409484.

[12] A. Fujita, T. Kondo, M. Kano, H. Yako, Shape-anisotropic heterogeneous nucleation and magnetic Gibbs-Thomson effect in itinerant-electron metamagnetic transition of $La(Fe_{0.88}Si_{0.12})_{13}$ magnetocaloric compound, Appl. Phys. Lett. 102 (2013) 041913. https://doi.org/10.1063/1.4789902.

[13] C. Bennati, F. Laviano, G. Durin, E.S. Olivetti, V. Basso, G. Ghigo, M. Kuepferling, Local magnetic behavior across the first order phase transition in $La(Fe_{0.9}Co_{0.015}Si_{0.085})_{13}$
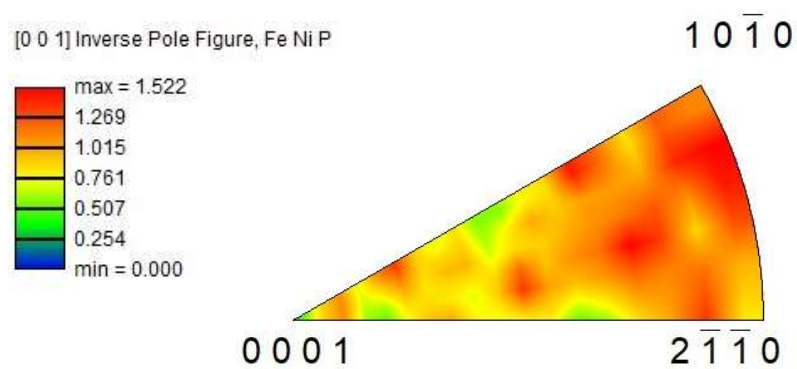
magnetocaloric compound, J. Magn. Magn. Mater. 400 (2016) 339–343. https://doi.org/10.1016/j.jmmm.2015.07.105.

[14] A. Waske, E. Lovell, A. Funk, K. Sellschopp, A. Rack, L. Giebeler, P.F. Gostin, S. Fähler, L.F. Cohen, The impact of surface morphology on the magnetovolume transition in magnetocaloric $LaFe_{11.8}Si_{1.2}$, APL Materials 4 (2016) 106101. https://doi.org/10.1063/1.4963840.

[15] N.V. Thang, H. Yibole, N.H. Van Dijk, E. Brück, Effect of heat treatment conditions on MnFe(P,Si,B) compounds for room-temperature magnetic refrigeration, J. Alloys Compd. 699 (2017) 633–637. https://doi.org/10.1016/j.jallcom.2016.12.402.

[16] F. Guillou, S. Liting, O. Haschuluu, Z.Q. Ou, E. Brück, O. Tegus, H. Yibole, Room temperature magnetic anisotropy in Fe_2P-type transition metal based alloys, J. Alloys Compd. 800 (2019) 403–411. https://doi.org/10.1016/j.jallcom.2019.05.327.

[17] H.M. Rietveld, A profile refinement method for nuclear and magnetic structures, J .Appl. Crystallogr. 2 (1969) 65–71. https://doi.org/10.1107/S0021889869006558.

[18] J. Rodríguez-Carvajal, Recent advances in magnetic structure determination by neutron powder diffraction, Physica B: Condensed Matter 192 (1993) 55–69. https://doi.org/10.1016/0921-4526(93)90108-I.

[19] J.M. Sosa, D.E. Huber, B. Welk, H.L. Fraser, Development and application of MIPAR™: a novel software package for two- and three-dimensional microstructural characterization, Integr. Mater. Manuf. Innov. 3 (2014) 123–140. https://doi.org/10.1186/2193-9772-3-10.

[20] A. Rogalev, F. Wilhelm, J. Goulon, G. Goujon, Magnetism and synchrotron radiation: towards the fourth generation light sources, Springer Proc. Phys. 151 (2013) 289–312. https://doi.org/10.1007/978-3-319-03032-6.

[21] M. Fries, L. Pfeuffer, E. Bruder, T. Gottschall, S. Ener, L.V.B. Diop, T. Gröb, K.P. Skokov, O. Gutfleisch, Microstructural and magnetic properties of Mn-Fe-P-Si (Fe_2P-type) magnetocaloric compounds, Acta Materialia 132 (2017) 222–229. https://doi.org/10.1016/j.actamat.2017.04.040.

[22] B. Suye, H. Yibole, Z.Q. Song, B. Tana, W. Wei, O. Haschuluu, O. Tegus, F. Guillou, Influence of cold compaction pressure on intergranular secondary phase distribution and magnetocaloric/thermomagnetic performances of MnFe(P,Si,B) compounds, J. Alloys Compd. 976 (2024) 172918. https://doi.org/10.1016/j.jallcom.2023.172918.

[23] F. Guillou, K. Ollefs, F. Wilhelm, A. Rogalev, A.N. Yaresko, H. Yibole, N.H. Van Dijk, E. Brück, Electronic and magnetic properties of phosphorus across the first-order ferromagnetic transition of $(Mn,Fe)_2(P,Si,B)$ giant magnetocaloric materials, Phys. Rev. B 92 (2015) 224427. https://doi.org/10.1103/PhysRevB.92.224427.

Supplementary Material for Chapter 5
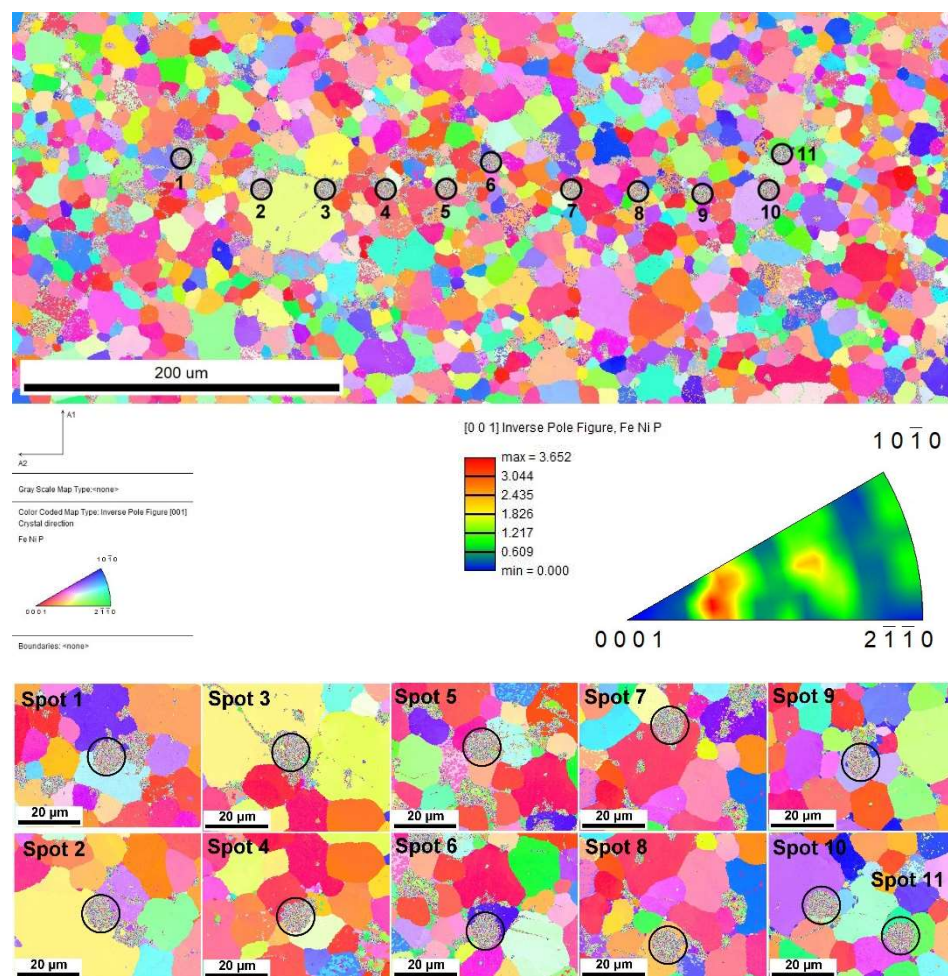
Fig. S5.1 Electron backscatter diffraction (EBSD) map including all 11 spots, along with the inverse pole figure of the $Mn_{0.60}Fe_{1.30}P_{0.66}Si_{0.34}$ polycrystalline sample.

[0 0 1] Inverse Pole Figure, Fe Ni P

max = 1.522
1.269
1.015
0.761
0.507
0.254
min = 0.000

$10\bar{1}0$

0001

$2\bar{1}\bar{1}0$

Fig. S5.2 The inverse pole figure of the $Mn_{0.60}Fe_{1.30}P_{0.66}Si_{0.34}$ ribbon sample.

Chapter 6

Structural and magnetic properties of YNi$_{4-x}$Co$_x$Si alloys

Abstract

The transition-metal based alloy system YNi$_{4-x}$Co$_x$Si shows a second-order ferromagnetic-to-paramagnetic transition near room temperature. Here, the magnetic structure, the magnetocaloric properties and the magnetic anisotropy of YNi$_{4-x}$Co$_x$Si (x = 0-4) are investigated. For x = 3.5, 3.75 and 4.0 a Curie temperature near room temperature is observed with T_C = 250, 283 and 310 K, respectively. In orientated YNi$_{4-x}$Co$_x$Si powder samples the c axis of the hexagonal crystal structure is found to be the easy magnetic axis, with a large dominant K_2 anisotropy constant ($K_2 > K_1 > 0$). The magnetic structure and the preferred atomic position for Ni are demonstrated by neutron diffraction measurements. We have found a dramatic decrease in the magnetic moment at the 3g site in the CaCu$_5$-type structure (space group $P6/mmm$), the saturation magnetization and the Curie temperature with increasing Ni concentration.

6.1 Introduction

Rare-earth alloys can exhibit both a large magnetocaloric effect and hard-magnetic properties [1-5]. The RM_4Si alloys, where R is a rare-earth element (La, Tb, Gd, Y, Tm) and M a $3d$ transition-metal element (Fe, Co, Ni), form a rich materials family with intriguing physics, including a giant magnetic coercivity, a large magnetocaloric effect and good hydrogen storage properties [6]. The hexagonal CaCu$_5$-type structure (space group $P6/mmm$) shows for some compounds an hexagonal-to-orthorhombic distortion into the orthorhombic YNi$_4$Si-type lattice (space group $Cmmm$), which is a potential route to optimize the magnetocaloric effect [7]. The relation between the lattice parameter in the orthorhombic (O) YNi$_4$Si-type lattice and the hexagonal (H) CaCu$_5$-type lattice is $b_O = (\sqrt{3}\, a_H)$ [8]. In recent years, TbNi$_4$Si (T_C = 30 K) and GdNi$_4$Si (T_C = 25 K) alloys are reported to show a giant magnetocaloric effect (MCE) at low temperatures [9], but their giant MCE is not optimized to room temperature. In the RNi$_4$Si alloy series a maximum isothermal entropy change was reported to be $|\Delta S_{max}|$ = 9.95 J kg^{-1} K^{-1} for TbNi$_4$Si and $|\Delta S_{max}|$ = 12.8 J kg^{-1} K^{-1} for GdNi$_4$Si in a field change of 5 T [9]. These reports have received much attention for their potential use in green energy-efficient magnetic refrigeration technology and magnetic heat pump applications. In order to make use of this giant MCE in applications, several challenges need to be dealt with: (1) the cost of heavy rare-earth elements brings one of the main challenges for applications, (2) large magnetic field changes are required to achieve the reported MCE effect, (3) the maximum adiabatic temperature changes at the ferromagnetic transition temperature need to be brought near room temperature. Considering the pronounced sensitivity of the structural and magnetic properties of RM_4Si materials to alloying, it is reasonable to anticipate that these drawbacks can be mitigated through careful adjustment of the chemical composition. First, in the heavy rare-earth ferromagnetic orthorhombic ternary alloys with M = Ni, such as GdNi$_4$Si or DyNi$_4$Si, Gd and Dy occupy the pyramidal sites and carry most of the magnetic moments 7.94 μ_B (Gd) and 10.65 μ_B (Dy), while Ni only carries 0.57 and 0.63 μ_B, respectively [17]. However, in the light rare-earth YNi$_4$Si compound, the theoretical magnetic moment of Y is zero, while the Ni magnetic moment of the above compound is 0.80 μ_B [6]. In order to maximize the magnetic density and the MCE, substitutions with heavy rare-earth elements such as Gd, Dy, Tb should be avoided. Second, in the series of alloys with R fixed to unity, extensive investigations have been carried out on the RNi$_{4-x}T_x$Si (T = Co, Fe, Cu, Mn) compounds [9]. The coupling between the $3d$ transition metals has been identified as a significant factor affecting the magnetic and structural transitions. However, the specific magnetic properties and structural transformations resulting from variations in the ratio of different $3d$ elements remains unclear. Recent research

involving the substitution of heavy rare-earth elements (R) has demonstrated relatively high values for the magnetic saturation polarization ($J_s = \mu_0 M_s$) and the maximum energy product $(BH)_{max}$ at low temperatures [6, 9], accompanied by uniaxial magnetic anisotropy [13]. These properties are essential for permanent magnets. Nevertheless, it is important to note that the temperature dependence of magnetization indicates a complex magnetic transition occurring below the Curie temperature [9].

On the other hand, the effect of substituting Si or Al for one of the Co atoms in YCo$_5$ has been investigated by neutron diffraction and X-ray diffraction, where the Si and Al atoms are found to preferentially occupy the $3g$ site of the CaCu$_5$-type structure [10-12]. Substitution in YCo$_5$ of Co by Si or Al induces important effects on the magnetic properties: a decrease in the Curie temperature (T_C) and the saturation magnetization (M_S), as well as a change in the magnetic anisotropy. The dilution of the Co sublattice by substitution of the nonmagnetic Al atom for Co decreases the magnetic moment μ_{Co} from 1.6 μ_B to 1.05 μ_B for YCo$_5$ [28] and YCo$_4$Al, respectively. With the substitution of Si for Co, the Co magnetic moment μ_{Co} of the YCo$_4$Si compound dramatically decreases to 0.75 μ_B. Thus, Si and Al substitution have shown a similar trend for their effect on the magnetic properties, although the Co moment μ_{Co} and transition temperature T_C are reduced more strongly by Si substitution compared to Al substitution.

Here, we aim to study a series of Si-based alloys with Y fixed to unity and introduce Co as substitutional element for Ni to explore the magnetic phase transition, in order to understand the evolution of the properties. First Y has no magnetic moment and this can help to better understand specific magnetic properties and structural transformation, resulting from variations in the ratio of different $3d$ elements. There is also a Si-based compound YCo$_4$Si whose transition temperature is near room temperature. This is one of the key conditions for magnetic heat pump applications. Therefore, the main focus of this study is on the quantitative evaluation of magnetic anisotropy parameters and magnetic phase transitions in YNi$_{4-x}$Co$_x$Si compounds.

6.2 Experimental Details

The YNi$_{4-x}$Co$_x$Si compounds have been prepared by melting high-purity starting elements Y (99.9 %), Ni (99.98 %), Co (99.8 %) and Si (99.9 %) in an arc melting furnace under a purified argon atmosphere. The molten ingots were turned and remelted five times to ensure homogeneity. Then the as-cast ingots were put into a quartz tube with a nozzle at the bottom, melted and ejected through the nozzle onto a cold Cu wheel rotating at a surface speed of 36 m/s. The thickness of the melt spun ribbons was 20-40 μm. To ensure the samples are single-phase, we added 3% of yttrium to compensate for oxides in the starting material. To explore the impact of the heat treatment on the crystal structure, we subjected the YNi$_{4-x}$Co$_x$Si compounds that were sealed in quartz ampoules filled with Ar, to an annealing at 873 K for 24 h, followed by rapid quenching in ice-cold water. The structure, purity and composition of the polycrystalline samples were evaluated using powder X-ray diffraction (XRD), electron microscopy and energy dispersive spectroscopy (EDS). The X-ray data are obtained on a PANalytical X-Pert PRO diffractometer (Cu-K_α radiation, angular range 10°- 90°, angular step 0.02°, 1 s per step). The temperature- and field-dependent magnetization was measured with a superconducting quantum interference device (Quantum Design MPMS-XL) at a ramp rate of 2 K/min using the reciprocating sample option (RSO). The sample mass for the SQUID magnetisation experiments was approximately 1-2 mg. Neutron diffraction (ND) experiments were carried out at the research reactor of the TU Delft [14]. A neutron wavelength of 1.67 Å was selected by the (5 3 3) reflection of a germanium single crystal monochromator. The powder samples with a mass of 5 g were loaded under argon in a 6 mm diameter air-tight vanadium sample can (wall thickness of 100 μm). The data were collected at temperatures of 5, 298 and 350 K. Refinements of the diffraction data were performed using the Rietveld method [15] as implemented in the Fullprof software [16]. Field-oriented samples were prepared by solidifying a mixture of glue and powdered specimen in a magnetic field of 1 T in the ferromagnetic state. Prior to orienting in field, the samples were powdered and then sieved down to a particle size smaller than 30 μm.

6.3 Results and Discussion

### 6.3.1 Crystalline structure

X-ray diffraction analysis confirms that the as-cast YNi$_{4-x}$Co$_x$Si compounds crystallize in the hexagonal CaCu$_5$-type structure (space group *P6/mmm*). Both X-ray diffraction and EDS shows that the YNi$_{4-x}$Co$_x$Si compounds are single phase, as shown in Fig. 6.1a. The unit cell includes the 1*a* site (0,0,0) for Y and the two different crystallographic positions 2*c* (1/3,2/3,0) and 3*g* (1/2,0,1/2) for

Co, Ni and Si, where the Ni and Si atoms predominantly occupy the $3g$ site [10,12]. The $2c$ site lies within the same plane as the $1a$ site, while the $3g$ position is positioned halfway in between the layers containing the $2c$ and $1a$ sites. In $YNi_{4-x}Co_xSi$ compounds the lattice parameters a and c show an opposite trend when Co substitutes Ni, with an increase in unit-cell volume for an increasing Co content x. The c/a ratio decreases for an increasing Co content, as shown in Fig. 6.1(b,c) and Table 6.1.

The CaCu$_5$-type hexagonal phase was not detected in the annealed YNi_4Si compound, which crystallizes in YNi_4Si-type orthorhombic phase (space group $Cmmm$). The unit cell includes the $2c$ site (1/2,0,1/2) for Y, the $2a$ site (0,0,0) for Si and the two different crystallographic positions $4j$ (0,0.15,1/2) and $4e$ (1/4,1/4,0) for Ni. Fig. 6.1d, reveals the orthorhombic distortion of the CaCu$_5$ structure (as-cast sample), in line with the report by Morozkin and coworkers [6]. The $b_O/\sqrt{3}a_H$ ratio can be used to estimate the degree of distortion. The obtained value of $b_O/\sqrt{3}a_H = 1$ corresponds to the transformation of the hexagonal CaCu$_5$-type lattice into the orthorhombic YNi_4Si-type lattice [8]. In the present results, only the YNi_4Si compound shows a clearly different structure between the as-cast and annealed samples with $b_O/\sqrt{3}a_H = 0.97016(8)$ at room temperature (298 K). After Co substitution for Ni, the studied $YNi_{4-x}Co_xSi$ ($x = 1$-2) compounds show a disordered orthorhombic phase, which may be viewed as the disordered variant of the YNi_4Si-type structure (mixed occupancy of the $2c$, $4f$ and $4i$ sites in the orthorhombic lattice) [9]. The $YNiCo_3Si$ and YCo_4Si compounds do not show a disordered phase after annealing. In our results the disordered structure exists until 50% Co substitution ($x = 2$). The temperature for the appearance of the distorted phase strongly depends on the Co concentration. Therefore, in this study we mainly focused on intrinsic physical properties of the as-cast $YNi_{4-x}Co_xSi$ ($x = 0$-4) compounds with the hexagonal structure.
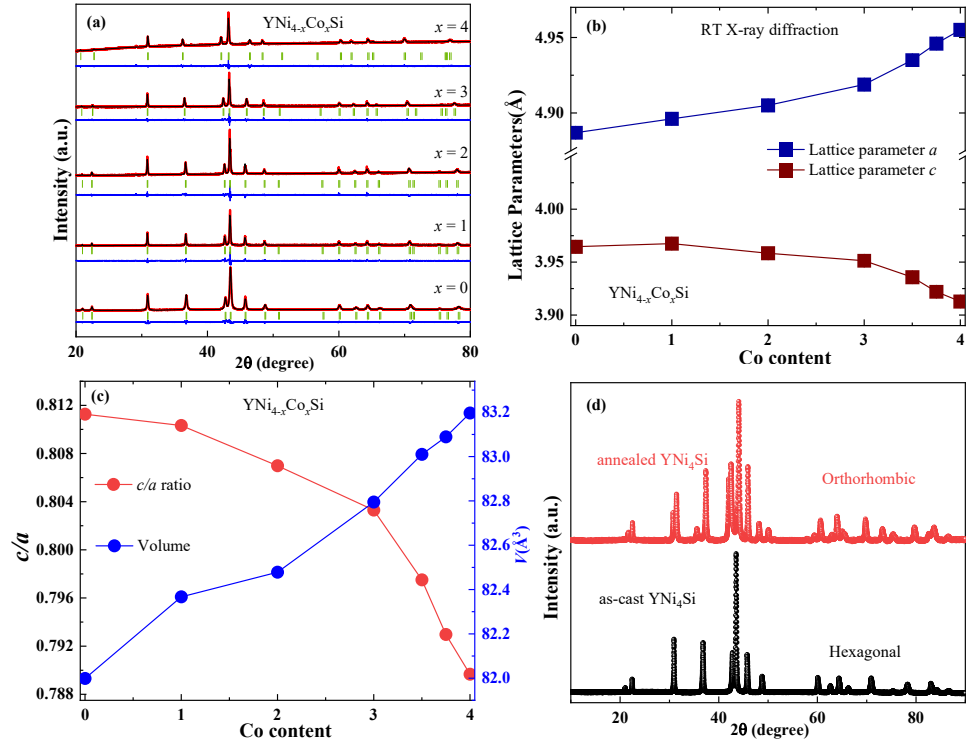
**Fig. 6.1.** (a) X-ray powder diffraction patterns of the $YNi_{4-x}Co_xSi$ alloys at room temperature. (b) Lattice parameters of the hexagonal phase in the $YNi_{4-x}Co_xSi$ compounds as a function of the Co content x. (c) Unit-cell volume and c/a ratio of the $YNi_{4-x}Co_xSi$ compounds as a function of the Co content x. (d) $CaCu_5$-type hexagonal phase of the as-cast YNi_4Si compound and the YNi_4Si-type orthorhombic phase of the YNi_4Si compound after annealing at 873 K.

Table 6.1. Lattice parameters a and c, c/a ratio and unit-cell volume V obtained by room-temperature XRD, saturation magnetization M_s and Curie temperature T_C for the $YNi_{4-x}Co_xSi$ ($2 \leq x \leq 4$) compounds. M_s is obtained from magnetisation measurements at 5 K and T_C from magnetisation measurements in an applied field of 0.01 T.

x	a	c	c/a	V	M_s	T_C	ΔS_{max}
	(Å)	(Å)		(Å^3)	(Am^2 kg^{-1})	(K)	(Jkg^{-1}K^{-1})
0.0	4.88695 (6)	3.96460 (6)	0.81126 (1)	81.998 (2)	-	-	-
1.0	4.89615 (7)	3.96746 (7)	0.81032 (2)	82.367 (2)	-	-	-
2.0	4.90510 (8)	3.95833 (7)	0.80698 (2)	82.478 (3)	4.61	32	0.18
3.0	4.91887 (9)	3.95132 (8)	0.80330 (2)	82.795 (3)	21.51	150	0.29
3.5	4.9350 (13)	3.93569 (11)	0.79750 (3)	83.010 (4)	31.54	250	0.60
3.75	4.9459 (14)	3.92199 (12)	0.79296 (3)	83.089 (4)	36.83	283	0.66
4.0	4.9550 (13)	3.91280 (13)	0.78967 (3)	83.196 (4)	42.67	310	0.75

6.3.2 Magnetic phase transition

From the temperature- and field-dependent magnetization in Fig. 6.2(a,b) we note that a substantial increase in the ferromagnetic transition temperature (T_C) and the saturation magnetization (M_s) is evident upon substituting Co for Ni. For YNi$_{4-x}$Co$_x$Si ($x = 2$-4), a ferromagnetic-to-paramagnetic transition without thermal hysteresis is observed. In the insert of Fig. 6.2a, it can be seen that for the parent YNi$_4$Si compound a paramagnetic behaviour is found in the complete temperature range from 5 to 370 K. For YNi$_4$Si the effective magnetic moment μ_{eff} obtained from the Curie-Weiss law is 0.3 μ_B/f.u. [8, 9]. As shown in the insert of Fig. 6.2b the field-dependent magnetization of YNi$_4$Si shows a magnetization per formula unit (M_{5T}) of 0.01 μ_B/f.u. in a field of 5 T ($1/H \rightarrow 0$ gives $M_\infty \rightarrow 0.02$ μ_B/f.u.). These observations suggest a negligible Ni magnetic moment in YNi$_4$Si compounds. The nearly filled Ni ($3d$) band implies that the Ni magnetic moment is negligible [17, 18]. For the YNi$_3$CoSi compound the field-dependent magnetization measurements at 5 K show an unusual ferrimagnetic behaviour without a saturation in fields up to 5 T with $M_{5T} = 0.03$ μ_B/f.u. ($1/H \rightarrow 0$ gives $M_\infty \rightarrow 0.04$ μ_B/f.u.). This indicates that the magnetic moments are enhanced with partly antiferromagnetic (or more complex) spin orientations. A enlargement of the weak magnetization curve for YNi$_3$CoSi is shown in the inset of Fig. 6.2b.
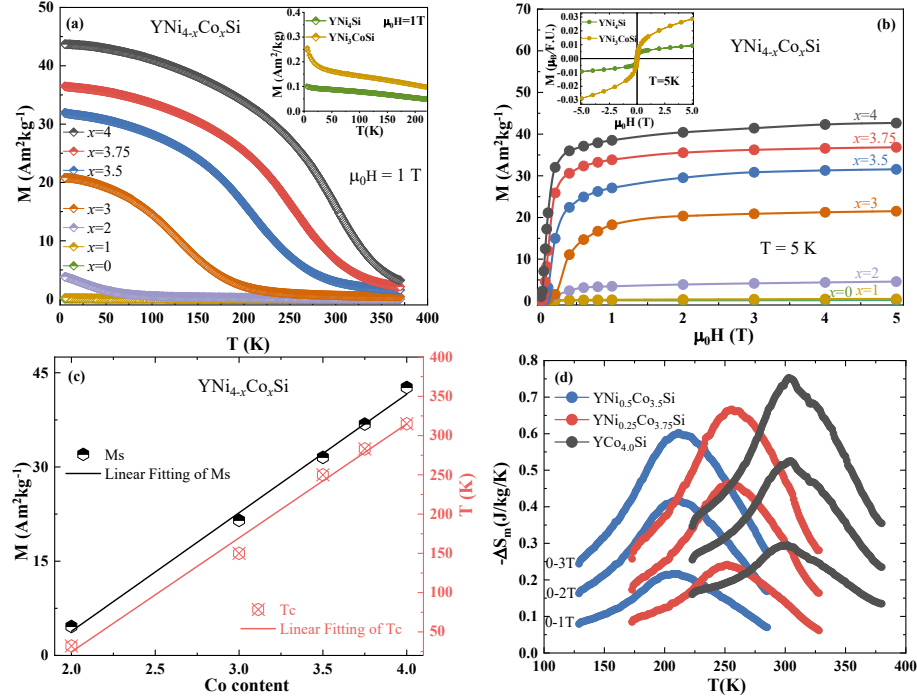

Fig. 6.2. (a) Magnetization as a function of temperature in an applied field of 1 T and (b) magnetization as a function of magnetic field at 5 K of YNi$_{4-x}$Co$_x$Si ($x = 0$ - 4) (inset

shows an enlargement of the weak magnetisation curves for $x = 0$ - 1). (c) Values of T_C and M_s for $YNi_{4-x}Co_xSi$ ($x = 0$ - 4) as a function of the Co content. (d) Isothermal entropy change $-\Delta S$ obtained from the magnetisation $M(T)$ upon heating in a field change of 1, 2 and 3 T.

Fig. 6.2c shows T_C and M_s as a function of the Co content, indicating that the transition temperature T_C increases from 32 to 310 K in the $YNi_{4-x}Co_xSi$ ($x = 2$- 4) compounds and can continuously be varied near room temperature by adjusting the Ni/Co ratio. Since the temperature dependence of the magnetization exhibits a relatively broad transition, the transition temperature defined as the maximum in the first derivative $|dM/dT|$ is not necessarily accurate. However, the mean field models are an alternative option for predicting transition temperature. Therefore, we used the equation $M(T)^2 = A^2(T_C - T)$ to estimate T_C (Table 6.1). For a Co concentration above 50% ($x > 2$), a strong increase in saturation magnetization is observed from 5 ($x = 2$) to 43 ($x = 4$) Am^2 kg^{-1}. The isothermal entropy change is calculated by applying the Maxwell relation $\Delta S(T)_{\Delta H} = \int_{H_i}^{H_f} \mu_0 \left(\frac{\partial M(T,H)}{\partial T} \right)_H dH$ [20, 21] to the $M(T)$ data at different fields. The magnetic or indirect calorimetric determinations of the entropy change suffer from uncertainties, typically of the order of 10% [22]. As indicated in Fig. 6.2d, the $YNi_{0.5}Co_{3.5}Si$, $YNi_{0.25}Co_{3.75}Si$ and YCo_4Si compounds ($x = 3.5, 3.75, 4.0$) show a maximum $|\Delta S_{max}|$ of 0.60, 0.66 and 0.75 J kg^{-1} K^{-1} for a field change of 3 T, respectively. While the values for the isothermal entropy change are limited, the magnetocaloric effect is spread out over a wide temperature range due to the broadening of the $M(T)$ curve in higher magnetic fields. Typically, this behaviour is observed in magnetocaloric materials with a second-order magnetic phase transition as a result of the temperature- and field-dependence of the magnetocaloric effect. To get further insight into the order of the ferromagnetic transition in YCo_4Si, we used a method recently proposed by Franco and coworkers [23,24]. Assuming that the field-dependence of the isothermal isothermal entropy change follows a power law of the type $|\Delta S| \propto H^n$. The field exponent $n = \frac{d \ln(|\Delta S|)}{d \ln(H)}$ generally shows a significant variation near the transition temperature [24, 25]. In particular, $n > 2$ was proposed for materials characterized by a first-order magnetic phase transitions (FOPT). Fig. 6.3 shows the local field dependence of the isothermal entropy change (ΔS) for the YCo_4Si compound. It is clearly seen that $n < 2$ near T_C for $\Delta\mu_0 H = 2$ and 3 T, reflecting a second-order magnetic phase transition (SOPT) [24]. Similar results were obtained for the other Ni/Co compounds ($x = 3.5, 3.75, 4$). In a conventional paramagnet ($T > T_C$) the value of n tends to 2. The analysis of the field dependence of ΔS thus demonstrates the SOPT character of the ferromagnetic transition. This is

consistent with the absence of thermal hysteresis in the $M(T)$ curves for these materials.
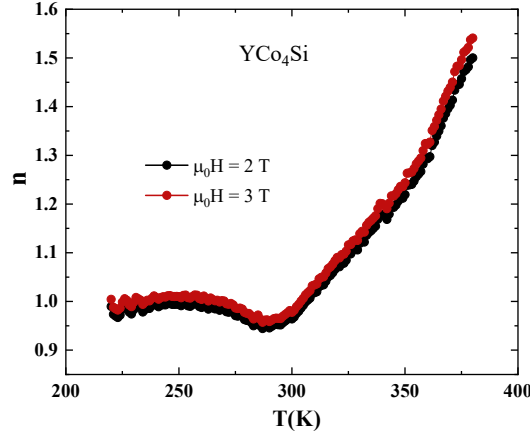
Fig. 6.3. Field exponent n of the isothermal entropy change in a field change of 2 and 3 T.

To study the characteristics of the magneto-elastic coupling, high-resolution XRD measurements are performed as function of temperature. Fig. 6.4a shows that the (111) reflection for the YCo_4Si compound shifts to a smaller angle at higher temperature as a result of the magnetic transition. This behaviour is linked to the magneto-elastic coupling of the magnetic order with the thermal expansion of the lattice. Fig. 6.4b shows the unit-cell volume as a function of temperature in the temperature range from 150 to 400 K. Due to the magnetic phase transition the linear continuous change in volume shows a kink at the ferromagnetic transition temperature (310 K). The volume difference ΔV between the ferromagnetic state and the linear extrapolation of the paramagnetic state can be regarded as the contribution from the magneto-elastic coupling. The transition temperature determined from the temperature-dependent XRD is in agreement with the transition found in the magnetization. The value is in agreement with the transition temperature of 320(5) K reported by Isnard and coworkers for the YCo_4Si compound [10] and is lower than the value of $T_C = 350$ K reported by Thang and coworkers [26].
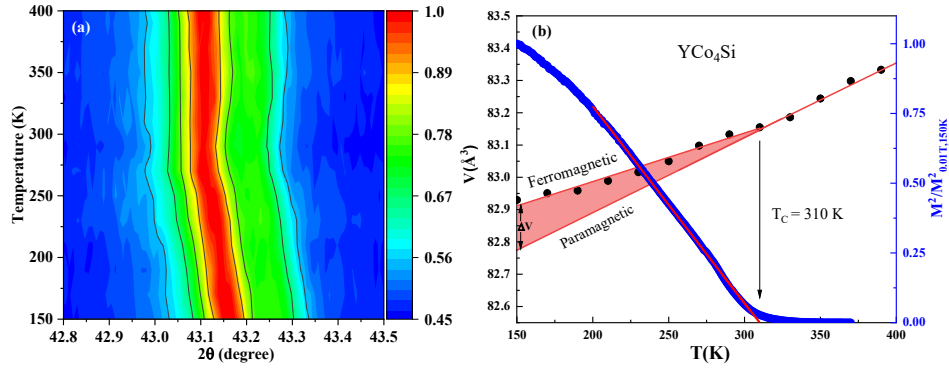
Fig. 6.4. (a) (111) reflection of YCo$_4$Si as a function of temperature. (b) Temperature dependence of the unit-cell volume V and the normalized M^2-T curve in a magnetic field of 0.01T for the YCo$_4$Si compound.

6.3.3 Magneto-crystalline anisotropy

To highlight the significant magneto-crystalline anisotropy in the quaternary YNi$_{4-x}$Co$_x$Si compounds, we selected three representative polycrystal samples ($x = 3.5$, 3.75 and 4.0) with a T_C near room temperature and hand crushed them into particles with a size smaller than 30 μm. During the field orientation process the powder was mixed with glue and placed on a plate in a magnetic field of 1 T orientated perpendicular to the plate.

XRD measurements were performed on the surface of the plate. The XRD measurements show a large difference between the results for field-oriented powders and free powders. Due to the magnetic orientation, one observes in Fig. 6.5a that reflections with a or b axis components, like (1 1 0) and (2 0 0), disappear almost completely. Simultaneously, reflections with a pure c axis component, like (0 0 1) and (0 0 2), are strongly enhanced. This indicates that in polycrystalline YNi$_{4-x}$Co$_x$Si ($x = $ 3.5-4) compounds the c-axis is the easy magnetization direction (EMD), and the a-b plane is a hard magnetization direction (HMD). This result is in agreement with previous studies on YCo$_5$, YCo$_4$Al, YCo$_{4.5}$Ge$_{0.5}$ and YCo$_4$B [11, 27-29]. The YCo$_4$B compound however shows a spin reorientation at low temperature (150 K) with the EMD in the a-b plane below the spin reorientation temperature [19, 27].
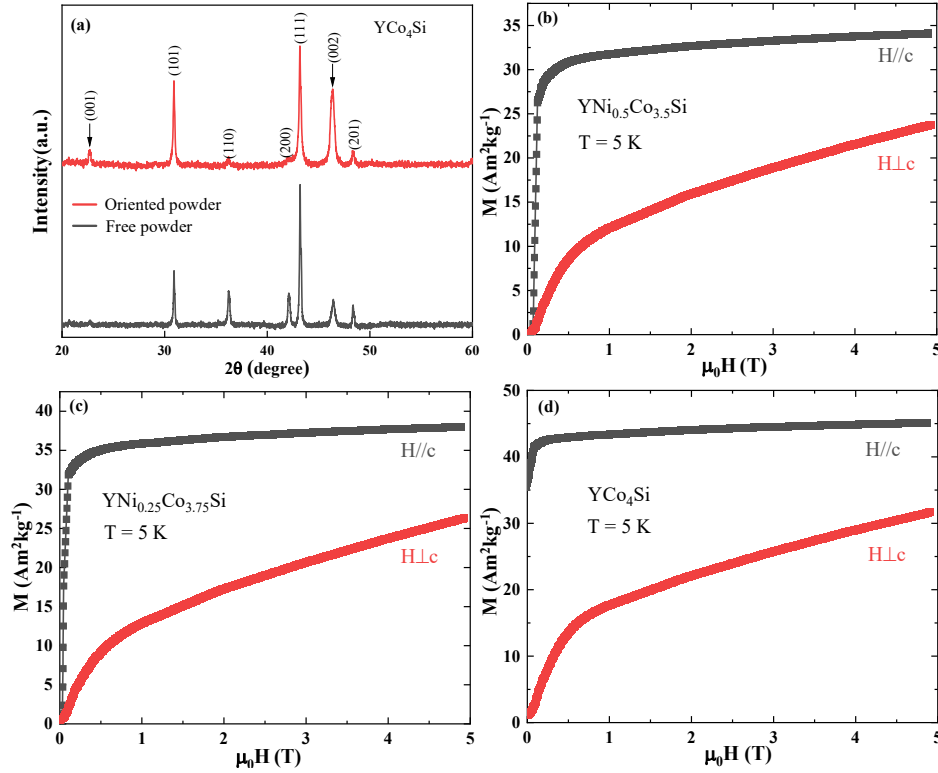
Fig. 6.5. (a) comparison between field-oriented and free powder XRD indicating large changes in the peak intensities by the alignment of the easy axis along the applied field. (b - d) Magnetization as a function of field for the YNi$_{4-x}$Co$_x$Si (x = 3.5, 3.75 and 4.0) compounds measured parallel and perpendicular to the c axis of the hexagonal lattice at 5 K.

Isothermal magnetization curves were systematically recorded in all quadrants and reveal magnetic hysteresis loops with a significant coercive field at low temperature. In Fig. 6.5(b-d) only the first quadrant measurements were performed at 5 K along c axis and in the a-b plane for each compound. The $M(H)$ curves measured at low temperature (5 K) clearly indicate a particularly large magnetic anisotropy, as the anisotropy field ($\mu_0 H_{an}$) is significantly higher than our applied field of 5 T. A linear extrapolation suggests that $\mu_0 H_{an}$ is of the order of 10 T, which is half of the value $\mu_0 H_{an} = 20$ T obtained for YCo$_{4.5}$Ge$_{0.5}$ [29]. This anisotropy slowly decreases with increasing temperature until it approaches the Curie temperature where it decreases more rapidly and finally vanishes. As shown in Fig. 6.6 the coercive field of YCo$_4$Si significantly reduces from 160 kA/m at 5 K to 0.55 kA/m at 300 K. The RM_5-type materials exhibit relatively large values for the saturation magnetic polarization $J_s = \mu_0 M_s$, the maximum energy product $(BH)_{max}$, and the uniaxial magnetic anisotropy, with the hexagonal c axis serving as the easy magnetic direction [6, 9]. These properties are of utmost importance

87

for the development of permanent magnets. The insert in Fig. 6.6 shows the $B(H)$ hysteresis measurements at 5 K (including the virgin magnetization curve). It can be seen $(BH)_{max}$ of the present YCo_4Si compound is 19 kJ m^{-3} at 5 K (it is 1.0 kJ m^{-3} at 200 K). The saturation magnetic polarization J_s is listed in Table 6.2. Polarized neutron diffraction experiments [28] have demonstrated that the high anisotropy in YCo_5 is associated with an important orbital contribution on the Co $2c$ site. As reported by Pareti and coworkers [30] the $CaCu_5$ -type structure contains two different Co sites: $2c$ and $3g$. These two Co sites give opposite contributions to the magneto-crystalline anisotropy: axial for $2c$ and planar for $3g$ [11, 28, 30, 33]. The overall axial anisotropy of YCo_5 is the sum of the two contributions. Therefore, it deserves a study dedicated to other $3d$ metals substitutions (often considered are Co, Ni and Fe).

Table 6.2. Comparison of the magnetocrystalline anisotropy constants K_1 and K_2, saturation specific magnetization (M_s), saturation magnetic polarization ($J_s = \mu_0 M_s$) and coercive field H_C for the $YNi_{4-x}Co_xSi$ ($x = 3.5, 3.75$ and 4.0) compounds.

Material	K_1 (5 K) (MJ m^{-3})	K_2 (5 K) (MJ m^{-3})	M_s (5 K) (μ_B/f.u.)	J_s (5 K) (T)	H_C (5 K) (kA m^{-1})
YCo_4Si	0.18(1)	1.05(2)	2.69(1)	0.41(2)	160(1)
$YCo_{3.75}Ni_{0.25}Si$	0.34(2)	0.98(3)	2.32(2)	0.37(2)	143(3)
$YCo_{3.5}Ni_{0.5}Si$	0.38(1)	0.89(3)	1.99(2)	0.36(1)	135(1)
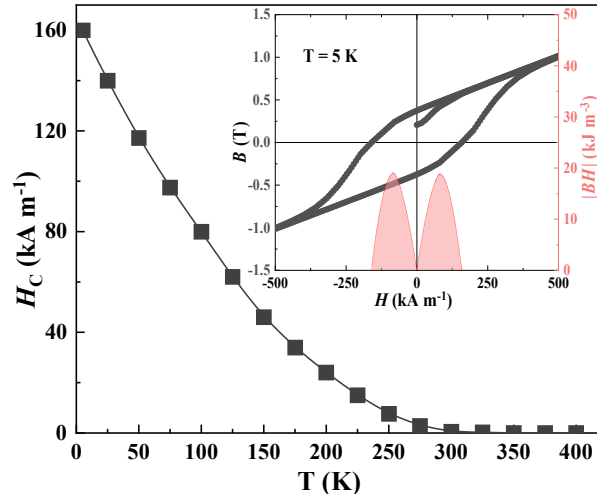
Fig. 6.6. Coercive field H_C versus temperature for field-oriented YCo_4Si powder. The insets shows the $B(H)$ hysteresis measurements at 5 K.

In order to calculate the anisotropy constant, first the effect of the demagnetizing field was included assuming an internal field $H_{in} = H_{ap} - NM$, where H_{ap} is the applied magnetic field, M the magnetization and N the sample-shape dependent demagnetizing factor. For an uniaxial system the magnetic anisotropy constants are K_1 and K_2. The magneto-crystalline anisotropy energy E_A in a crystal can be expressed as $E_A \approx K_1 \sin^2\theta + K_2 \sin^4\theta$, where θ is the angle between the magnetization vector and the axial symmetry direction of the crystal (in this case c axis for the hexagonal lattice). The K_1 and K_2 magnetocrystalline anisotropy constants can be estimated from the magnetization curves recorded parallel and perpendicular to the c axis in the temperature range from 5 to 350 K, using the Sucksmith and Thompson method [31]. In this method the following relation is considered: $\frac{2K_1}{J_S^2} + \frac{4K_2}{J_S^4}J^2 = \frac{H}{J}$, where $J = \mu_0 M$ is the magnetic polarization and H the internal magnetic field. Fig. 6.7 presents the obtained temperature evolution of K_1 and K_2 for each compound. The values at low temperature (5 K) are listed in Table 6.2. The K_1 and K_2 magnetic anisotropy values are both positive, as is expected for materials with a c easy magnetization axis (an easy axis is predicted under the condition that $K_1 > 0$ and $K_2 > -K_1$). For all three alloys we find $K_2 > K_1 > 0$. For YCo$_4$Si we find $K_1 \approx 0.18$ MJ m^{-3} and $K_2 \approx 1.05$ MJ m^{-3} at 5 K. The K_2/K_1 ratio decreases for increasing Ni substitutions. As expected, the magneto-crystalline anisotropy constants K_1 and K_2 decrease for increasing temperature and vanish at T_C.
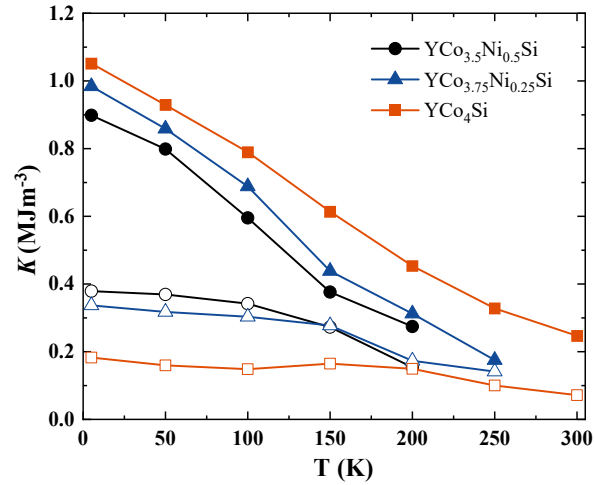
Fig. 6.7. Magneto-crystalline anisotropy constants K_1 (open symbols) and K_2 (full symbols) determined as a function of the temperature by the Sucksmith and Thompson method for YNi$_{4-x}$Co$_x$Si ($x = 3.5$, 3.75 and 4.0).
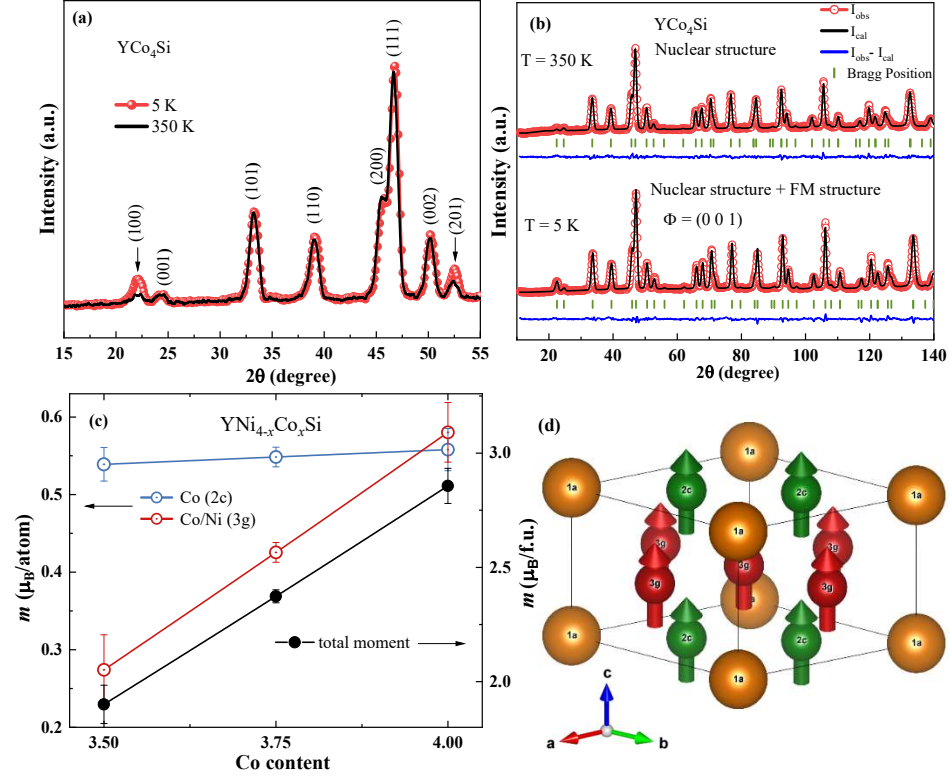
6.3.4 Magnetic structure

Powder neutron diffraction (ND) is a powerful method to determine the magnitude and direction of magnetic moments. A precise structure determination of the Ni location in the $CaCu_5$-type structure was completed by powder ND investigations. For YCo_4Si the $1a$ site is occupied by Y and the $2c$ and $3g$ sites are occupied by Co and Si. It is well known that in the RCo_5 structure the Si atoms preferentially occupy the $3g$ site [10, 32, 33]. Fig. 6.8a shows a comparison of the neutron diffraction pattern of YCo_4Si at 5 and 350 K. No new peaks appear in the ferromagnetic (FM) state in comparison with the paramagnetic (PM) state of YCo_4Si. Therefore, the propagation vector of the magnetic structure corresponds to $\mathbf{k} = (0,0,0)$. From the enhancement of the peak intensity of the (100) and (201) reflections and the absence of an enhancement for the (002) reflection it can be deduced that the spins in the FM state are aligned along the c-axis. Thus, the irreducible representation used for the magnetic basic vector is $\Phi = (0\ 0\ 1)$. The refinement of the neutron patterns shown in Fig. 6.8b confirm the hexagonal $CaCu_5$-type structure (space group $P6/mmm$) for all compounds. This is in line with the XRD results. For the YCo_4Si compound magnetic moments of $0.56\mu_B$ on the $2c$ site and $0.58\mu_B$ on the $3g$ site have been found. These values are almost equal, as was found for the YCo_4Ga compound by Thang and coworkers [11]. The sum of the Co magnetic moments ($2.86(7)$ μ_B/f.u.) is slightly larger than the value obtained by bulk magnetization (2.69 μ_B/f.u.) in the present results. The total magnetic moment obtained from neutron diffraction $2.86(7)$ μ_B/f.u. is comparable with the value of 3.0 μ_B/f.u. reported by Isnard and coworkers [10] and obtained by SPR-KKR calculations reported by Benea and coworkers [34].

After a partial Ni substitution for Co, the Ni atoms preferentially occupy the $3g$ site. As a result, the magnitude of the magnetic moments on the $3g$ site decreases more rapidly compared to the $2c$ site. For instance, as shown in Fig. 6.8c and Table 6.3 the magnitude of the Co-$3g$ magnetic moment ($0.27\mu_B$) is only about half of that obtained on the Co-$2c$ site ($0.54\mu_B$) in the $YNi_{0.5}Co_{3.5}Si$ compound. However, we observe a rather constant (within $0.01\mu_B$) contribution of the Co-$2c$ magnetic moments at low temperature (5 K) for the three different compounds. Fig. 6.8d shows a representative magnetic unit cell for $YNi_{4-x}Co_xSi$ compounds. In $YNi_{4-x}Co_xSi$ compounds the nuclear unit cell has the same size as the magnetic unit cell and the magnetic moments are aligned with the c axis. This alignment serves as a dual confirmation that the $YNi_{4-x}Co_xSi$ compounds are uniaxial systems with the c axis as easy magnetization axis. Furthermore, the replacement of Ni leads to a marginally reduced atomic separation between the

Co atoms at the d_{2c-2c} and d_{3g-3g} spacings. The specific atomic distances between various atomic positions can be found in Table 6.3.

Fig. 6.8. Powder neutron diffraction pattern of $YNi_{4-x}Co_xSi$ obtained at 5 and 350 K. (a) Comparison of the YCo_4Si compound in the ferromagnetic state (5 K) and in the paramagnetic state (350 K). (b) Refinements of the nuclear and magnetic structure. (c) Magnetic moment of the $YNi_{4-x}Co_xSi$ (x = 3.5, 3.75 and 4) compounds obtained by neutron diffraction at 5 K. (d) Magnetic structure of the YCo_4Si compound in the ferromagnetic state, the moments are aligned along the c axis.

Table 6.3. Results of the neutron diffraction data analysis for $YNi_{4-x}Co_xSi$ ($x = 3.5$, 3.75 and 4.0) at 5 K.

Parameters	YCo_4Si (5 K)	$YCo_{3.75}Ni_{0.25}Si$ (5 K)	$YCo_{3.5}Ni_{0.5}Si$ (5 K)
a (Å)	4.93395 (5)	4.92382 (4)	4.91219 (3)
c (Å)	3.90145 (7)	3.91145 (6)	3.92268 (5)
V (Å^3)	82.252 (2)	82.125 (2)	81.972 (1)
easy magnetization axis	c axis	c axis	c axis
μ_{Co-2c} (μ_B)	0.5580 (272)	0.54849 (127)	0.539 (216)
μ_{Co-3g} (μ_B)	0.58028 (384)	0.42549 (127)	0.27411 (451)
M (μ_B/f.u.)	2.85684 (768)	2.37345 (284)	1.90033 (838)
$2c$ site (%Co)	100 (2)	100 (2)	100 (2)
$3g$ site (%Co)	63 (3)	56 (3)	50 (3)
d_{2c-2c} (Å)	2.84863(3)	2.84278(2)	2.83607(2)
d_{3g-3g} (Å)	2.46697(3)	2.46191(2)	2.45610(2)
d_{1a-1a} (Å)	3.90145(7)	3.91145(6)	3.92268(5)
d_{2c-3g} (Å)	2.41536(2)	2.41768(3)	2.42025(2)
d_{1a-2c} (Å)	2.84863(3)	2.84278(2)	2.83607(2)
d_{1a-3g} (Å)	3.14504(2)	3.14418(2)	3.14313(2)
R_{exp}, R_{wp}, R_p (%)	3.14, 8.80, 10.7	4.06, 9.27, 10.7	4.03, 8.33, 9.36

6.4 Conclusions

$YNi_{4-x}Co_xSi$ ($x = 0$-4) compounds were synthesised and characterized to investigate their magnetic properties. By analysing the field dependence of the magnetocaloric effect, it was found that the ferromagnetic-to-paramagnetic transition is a second-order magnetic phase transition, which is compatible with the absence of thermal hysteresis related to the phase transition. X-ray diffraction experiments and magnetic measurements on field-oriented polycrystalline materials confirm the relatively strong magneto-crystalline anisotropy obtained at the Co rich side ($x = 3.5$, 3.75 and 4.0), with the c axis as the easy axis for the magnetisation direction and the a-b plane as the hard magnetic direction. The magnetocrystalline anisotropy constants are determined over a broad temperature range and show $K_2 > K_1 > 0$, in line with the easy direction for the magnetisation. Powder neutron diffraction experiments demonstrate the preference of Ni atoms for the $3g$ site. The magnetic properties are dramatically affected by the Ni/Co ratio. A dramatic decrease in the mean Co magnetic moment at the $3g$ site, the saturation magnetization and the Curie temperature was found for increasing Ni

concentrations. The transition temperature T_C can be adjusted continuously over a broad temperature range for different Ni/Co ratios. This fulfils one important application requirement for the magnetocaloric materials. In this study, the evolution of the crystalline and magnetic structure, as well as changes in magnetic properties, are identified. They reveal large changes in the bulk physical properties, such as the magnetization, transport and thermal properties, which form the basis for their applications.

References

[1] E. Brück, O. Tegus, D.T.C. Thanh, K.H.J. Buschow, J. Magn. Magn. Mater. 310 (2007) 2793-2799.

[2] J. Cui, M. Kramer, L. Zhou, F. Liu, A. Gabay, G. Hadjipanayis, B. Balasubramanian, D. Sellmyer, Acta Mater. 158 (2018) 118-137.

[3] J.M.D. Coey, Scr. Mater. 67 (2012) 524-529.

[4] O. Gutfleisch, M.A. Willard, C.H. Chen, E. Brück, S.G. Sankar, J.P. Liu, Adv. Mater. 23 (2011) 821-842.

[5] A.K. Pathak, M. Khan, K.A. Gschneidner, R.W. McCallum, L. Zhou, K. Sun, K.W. Dennis, C. Zhou, F.E. Pinkerton, M.J. Kramer, V.K. Pecharsky, Adv. Mater. 27 (2015) 2663-2667.

[6] A.V. Morozkin, A.V. Knotko, V.O. Yapaskurt, Fang Yuan, Y. Mozharivskyj, R. Nirmala, J. Solid State Chem. 208 (2013) 9-13.

[7] S.N. Klyamkin, V.N. Verbetsky, A.A. Karih, J. Alloys Compd. 231 (1995) 479-482.

[8] A.V. Morozkin, Fang Yuan, Y. Mozharivskyj, O. Isnard, J. Magn. Magn. Mater. 368 (2014) 121-125.

[9] A.V. Morozkina, A.V. Garsheva, V.O. Yapaskurtc , J. Yao, R. Nirmala, S. Quezado, S.K. Malik, J. Solid State Chem. 265 (2018) 18-28.

[10] O. Isnard, Z. Arnold, N. Coroian, J. Kamarad, J. Magn. Magn. Mater. 316 (2007) 325-327.

[11] O. Moze, L. Pareti, A. Paoluzi, K.H.J. Buschow, Phys. Rev. B 53 (1996) 11550-11556.

[12] C.V. Thang, T.Q. Vinh, N.P. Thuy, J.J.M. Franse, Physica B 246-247 (1998) 505-508.

[13] L. Pareti, M. Solzi, G. Marusi, J. Appl. Phys. 72 (1992) 3009.

[14] L. van Eijck, L.D. Cussen, G.J. Sykora, E.M. Schooneveld, N.J. Rhodes, A.A. van Well, C. Pappas, J. Appl. Cryst. 49 (2016) 1398-1401.

[15] H.M. Rietveld, J. Appl. Cryst. 2 (1969) 65-71.

[16] J. Rodriguez-Carvajal, Physica B 192 (1993) 55-69.

[17] S. Legvold, in: E.P. Wohlfarth (Ed.), Ferromagnetic Materials, North-Holland Publishing Company, Amsterdam, (1980) pp. 183-295.

[18] M. Pugaczowa-Michalska, M. Falkowski, A. Kowalczyk, Acta Physica Polonica A 113 (2008) 323-326.

[19] C. Chacon, O. Isnard, J. Appl. Phys. 89 (2001) 71-75.

[20] V.K. Pecharsky, K.A. Gschneidner Jr., Phys. Rev. Lett. 78 (1997) 4494-4497.

[21] K.A. Gschneidner Jr., V.K. Pecharsky, A.O. Tsokol, Rep. Prog. Phys. 68 (2005) 1479-1539.

[22] V.K. Pecharsky, K.A. Gschneidner Jr., J. Appl. Phys. 86 (1999) 565-575.

[23] V. Franco, J.S. Blazquez, A. Conde, Appl. Phys. Lett. 89 (2006) 222512.

[24] J.Y. Law, V. Franco, L.M. Moreno-Ramírez, A. Conde, D.Y. Karpenkov, I. Radulov, K.P. Skokov, O. Gutfleish, Nat. Commun. 9 (2018) 2680.

[25] N.H. van Dijk, J. Magn. Magn. Mater. 529 (2021) 167871.

[26] C.V. Thang , L.H. Nam, N.P. Duong, N.P. Thuy, E. Brück, J. Magn. Magn. Mater. 196-197 (1999) 765-767.

[27] R. J. Caraballo Vivas, D. L. Rocco, T. Costa Soares, L. Caldeira, A. A. Coelho, M. S. Reis, J. Appl. Phys. 116 (2014) 063907.

[28] C. Zlotea, O. Isnard, J. Magn. Magn. Mater. 242-245 (2002) 832-835.

[29] C.V. Colina, O. Isnarda, M. Guillot, J. Alloys Compd. 505 (2010) 11-16.

[30] L. Pareti, M. Solzi, G. Marusi, J. Appl. Phys. 72 (1992) 3009-3012.

[31] W. Sucksmith, F.R.S. Thompson, J.E. Thompson, Proc. Royal Soc. A 225 (1954) 362.

[32] N. Coroian, V. Klosek, O. Isnard, J. Alloys Compd. 427 (2007) 5-10.

[33] R.L. Streever, Phys. Rev. B. 19 (1979) 2704-2711.

[34] D. Benea, O. Isnard, N. Coroian, V. Pop, J. Magn. Magn. Mater. 322 (2010) 1052-1055.

Chapter 7

Complex spin structure and magnetic phase transition of Mn$_{3-x}$Fe$_x$Sn alloys

Abstract

The hexagonal Mn$_{3-x}$Fe$_x$Sn compounds possess several desirable properties that make them suitable novel magnetocaloric materials (MCMs), including a ferromagnetic-to-paramagnetic transition near room temperature and soft magnetic behaviour. In this study, we used the melt spinning technique to explore the Mn-Fe-Sn ternary system. By combining magnetisation measurements, Mössbauer spectroscopy, neutron diffraction, oriented powder X-ray diffraction and density functional theory (DFT) calculation, the magnetocaloric effect (MCE), spin structures and the intrinsic magnetic properties of polycrystalline Mn$_{3-x}$Fe$_x$Sn (x = 0.8-1.4) compounds are determined. The ferromagnetic-to-paramagnetic transition temperature T_C ranges from 253 K (x = 0.8) to 394 K (x = 1.4). At low temperature a spin reorientation at T_S is observed, where below T_S a coexistence of ferromagnetic (FM) order with spins along the c axis and antiferromagnetic (AFM) order with spins within a-b plane occurs for x = 0.8 and 1.0. However, for compounds with x = 1.2 and 1.4, FM order with spins along the c axis has been found below T_S. Above T_S, the spin structure corresponds to FM order with spins aligned within the a-b plane. The magnetic moments of Mn and Fe were evaluated using Density Functional Theory (DFT), demonstrating a good agreement with the neutron diffraction results.

7.1 Introduction

The investigation and utilization of Heusler alloys have attracted increasing attention due to their fascinating physical properties and potential applications as giant magnetocaloric effect (MCE) materials [1–3], ferromagnetic (FM) shape-memory alloys [4–6], topological insulators [7] and half-metals [8,9]. In the X_2YZ-compounds, where X and Y are $3d$ transition metals and rare-earth metals, Z is a main group element (like Si, Al, Ge, Ga, Sn and Sb). They manifest diverse crystalline symmetries, such as cubic, tetragonal and hexagonal [10,11]. Since the rare earth crisis of 2011, persistent supply chain vulnerabilities and price fluctuations of rare-earth metals, there has been a growing research interest in the development of rare-earth-free materials for various applications [12,13]. Hence, particularly Sn-based Mn-Fe-Sn alloys offer markedly superior properties compared to commercially available alternatives, with the added benefits of good availability and sustainability [14]. Properties like a sizeable magneto-crystalline anisotropy, a high spin polarization and high transition temperatures qualify them as good candidates for magnetic materials with high performance for spintronics [15–17]. Subsequently, density functional theory (DFT) calculations predicted that the Heusler alloy $(Mn,Fe)_3Sn$ is a promising MCE material for magnetic heat pump and thermomagnetic motor applications [18–24]. Due to their relatively high magnetic moments and transition temperatures they can be adjusted continuously by their Mn/Fe ratio [14]. According to the binary Mn-Sn and Fe-Sn phase diagrams the Mn_3Sn and Fe_3Sn compounds both crystallize in the hexagonal Mg_3Cd-type structure [25–28]. However, the processing route for these two compounds requires a different heat treatment. The Mg_3Cd-type crystal structure with $P6_3/mmc$ symmetry (space group 194) is composed of two layers, each containing three magnetic (Mn, Fe) atoms at the $6h$ site and one non-magnetic Sn atom at the $2d$ site of the hexagonal unit cell [29,30]. The magnetic atoms are arranged in a triangle in each layer [29].

Previous studies on the Sn-based Mn-Fe-Sn system have identified several different applications based on their different intrinsic properties. Neutron diffraction studies of Mn_3Sn [25,31–43] have revealed an inverse antiferromagnetic (AFM) triangular spin structure below $T_N \approx 420$ K [30,35]. It is proposed that these properties enable promising applications in data storage high-density memory integration, and ultrafast data processing [15] due to the insensitivity of AFM spin structures to perturbations, the absence of stray fields, and fast spin dynamics [44,45]. However, a single crystal of Mn_3Sn measured in an applied magnetic field oriented along $\mathbf{H} \parallel (0\ 1\ 0)$, revealed the presence of weak ferromagnetism with hysteresis at $T = 300$ K [30]. Polarized neutron diffraction studies elucidated that the weak ferromagnetism observed in Mn_3Sn

originates from the triangular AFM structure itself. This phenomenon is attributed to the change in orientation induced by the interaction between the magnetic field and the ferromagnetic moment, which varies depending on the orientation of the triangular AFM structure [35,42,46]. On the other side the nature of FM ordering in the Fe_3Sn compound [27,47–49] has been examined for permanent magnetic applications, revealing a high Curie temperature ($T_C \approx 725$ K), a basal plane magnetic anisotropy constant of 1.8 MJ m^{-3} and a sizeable magnetization $M_s =$ 120 Am^2 kg^{-1} at room temperature [27,28,49–52]. While the magneto-crystalline anisotropy corresponds to easy plane, its considerable absolute value has led to investigations into potential modifications aimed at shifting the anisotropy from easy plane to easy axis. Subsequently, theoretical calculations predicted that tuning the anisotropy from easy plane to easy axis is feasible by replacing Sn with Sb [49,53]. For the above compounds, both experimental studies and DFT calculations were employed to evaluate the magnitude of the magnetic moments on the *6h* site. DFT calculations yielded a magnetic moment of about 3.0 μ_B/Mn for Mn_3Sn [34,35,43,54] and 2.4 μ_B/Fe for Fe_3Sn. However, previous experimental results for the Mn_3Sn compound exhibited slightly lower magnetic moments, ranging from 2.1 to 2.75 μ_B/Mn [33,55,56]. Later research by Brown et al. and Cable et al. presented experimental values closer to the theoretical prediction of about 3.0 μ_B/Mn for Mn_3Sn [35,37]. For Fe_3Sn, the calculated saturation magnetization of 2.4 μ_B/Fe is slightly higher than the experimental value of 2.2 μ_B/Fe at 10 K [27,49,53]. This difference is attributed to the 4*s* electrons that in metallic iron are negatively polarized by about 0.2 μ_B per atom, with respect to the 3*d* electrons. Therefore, experimental results suggest that the atomic moment of iron metal, 2.2 μ_B/Fe would be composed of about 2.4 μ_B/Fe from the 3*d* electrons and about -0.2μ_B/Fe from the 4*s* electrons [57].

The characteristics of the aforementioned compounds are not suitable for applications in magnetic heat pumps or thermomagnetic motors, as they require a significant MCE centred around a Curie temperature near room temperature. Hence, a transition temperature (T_C) that is tuneable near room temperature is required for magnetocaloric materials (MCM) in magnetic heat pump applications. This is achievable by switching from binary Mn-Sn and Fe-Sn to ternary Mn-Fe-Sn alloys by partially replacing Mn by Fe [14]. When in Mn_3Sn 1/3 of the Mn is replaced by Fe, then the transition temperature of Mn_2FeSn is shifted to a value near room temperature. The magnetic moments that were originally lying on a Kagome lattice for Mn_3Sn will be broken in Mn_2FeSn by a rearrangement of the spin structure. The rearrangement of the magnetic moments has the potential to generate new spin configurations [54]. The ferromagnetic interaction in the Mn_2FeSn compound is enhanced and as a result the magnetic structure has changed [58,59]. Hence, the ferromagnetic-to-paramagnetic

transition in $Mn_{3-x}Fe_xSn$ alloys holds the potential to generate promising MCEs. The spin configuration of Mn_2FeSn and the complex magnetic structure evolution with temperature has not yet been resolved. Therefore, the influence of the Mn/Fe ratio on the magnetic properties of $Mn_{3-x}Fe_xSn$ alloys constitutes the primary focus of this study. This article combines magnetisation measurements, X-ray diffraction, Mössbauer spectroscopy, neutron powder diffraction and DFT calculations to investigate the MCE effect, the structural and magnetic properties of $Mn_{3-x}Fe_xSn$ ($x = 0.8$-1.4) alloys.

7.2 Experimental and Calculation Methods

High-quality polycrystalline $Mn_{3-x}Fe_xSn$ alloys with x ranging between 0.8 and 1.4 were prepared by the traditional arc-melting method in a high-purity argon atmosphere. Elemental starting materials with a purity of 99.9% for Mn, Fe and Sn were weighted in terms of the stoichiometric amount. 2 wt.% excess Mn was added to compensate the weight loss during the melting. Homogeneity for the sample of 5 g was ensured by turning and re-melting for five times. The evaporation was found to vary between 1.05 and 2.05 wt.%. Then the as-cast ingots were melted and quenched by melt spinning with a copper-wheel speed of $v \approx 30$ m/s. The melt spun ribbons with a width of 2-3 mm and a thickness of 15-25 µm were produced. In order to ensure the phase homogeneity the $Mn_{3-x}Fe_xSn$ compounds were sealed in a quartz tube filled with a high-purity argon atmosphere. Finally, the samples were annealed at 500°C for 2 h and then quenched in cold water.

The crystalline structure and phase composition of the polycrystalline samples were evaluated using powder X-ray diffraction (XRD), electron microscopy (SEM, JEOL JSM 6500 F, Japan) coupled with energy-disperse X-ray spectroscopy (EDS). X-Ray Diffraction (XRD) was carried out on a PANalytical X-Pert PRO diffractometer, using Cu-K_α radiation 1.5405 Å (angular range 10°- 90°, angular step 0.02°, 1 s per step). The samples were placed on a spinner to limit preferential crystalline orientation. Neutron diffraction (ND) experiments were carried out at the research reactor of the TU Delft [60]. A neutron wavelength of 1.67 Å was selected by the (5 3 3) reflection of a germanium single crystal monochromator. The data were collected at temperatures of 5, 80, 250 and 500 K. Refinements of the X-ray and neutron diffraction data were analysed by the Rietveld method [61], as implemented in the Fullprof Suite [62]. The temperature- and field-dependent magnetization was measured with a superconducting quantum interference device (Quantum Design MPMS XL) magnetometer, using the reciprocating sample option mode (RSO), was employed to collect the magnetization in a temperature range from 5 to 370 K with a constant sweep rate of 2 K/min and in applied magnetic fields up to 2 T.

The magnetic hysteresis loops were measured at different temperatures in magnetic fields ranging from -5 T to 5 T. The magnetic measurements at temperatures higher than 370 K were performed in a VersaLab vibrating-sample magnetometer (VSM) with an oven function. Field-oriented samples were embedded in an epoxy glue and oriented with an applied magnetic field of $\mu_0 H = 1$ T in the ferromagnetic state. Prior to orienting in field, the samples were hand milled and then sieved down to a powder size smaller than 10 μm. The transmission ^{57}Fe Mössbauer spectra were collected at different temperatures with a conventional constant-acceleration spectrometer using a ^{57}Co(Rh) source. Velocity calibration was carried out using an α-Fe foil at room temperature. The Mössbauer spectra were fitted using the Mosswinn 4.0 program [63].

Density functional theory (DFT) calculations were carried out with the Vienna *ab initio* simulation package (VASP) [64] using the Perdew-Burke-Ernzerhof (PBE) exchange correlation functional [65,66] and the PAW method [67,68]. The DOS of Mn_2FeSn in the FM state was calculated with fixed hexagonal lattice parameters of $a = 5.57$ Å and $c = 4.45$ Å (cf. Table 7.1). Layers of composition Mn_2Fe were stacked along the c axis and internal coordinates were optimized for the hexagonal symmetry. The kinetic energy cutoff was 270 eV. PAW data sets from the VASP distribution were used with a frozen $[Ne](2s)^2$, [Ar] and [Kr] core for Mn, Fe and Sn, respectively. The DOS was obtained with a Γ-centred $10 \times 10 \times 14$ **k**-point mesh using the tetrahedron method [69].

To establish trends in total energy and net magnetic moment without using supercells, calculations were carried out using the virtual crystal approximation (VCA) with special PAW data sets. These data sets were constructed inspired by the GW-style data sets for Mn and Fe with frozen [Ne] core from the VASP distribution. They interpolate, using fractional charges, between Mn ($Z = 15$ effective core charge) and Fe ($Z = 16$ effective core charge). These were generated for $Z = 15$, 15.3333, 15.6667, 16 keeping these four potentials as similar as possible.

Calculations were done in a primitive hexagonal cells with 8 atoms that were fully optimized (c, a, internal coordinates) observing only symmetry requirements. The kinetic energy cutoff was 600 eV and a Γ-centred $7 \times 7 \times 10$ **k**-point mesh with Methfessel-Paxton smearing of 1th order ($\sigma = 0.1$ eV) was employed [70].

7.3 Results and Discussion

7.3.1 Structural properties

The room-temperature XRD refinements at ambient temperature confirm that the $Mn_{3-x}Fe_xSn$ (x = 0.8-1.4) compounds all crystallize in the Mg_3Cd-type hexagonal structure with space group $P6_3/mmc$ (194). The Mn and Fe atoms share the Wyckoff positions of the $6h$ site, while the Sn atoms occupy the $2c$ site. This result is in agreement with those for other Sn-based Mn_3Sn and Fe_3Sn compounds [14,49,51]. Fig.7.1a shows the Rietveld refinement results for the polycrystalline Mn_2FeSn compound. All of the diffraction peaks marked with their crystal plane index can be identified as the Mg_3Cd-type hexagonal structure with a minor secondary phase. According to literature reports, compounds prepared by traditional arc melting methods show texture [58,59]. However, the compounds prepared by melt-spinning do not exhibit a preferred crystallographic orientation in the Rietveld refinement results.

To identify the impurity phase and examine the microstructure of the $Mn_{3-x}Fe_xSn$ compound, SEM imaging coupled with EDS chemical analyses unveiled coexistence of $Mn_{3-x}Fe_xSn$ and $Mn_{1.75-x}Fe_xSn$ phases in the Mn_2FeSn compound. The insert in Fig.7.1a shows the backscattered electron image of the Mn_2FeSn compound. Obvious contrast can be seen, where the grey region is the Mg_3Cd-type main phase and the light grey area represents the compositional segregation of the Sn-rich phase $Mn_{1.75-x}Fe_xSn$, which is identified as the $Mn_{1.75}Sn$-type hexagonal structure (space group $P6_3/mmc$). This is in good agreement with the results reported by Felez et al. and Liu et al. [14,59]. Furthermore, the grain size and grain boundaries of the compounds are clearly visible in the inset of Fig.7.1a. This is because Sn tends to segregate to grain boundaries [71,72]. It was found that the impurity phase preferentially occupies the grain boundaries. When the grains of the main phase in samples with x = 0.8 and 1.4 are compared, a clear trend can be observed. Specifically, the x = 0.8 sample exhibits a log-normal distribution with an average grain size in the range of 3 - 4 μm. An increase in Fe content to x = 1.4 causes an increase in average grain size to 7 - 8 μm, as shown in Fig. S1 (Supplementary Information). For the grain size evaluation, about 15 SEM images per samples were analysed using the MIPAR software [73] to obtain a quantitative estimate of the average grain size. Compared with other MnNi-X-Y (X = Co, Fe; Y = Sn, In) based Heusler alloys, this grain size is significantly smaller [74–77] and microstructure very different from previous reports.

The weight fractions of the main phase and the impurity phase in the $Mn_{3-x}Fe_xSn$ compounds are shown in Fig. 7.1b and Table 7.1. For $0.8 \leq x \leq 1.4$

the impurity phase was 1-2 wt.%. In our experimental results the ratio of Mn:Fe = 1.6:1.4 is the limit for Mn/Fe substitution at 500 °C. This is because according to the binary Mn-Sn phase diagram the Mn_3Sn phase stable at 500 °C [26] and according to the binary Fe-Sn phase diagram the Fe_3Sn phase is stable in a temperature range of 750-1080 °C [10,52,59]. Meanwhile, it is reasonable to assume that a further increase in the Fe/Mn ratio for the $Mn_{3-x}Fe_xSn$ compounds will lead to an increase in annealing temperature up to 800 °C [10,52]. Fig. 7.1 (c, d) and Table 7.1 shows the refined lattice parameters and the unit-cell volume. By replacing Mn by Fe, the lattice parameters a, c and the unit-cell volume V decrease linearly. In general, Fe substitution for Mn leads to a contraction of the unit cell with a decrease in both hexagonal lattice parameters, due to the fact that the atomic radius of Fe is smaller than that of Mn. The linear continuous change in lattice parameter a and volume V exhibits a kink at the transition from the PM to the FM state as a result of the magneto-volume contribution. In contrast, the lattice parameter c exhibits a linear continuous change, which most likely indicates that the magnetic moments are aligned within the a-b plane at room temperature.

Table 7.1. Lattice parameters a and c, c/a ratio and unit-cell volume V obtained by room-temperature XRD, phase fractions, saturation magnetization M_s and Curie temperature T_C for the $Mn_{3-x}Fe_xSn$ ($0.8 \leq x \leq 1.4$) compounds. M_s is obtained from magnetisation measurements at 5 K and the transition temperatures T_C defined as the minimum in dM/dT in an applied field of 0.01 T.

| x	a (Å)	c (Å)	c/a	V (Å³)	Main wt. (%)	Impurity wt. (%)	$M_{s, 5\,K@5\,T}$ (Am²kg⁻¹)	T_C (K)
0.8	5.58989(7)	4.46896(6)	0.79947(1)	120.933(3)	98.7(6)	1.3(1)	64.27	253
0.9	5.57903(8)	4.46021(7)	0.79946(2)	120.227(3)	98.3(5)	1.7(1)	70.25	272
1.0	5.5695(1)	4.45097(1)	0.79917(2)	119.569(4)	98.2(7)	1.8(1)	76.47	305
1.1	5.56233(7)	4.44581(6)	0.79927(1)	119.123(3)	97.9(5)	2.1(2)	82.64	325
1.2	5.55709(7)	4.43921(6)	0.79884(1)	118.722(3)	97.7(6)	2.3(2)	86.42	351
1.3	5.54841(7)	4.43167(6)	0.79873(1)	118.151(3)	97.9(6)	2.1(2)	92.26	371
1.4	5.5447(1)	4.42473(9)	0.79800(2)	117.811(3)	98.2(7)	1.8(2)	95.48	394
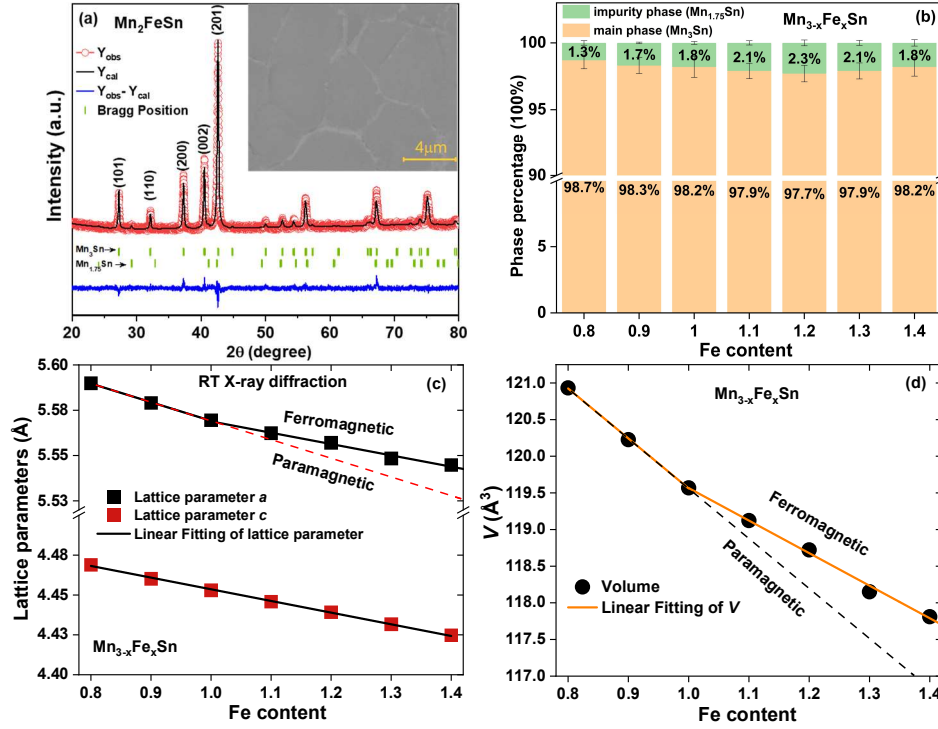
Fig. 7.1. (a) Refined XRD pattern for the Mn$_2$FeSn compound. The insert shows the backscattered electron image of the Mn$_2$FeSn compound. (b) Phase fraction (wt.%) for the Mn$_{3-x}$Fe$_x$Sn alloys. (c) Lattice parameter a and c of (Mn,Fe)$_3$Sn (x = 0.8 -1.4). (d) Unit-cell volume V of (Mn,Fe)$_3$Sn (x = 0.8 -1.4).

7.3.2 Magnetic phase transition

To understand the magnetic properties of the Mn$_{3-x}$Fe$_x$Sn (x = 0.8-1.4) compounds, the temperature dependence of magnetization employing zero-field cooled (ZFC) and field cooled (FC) mode from 5 to 370 K under a magnetic field of 1 T is measured, as shown in Fig. 7.2a. The ZFC (lower curve) and FC (upper curve) magnetization curves for samples with $0.8 \leq x \leq 1.4$ do not overlap at low temperatures, indicating magnetic anisotropy. The M-T curves for heating and cooling coincide without thermal hysteresis. This suggests that these compounds show a second-order phase transition (SOPT) at T_C. Fig. 7.2b shows the FC magnetization vs temperature (M–T) curves recorded at temperatures from 370 to 5 K under an applied field of 0.01 T for Mn$_{3-x}$Fe$_x$Sn (x = 0.8-1.1) compounds, two distinct magnetic transitions were evident in this material system. One transition occurs at higher temperatures, marking the transition from the PM state to the FM state. The Curie temperature defined as the minimum of dM/dT in a field of 0.01T is shown in the insert of Fig. 7.2b. Additionally, a low-temperature

feature is observed in Fig. 7.2b, which indicates a spin reorientation transition or the formation of a complex antiferromagnetic state, which is incompatible with a collinear FM arrangement. This structure can easily evolve into ferromagnetism at intermediate magnetic fields [58,59].
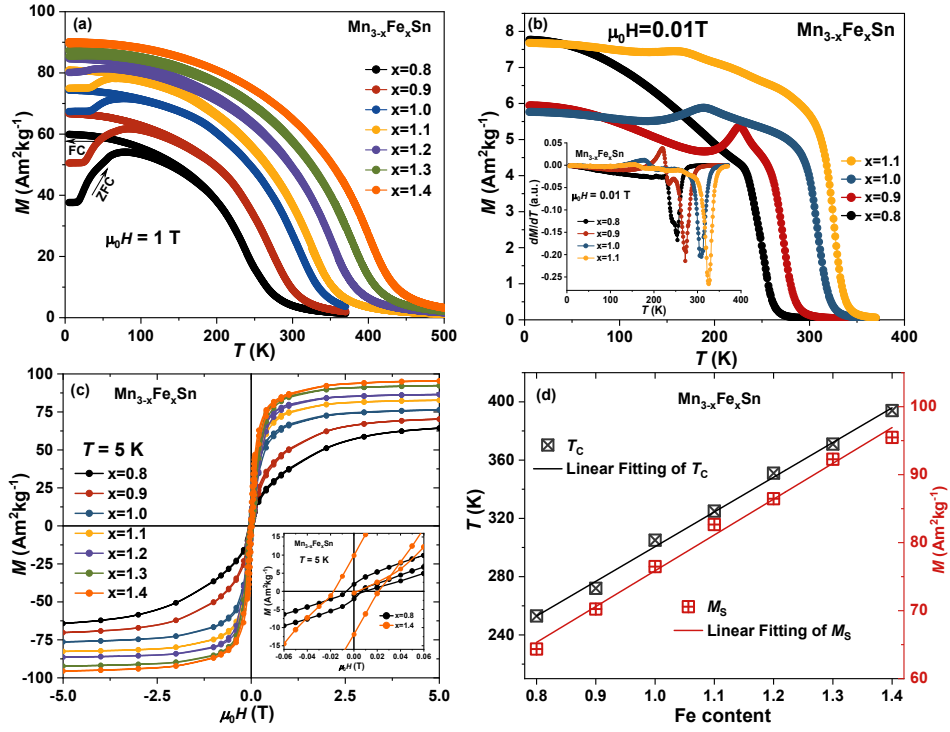
Fig. 7.2. (a) Magnetization as a function of temperature in an applied field of 1 T and (b) Magnetization versus temperature in an applied field of 0.01 T. The insert shows the dM/dT curves in a field of 0.01 T for $x = 0.8$ - 1.1. (c) Magnetization as a function of magnetic field of $Mn_{3-x}Fe_xSn$ ($0.8 \leq x \leq 1.4$) at 5 K. The insert shows a zoomed part of the magnetic hysteresis loop of $Mn_{3-x}Fe_xSn$ ($x = 0.8$ and 1.4). (d) Values of T_C and M_s for the $Mn_{3-x}Fe_xSn$ ($0.8 \leq x \leq 1.4$) compounds as a function of the Fe content.

Fig. 7.2c shows the systematically recorded M-μ_0H magnetization versus magnetic field for the free-powder polycrystalline samples, showing data for the most representative temperature of 5 K. The measurements were performed along 5 quadrants and point towards a soft ferromagnetic behavior with a small magnetic hysteresis loop. For instance, the $x = 1.4$ compound shows the highest coercive field of $\mu_0H_C = 18$ mT and remnant magnetization $M_{rem} = 9.87$ Am^{2}kg^{-1} at 5 K, as shown in the insert of Fig. 7.2c. The magnetic saturation is effectively reached at 2 T for $1.1 \leq x \leq 1.4$. This is in agreement with the field dependent magnetization results reported by Felez et al. [14] for $Mn_{3-x}Fe_xSn$ compounds. One can note that for $x = 0.8$, 0.9 and 1.0 the field-dependent magnetization measurements at 5 K show an ferrimagnetic behaviour without a saturation for

fields up to 5 T. This indicates that the magnetic moments are sizeable and most likely have an antiferromagnetic component. In previous studies of the polycrystalline Mn-Fe-Sn system, the coexistence of FM and AFM phases is not uncommon [58,78–80], which we will discuss in the next section. Fig. 7.2d shows the linear correlation between the saturation magnetization and the transition temperature. In the $Mn_{3-x}Fe_xSn$ ($x = 0.8$-1.4) compounds the transition temperature can be varied continuously in the temperature range from 250 to 396 K by adjusting the Mn/Fe ratio. This satisfies a crucial requirement for the application of MCMs, ensuring that the transition temperature can be adjusted continuously across the temperature range required for magnetic heat pump applications, particularly considering the finite MCE centered around the Curie temperature. As shown in Fig. S7.2 (Supplementary Information) and Table 7.2, the saturation magnetization (M_s) in a field of 7 T for $Mn_{2.2}Fe_{0.8}Sn$ and $Mn_{1.6}Fe_{1.4}Sn$ correspond to 69.96 and 95.98 Am^2kg^{-1}, respectively. These values for the saturation magnetization are comparable to those of most existing MCMs [77,81–83].

The magnetocaloric performance expressed as the isothermal entropy change ΔS is shown in Fig. 7.3a. The isothermal entropy change is calculated by applying the Maxwell relation $\Delta S(T)_{\Delta H} = \int_{Hi}^{Hf} \mu_0 \left(\frac{\partial M(T,H)}{\partial T}\right)_H dH$ [84,85] to the isofield $M(T)$ data. The magnetic or indirect calorimetric determinations of the isothermal entropy change suffer from uncertainties, typically of the order of 10% [86]. The maximum values in isothermal entropy change (ΔS_{max}) measured for the $Mn_{3-x}Fe_xSn$ ($x = 0.8, 1.0, 1.2, 1.4$) compounds are shown in Table 7.2. It is evident that the increase in Fe content from 0.8 to 1.4 results in a 30% enhancement in $|\Delta S_{max}|$, with the maximum value of $|\Delta S_{max}|$ from 1.10 to 1.41 J kg^{-1} K^{-1} for a magnetic field change of 2 T. Unlike first-order phase transition (FOPT) materials, the observed isothermal entropy change is relatively low, which is typical for second-order phase transition (SOPT) materials. To qualitatively evaluate the order of the magnetic phase transition in $Mn_{3-x}Fe_xSn$ materials the field-dependence of the isothermal entropy change with a power law behaviour of the type $|\Delta S| \propto H^n$ is evaluated [87,88]. The field exponent n can be used to classify the nature of the magnetic order: FOPT or SOPT. The field exponent $n = \frac{d \ln(|\Delta S|)}{d \ln(H)}$ for the isothermal entropy change as a function of magnetic field are evaluated. In Fig. 7.3b the high-temperature limit $n \approx 2$ and the low-temperature limit $n \approx 1$ are clearly depicted [89]. When the FM-to-PM phase transition is crossed the minimum value for the exponent corresponds to the value predicted for the SOPT of $n_{min} = 2/3$ and a maximum value of $n_{max} \leqslant 2$ is obtained [89], which is also a characteristic feature for the SOPT. In Fig. 7.3b is clearly seen that field exponent is restricted by the high-temperature value as an upper

limit: $n_{max} < 2$ near T_C. Similar results were obtained for other magnetic field change values. Not only the n_{max} values, but also their temperature evolution, and $n_{min} \approx 2/3$ is typical for materials with a second order phase transition [88]. This is consistent with the absence of thermal hysteresis in the $M(T)$ curves for these materials.
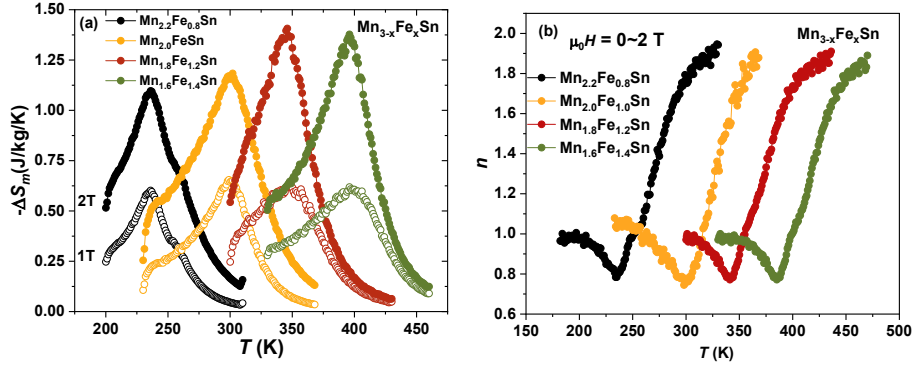
Fig. 7.3. (a) Isothermal entropy change $-\Delta S$ from the temperature-dependent magnetisation $M(T)$ upon heating in a magnetic field change of 1 T (open symbols) and 2 T (closed symbols) for the $Mn_{3-x}Fe_xSn$ ($x = 0.8$-1.4) compounds. (b) Field exponent n of the entropy change for the $Mn_{3-x}Fe_xSn$ ($x = 0.8$-1.4) compounds.

Table 7.2. Calculated $|\Delta S_{max}|$ for $Mn_{3-x}Fe_xSn$ ($x = 0.8, 1.0, 1.2, 1.4$) in a field change of 2 T. The magnetic moment per formula unit derived from the SQUID measurements in a maximum applied magnetic field of $\mu_0H = 7$ T at 5 and 80 K. The magnetic moment per atom of the FM and AFM structures were calculated from neutron powder diffraction data at 5 and 80 K.

x	ΔS_{max} ($Jkg^{-1}K^{-1}$)	$M_{s, 7T}$ (μ_B/f.u.)		FM (μ_B/atom)		AFM (μ_B/atom)	
		5 K	80 K	5 K	80 K	5 K	80 K
0.8	1.10	3.59(1)	3.49(2)	1.29(7)	1.28(7)	2.23(5)	2.11(5)
1.0	1.18	4.02(1)	3.94(1)	1.40(5)	1.37(5)	1.91(3)	1.80(4)
1.2	1.40	4.39(1)	4.33(1)	1.50(6)	1.49(6)	-	-
1.4	1.41	4.77(1)	4.73(1)	1.68(6)	1.65(5)	-	-

7.3.3 Magnetic structure

The spin configurations of intermediate $Mn_{3-x}Fe_xSn$ compositions, probably influenced by the crossover in magnetic behaviour from Mn_3Sn (AFM) to Fe_3Sn (FM), have not been studied as a function of Fe/Mn ratio. While Mn_3Sn shows AFM ordering (with spins within the *a-b* plane) [30], Fe_3Sn exhibits FM ordering (with spins along the *a* axis) [27,52]. In order to qualitatively investigate the evolution of the magnetic structure from AFM to FM order with for an increasing Fe/Mn ratio, we examined a series of representative compositions within the

Mn$_{3-x}$Fe$_x$Sn (x = 0.8, 1.0, 1.2 and 1.4) compounds by powder neutron diffraction (ND) measurements. ND is a powerful technique to investigate the crystalline structure and magnetic properties of materials, with particular sensitivity to the size and orientation of magnetic moments and thereby provide the ability to resolve the magnetic structure. This makes ND an essential tool for studying magnetic materials and investigating magnetic phase transitions. Hence, ND was carried out on Mn$_2$FeSn at five different temperatures (5, 80, 250, 298 and 500 K). These temperatures were selected based on magnetization measurements in a field of 0.01 T. Fig. 7.4a shows a comparison of the ND pattern for the Mn$_2$FeSn compound in the FM+AFM state (5 K), the FM state (250 K) and the PM state (500 K). No additional peaks emerge in the ordered state compared to the disordered state of Mn$_2$FeSn. Therefore, the propagation vector of the magnetic structure corresponds to $\mathbf{k}$ = (0,0,0). From the enhancement of the peak intensity of the (100) and (200) reflections at 5 K it can be deduced that there is a significant magnetic spin component along the c axis, whereas the discernible magnetic contribution of the (002) peak at 250 K indicates a spin alignment within the a-b plane. A symmetry operation analysis of space group 194 (hexagonal $P6_3/mmc$ symmetry) has been performed by BASIREPs (part for Winplotr suite). Table S7.1 (Supplementary Information) presents all possible irreducible representations and the corresponding basis vectors (Φ) for FM and AFM ordering.

The refinement of the ND patterns of Mn$_2$FeSn shown in Fig. 7.4b confirm the hexagonal Mg$_3$Cd-type hexagonal structure with space group $P6_3/mmc$ (194) for Mn$_2$FeSn compound. This is in line with the XRD results. No phase distortion is observed at low temperatures. The initial refinement using the Γ2 irreducible representation assumes a simple ferromagnetic (FM) structure with all magnetic moments aligned along the c axis. However, the poor fitting of the (110) reflection peak suggests that the magnetic structure at 5 K is not a simple ferromagnetic configuration. As show in Fig. S7.2 (Supplementary Information) the macroscopic magnetisation measurements at 5 K reveal a linear magnetisation process below 1 T, without saturation for fields up to 7 T. This behaviour is indicative of the coexistence of FM and AFM contributions. The previous studies, also mentioned a coexistence of FM and AFM contributions, which is a common feature in the Mn-Fe-Sn system [58,78–80]. Therefore, in the final refinement, we included two sets of symmetry operations, Γ2 (FM with moments along the c axis) and Γ8 (AFM with moments in the a-b plane), to achieve a good fit with the data at 5 and 80 K. For the refinements of ND data at 250 K, we employed the irreducible representation Γ10 to describe the FM structure, where the spins are oriented in the a-b plane, as showed in Fig. 7.4b (middle). To validate our hypothesis, we embedded the Mn$_2$FeSn fine powder in

an epoxy and aligned the powder particles using an magnetic field of $\mu_0 H = 1$ T during the curing process. Fig. 7.4c shows room temperature XRD measurements of the Mn_2FeSn compound, comparing the field-oriented powder with free powder samples. As a result of the particle orientation in magnetic field, reflections with a pure a axis component, such as (1 0 0) and (2 0 0), are significantly enhanced. Simultaneously, reflections with a pure c axis component, like (0 0 2), vanish almost completely. This indicates that at room temperature (298 K) the magnetic moments in the Mn_2FeSn compound are aligned within the a-b plane. This observation is consistent with our ND results at 250 K. The hysteresis loops of the field-oriented powders (measured along the field orientation axis) are shown in Fig. 7.4d. At 5 K, the coercive field is $H_C = 25$ mT and the remnant magnetization is $M_{rem} = 5.22$ Am^2kg^{-1}. At 250 K, we observe soft ferromagnetic behaviour characterized by the absence of hysteresis, which is advantageous for MCMs applications. The combined results from ND and oriented powder XRD provide evidence supporting the conclusion that the low-field transition observed at 200 K in the Mn_2FeSn compound corresponds to a spin reorientation transition (T_S). Below T_S, the Mn_2FeSn compound exhibits a coexistence of FM (with spins along the c axis) and AFM (within spins in the a-b plane) components, with combined magnetic moments that are oriented out of the basal plane and tilted towards the c axis, as shown in Fig. 7.5(a-b). Above T_S, the compound displays a ferromagnetic structure aligned within the a-b plane, without any c axis component. Fig. 7.5(a-d) show the refined low-temperature spin structures of $Mn_{3-x}Fe_xSn$ ($x = 0.8$, 1.0, 1.2 and 1.4) compounds at 5 K.
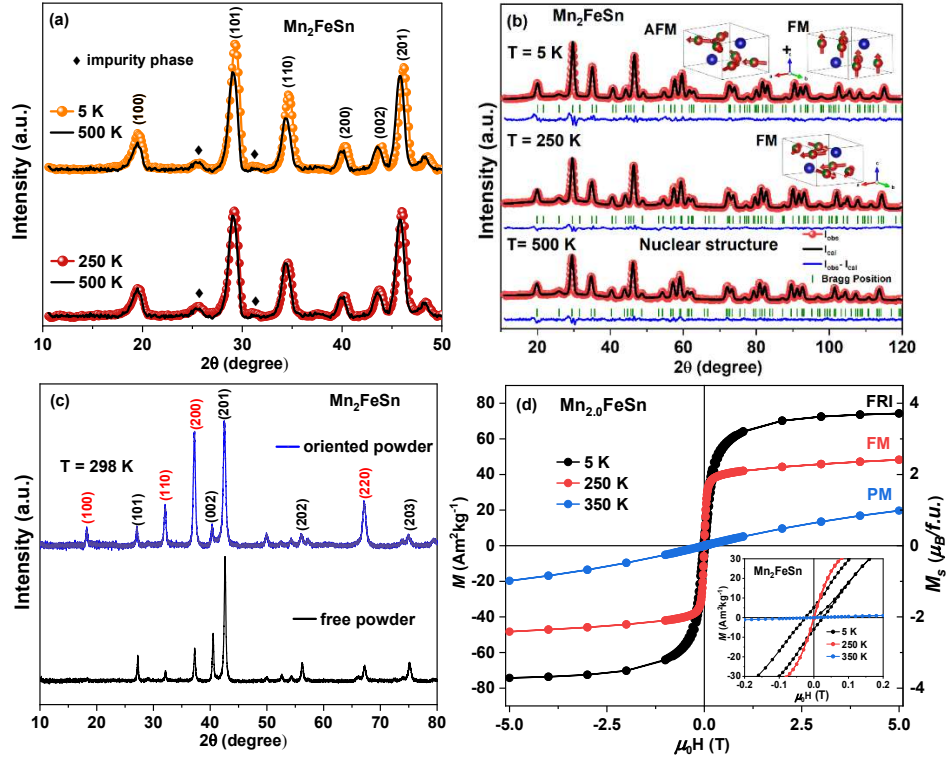
Fig. 7.4. (a) Powder neutron diffraction pattern of the Mn_2FeSn compound obtained at 5, 250 and 500 K. (b) Refinements of the nuclear and magnetic structure. (c) Comparison between random (bottom curve) and oriented powder (top curve) XRD with large changes in the indexed peak intensities. (d) Magnetization as a function of magnetic field for the Mn_2FeSn compound at 5, 250 and 350 K.
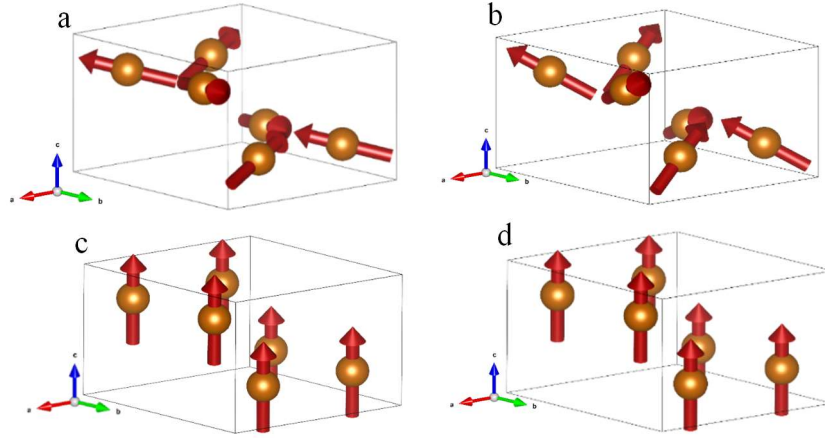
Fig. 7.5. Low-temperature spin structures of $Mn_{3-x}Fe_xSn$ (x = 0.8, 1.0, 1.2 and 1.4) compounds at 5 K. (a) $Mn_{2.2}Fe_{0.8}Sn$, (b) $Mn_{2.0}Fe_{1.0}Sn$, (c) $Mn_{1.8}Fe_{1.2}Sn$ and (d) $Mn_{1.6}Fe_{1.4}Sn$.

109

For the $Mn_{3-x}Fe_xSn$ (x =1.2 and 1.4) compounds ND was carried out at three different temperatures (5, 80 and 500 K). The ND refinement of the $Mn_{1.6}Fe_{1.4}Sn$ pattern is shown in Fig. 7.6a. From the comparison of the FM state and the PM state ND patterns, it is evident that the (100) peak exhibits a noticeable magnetic contribution. The magnetic structure was accurately refined using irreducible representation $\Gamma2$ (FM order with moments along the c axis), which is in good agreement with the magnetisation saturation behaviour observed in Fig. 7.2c. To investigate the nature of the magnetocrystalline anisotropy of $Mn_{1.6}Fe_{1.4}Sn$ compound Fig. 7.6b shows XRD measurements of $Mn_{1.6}Fe_{1.4}Sn$ compound at room temperature for field-oriented powder and free powder samples. It is clearly seen that reflections with a pure a axis component, like (1 0 0) and (2 0 0), are significantly enhanced. Concurrently, reflections with a pure c axis component, like (0 0 2), disappear completely. This indicates that at 298 K, the $Mn_{1.6}Fe_{1.4}Sn$ compound exhibits the same spin structure as Mn_2FeSn, where the a-b plane corresponds to the easy magnetization plane (EMP), while the c axis shows a hard magnetization direction (HMD). The magnetic hysteresis loops of the field-oriented powder (along the field-orientation axis) are shown in Fig. S7.3 (supplementary Information). The coercive field is H_C = 28 mT and the remnant magnetization is M_{rem} = 14.70 Am^{2}kg^{-1} at 5 K.
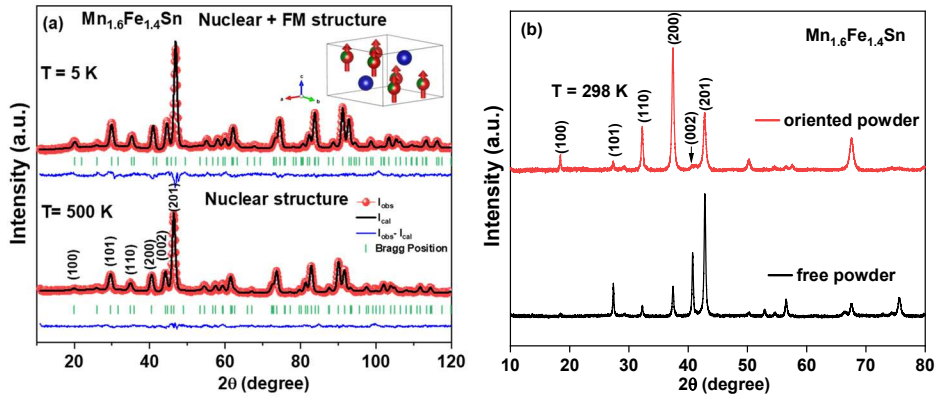
Fig. 7.6. (a) Refinements of the nuclear and magnetic structure of $Mn_{1.6}Fe_{1.4}Sn$ compound. (b) Comparison between random powder (bottom curve) and field oriented powder (top curve) XRD with large changes in the indexed peak intensities.

Fig. 7.7 (a, b) shows the magnetic moment on the 6h site per atom and per formula unit for the FM and AFM components obtained from the ND refinement compared with the SQUID magnetization results for the $Mn_{3-x}Fe_xSn$ (x = 0.8, 1.0, 1.2, 1.4) compounds. From the ND results it is found that magnetic moments of the FM component increase from 1.29(7) μ_B/f.u. (x = 0.8) to 1.68(6) μ_B/f.u. (x = 1.4) for increasing Fe content, as listed in Table 7.2. The ND results for the magnetic moments are comparable with the macroscopic magnetization

results. For $x = 0.8$ and 1.0 the AFM component shows a larger magnetic moment than the FM component. For the $Mn_{2.2}Fe_{0.8}Sn$ compound at 5 K the AFM component displays a magnetic moment of 2.23(5) μ_B/atom, consistent with previous polarized neutron experimental studies of pure Mn_3Sn [78]. It is found that the magnetic moment of the AFM component decreases with the Fe concentration. It should be pointed out that an increasing Fe substitution promotes FM interactions. Fig. 7.7c shows the interatomic distances of the $Mn_{3-x}Fe_xSn$ ($x = 0.8, 1.0, 1.2, 1.4$) compounds obtained from refined ND data at different temperatures. It is clearly shown that the intra-layer distances gradually decrease with the Fe concentration, which is consistent with the trend in lattice parameters. The shortened intra-layer metallic-metallic and metallic-non-metallic distances will strengthen the d-d hybridization among metallic-metallic atoms and the p-d hybridization among metallic-metalloid atoms, due to the increased overlap of electron orbitals [90]. This effect might amplify the magnetic exchange interactions among magnetic atoms. Therefore, the saturation magnetization and the transition temperatures are increasing on increasing Fe contents. Additionally, we observed a significant increase in interatomic distances at high temperature, indicating thermal expansion of the lattice.
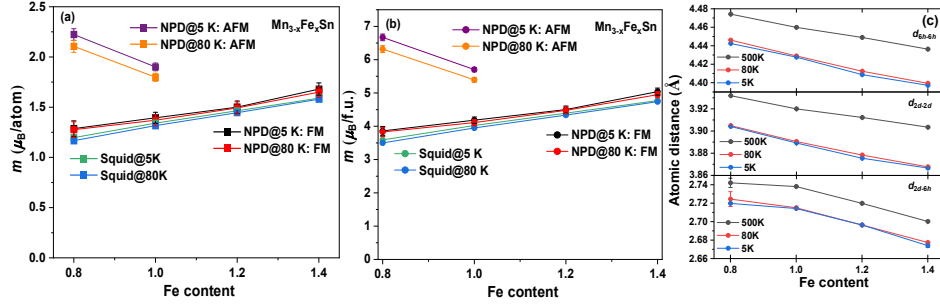
Fig. 7.7. (a) Magnetic moments for $6h$ site in the hexagonal lattice of the $Mn_{3-x}Fe_xSn$ compounds ($x = 0.8, 1.0, 1.2, 1.4$). (b) Saturation magnetization of the $Mn_{3-x}Fe_xSn$ compounds ($x = 0.8, 1.0, 1.2, 1.4$) obtained by neutron diffraction and SQUID magnetization at different temperatures. (c) Interatomic distances of $Mn_{3-x}Fe_xSn$ compounds at different temperatures.

From the ND results we determined the spin structure of the magnetic unit cell in the $Mn_{3-x}Fe_xSn$ ($x = 0.8, 1.0, 1.2, 1.4$) compounds. In order to investigate the magnetic structure in more detail we utilized Mössbauer spectroscopy at varying temperatures. Mössbauer spectroscopy plays a crucial role in investigating structural and magnetic phase transitions in magnetic compounds. Fig. 7.8 displays the Mössbauer spectra of the Mn_2FeSn alloy at different temperatures. A good quality of fit to the experimental data is achieved with single-phase models that exhibit small linewidths (0.3 mm/s) for the $6h$ magnetic site, which

suggests a homogeneous distribution of the magnetic Fe atoms throughout the Mn_2FeSn compound. At 295 K, the spectrum consists of a sextet magnetic sub-spectrum and a quadrupole doublet, which is considered to be the relaxing phase, with a coexistence of the FM state (69%) and the PM state (31%) [52]. This coexistence of FM and PM states is in line with the ND data at 298 K. The temperature dependence of the internal magnetic hyperfine field (B_{hf}) at the 6h site is shown in Fig. 7.9. The compound exhibits $B_{hf} = 20.54$ T at 5 K, which decreases to $B_{hf} = 5.42$ T at 295 K. In contrast, the Fe_3Sn compound shows $B_{hf} = 25.10$ T at the 6h site in the hexagonal lattice at room temperature [52]. In numerous publications, it has been noted that the internal magnetic hyperfine field (B_{hf}) and the magnetic moment (μ_{Fe}) show a proportional relation in many Fe-based compounds [91]. However, a recent study has suggested that the measured magnetic moment may not be the primary factor that defines this proportionality; instead, the contribution of the 3d-moment plays a decisive role. An analysis of the magnetization and the field B_{hf} resulted in a proportionality factor, $P = B_{hf}/\mu_{3d} = 10.37$ T/μ_B [92]. Employing a proportionality factor of 10.37 T/μ_B provides magnetic moments for the Fe (6h) site of about 1.98 μ_{3d}/Fe in the Mn_2FeSn compound. The isomer shift and quadrupole splitting are listed in Table 7.3. The isomer shift decreases with increasing temperature due to the second-order Doppler effect. In the Mn_2FeSn compound, the isomer shift decreases by 0.11 mm/s as the temperature increases from 5 to 295 K. A change in quadrupole splitting from negative to positive values is observed across the spin reorientation. This indicates changes in orientation of the local electric field gradient at the nucleus with respect to the spin direction. This reflects a change in the spin tilt angle across the spin reorientation transition.
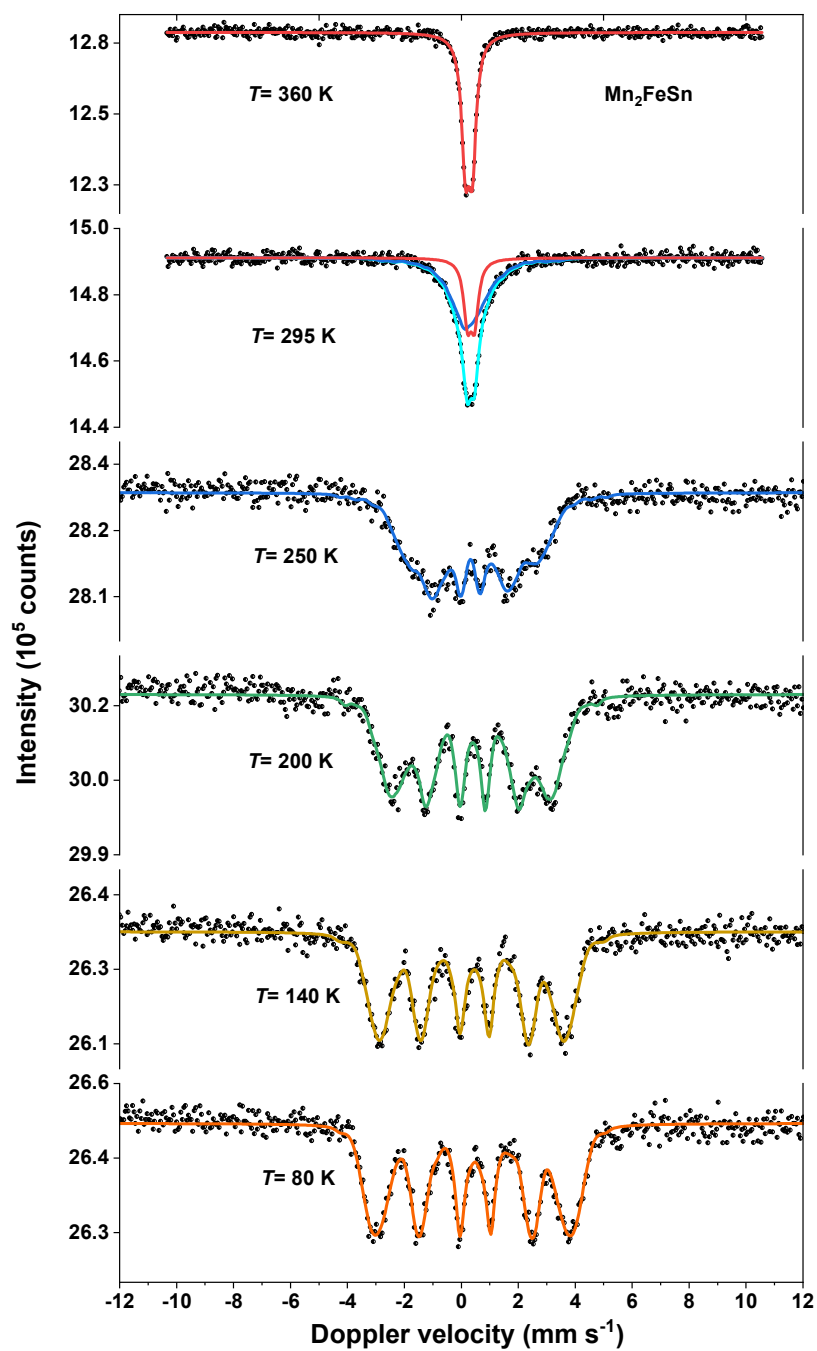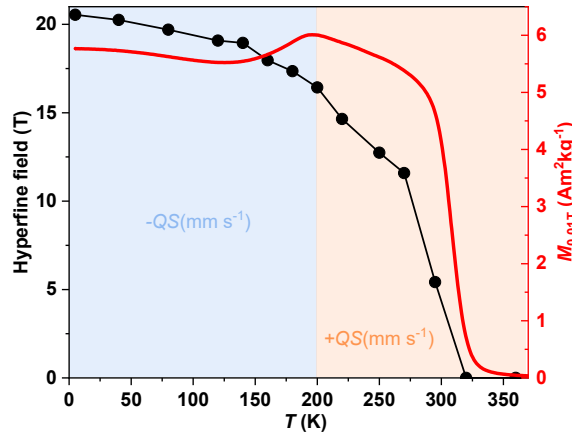
Fig. 7.8. Mössbauer spectra of the Mn_2FeSn compound at 80, 140, 200, 250, 295 and 360 K. The black points represents the experimental data and coloured line is the model fit.

Table 7.3. Fitted Mössbauer parameters of the Mn_2FeSn compound, obtained at different temperatures. Experimental uncertainties: Isomer shift: $IS \pm 0.03$ mm s^{-1}; Quadrupole splitting: $QS \pm 0.03$ mm s^{-1}; Line width: $\Gamma \pm 0.05$ mm s^{-1}; Hyperfine field: $B_{hf} \pm 0.2$ T; Spectral contribution: $\pm 3\%$. FM: ferromagnetic state; PM: paramagnetic state.

Sample	T	IS	QS	Hyperfine field	Γ	Phase
	(K)	(mm s^{-1})	(mm s^{-1})	(T)	(mm s^{-1})	
Mn_2FeSn	5	0.45	-0.09	20.54	0.31	FiM
Mn_2FeSn	40	0.47	-0.08	20.25	0.28	FiM
Mn_2FeSn	80	0.45	-0.09	19.7	0.28	FiM
Mn_2FeSn	120	0.43	-0.09	19.08	0.27	FiM
Mn_2FeSn	140	0.42	-0.10	18.95	0.32	FiM
Mn_2FeSn	160	0.40	-0.12	17.97	0.34	FiM
Mn_2FeSn	180	0.39	-0.08	17.35	0.32	FiM
Mn_2FeSn	200	0.38	-0.06	16.43	0.29	FiM
Mn_2FeSn	220	0.38	0.002	14.65	0.36	FM
Mn_2FeSn	250	0.37	0.12	12.74	0.30	FM
Mn_2FeSn	270	0.37	0.08	11.59	0.33	FM
Mn_2FeSn	295	0.28	0.09	5.42	0.32	FM
Mn_2FeSn	295	0.34	0.25	-	0.32	PM
Mn_2FeSn	320	0.29	0.24	-	0.33	PM
Mn_2FeSn	360	0.26	0.24	-	0.32	PM

Fig. 7.9. Temperature dependence of the hyperfine field B_{hf} of the Mn_2FeSn compound, derived from Mössbauer spectroscopy compared with the low-field magnetisation in a field of 0.01 T.

7.3.4 Electronic and magnetic properties of Mn$_2$FeSn

Recent density functional theory (DFT) studies investigate the structural and magnetic properties of the MnFe$_2$Sn compound for the different phases (cubic, tetragonal and hexagonal) reported experimentally. Daha et al. [11] found that the hexagonal structure with ferromagnetic ordering is most stable [81–83], as it has slightly lower total energy compared to cubic or tetragonal MnFe$_2$Sn. The specific electronic density and local magnetic moments are expected to depend on the Mn/Fe ratio. Density functional theory (DFT) calculations were performed to investigate the magnetic moments in the Mn$_2$FeSn compound. The DOS of FM Mn$_2$FeSn, shown in Fig. 7.9, indicates metallic behavior at the Fermi level for both spin-up and spin-down states. This behavior is primarily attributed to the contribution of the 3d electrons with 2.91 μ_{3d}/Mn atom and 2.13 μ_{3d}/Fe atom, while Sn contributes with only a very weak induced moment. The contributions from the s and p state electrons of Mn and Fe are minimal. The DFT calculations reveal values of 0.008 and 0.007 μ_B for the s and p states of the Mn atoms, and values of -0.011 and -0.004 μ_B for s and p states of the Fe atoms, respectively. Overall, the results indicate total local magnetic moments of 2.92 μ_B for Mn, 2.11 μ_B for Fe, and a weak induced moment of -0.18 μ_B for Sn, which indicates an opposite polarization for Sn with respect to the Mn and Fe atoms. Notably, the magnetic moment of Fe atoms is comparable to the moment estimated from the hyperfine field (B_{hf}) and the proportionality factor resulting in a moment of 1.98 μ_{3d}/Fe.

   To analyze trends with varying composition, virtual crystal approximation (VCA) calculations were carried out for $x = 0$, 1, 2 and 3. Here Mn and Fe are replaced with one effective species (with a fractional core charge). This allows calculations to be performed on primitive hexagonal cells with 8 atoms. According to the calculated DFT energies (per unit cell) with relaxed lattice parameters, as shown in Fig. S7.4a (Supplementary Information), the AFM structure has the lowest energy on the Mn-rich side, consistent with previous experimental results [46,56,93,94]. Introducing Fe atoms enhances the FM interactions in the hexagonal structure, causing the energy of the FM state to gradually stabilize with increasing Fe concentration, which is in good agreement with the present ND results. In the DFT calculations, the energies of the FM and AFM structures are equal at an Fe content of $x = 0.35$. Experimentally we observed the coexistence of FM and AFM magnetic structures up to $x = 1$. The average magnetic moments of FM and AFM structures are plotted in Fig. S7.4b (supplementary Information). A similar trend is observed in the DFT results: the magnetic moment of the AFM structure decreases with increasing Fe content, while the moment of the FM structure increases with increasing Fe content.

Specifically, for the Mn_2FeSn compound, the average magnetic moment (2.46 μ_B/atom) and the effective magnetic moment (2.37(6) μ_B/atom) from the ND results gradually approach each other. However, the VCA calculated average moments are smaller than those calculated for Mn_2FeSn (when VCA is not used). This might point to larger variations in local Mn and Fe moments, depending on the specific coordination.

Table 7.4. ND results and DFT calculation results for the Mn_2FeSn compound with the hexagonal space group $P6_3/mmc$ (194) symmetry for the two different magnetic ordering types with FM and AFM structures.

Material	ND FM (μ_B/atom) 5 K	ND AFM (μ_B/atom) 5 K	ND M_{tot} (μ_B/atom) 5 K	DFT M (μ_B/atom) Mn	DFT M (μ_B/atom) Fe	DFT $M_{average}$ (μ_B/atom)
Mn_2FeSn	1.40(5)	1.91(3)	2.37(6)	2.92	2.11	2.46
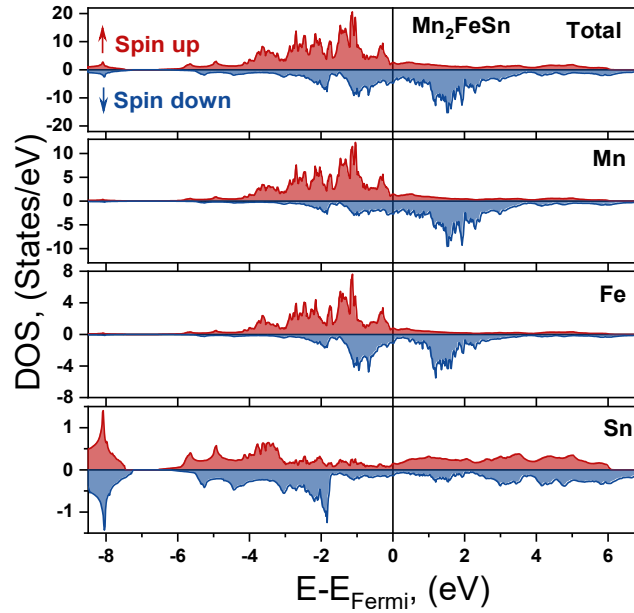
Fig. 7.10. Density of states (DOS) of the FM hexagonal structure obtained from DFT calculations. The vertical line indicates the Fermi level. The DOS of total and individual contributions from Mn, Fe and Sn are as indicated. Positive and negative DOS correspond to the spin up and spin down states, correspondingly.

7.4 Conclusions

A comprehensive study has been performed to investigate the microstructure, spin structure and magnetic properties of $Mn_{3-x}Fe_xSn$ ($x = 0.8$-1.4) polycrystalline samples. In this study we have characterised the phase transition, the nature of the magnetic order, and the magnetocaloric effect of the $Mn_{3-x}Fe_xSn$ compounds. We identified the complex spin configuration of the Mn_2FeSn compound, which depends on temperature. A low-temperature transition at T_S is attributed to a spin reorientation. Below T_S, both ferromagnetic (FM) and antiferromagnetic (AFM) states coexist and are uniformly distributed. Above T_S, the spin structure rearranges into a FM configuration with spins oriented in the a-b plane. However, a new spin model has been derived for the compounds with $x = 1.2$ and 1.4, where a FM component with spins along the c axis shows a spin reorientation into an FM structure with spins in the a-b plane upon crossing T_S. The magnetic properties were evaluated on random and oriented powders, and an easy plane anisotropy was deduced at room temperature. The Curie temperature T_C, determined by the minimum in dM/dT, ranges from 250 K ($x = 0.8$) to 396 K ($x = 1.4$), highlighting its potential applications for magnetic heat pumps and thermal magnetic motors. Applying Maxwell's relationship to assess the isothermal entropy change, it is found that increasing the iron content up to $x = 1.4$ enhances the isothermal entropy change by 30% compared to $x = 0.8$. DFT calculations of the magnetic moments of Mn and Fe in Mn_2FeSn, as well as the trends in average magnetic moment and unit-cell energy with different Fe concentration, are in good agreement with the present experimental results. This demonstrates that DFT calculations are an effective tool to identify the potential of magnetocaloric materials and evaluating their magnetic properties in the Mn-Fe-Sn system.

References

[1] P.J. Shamberger, F.S. Ohuchi, Hysteresis of the martensitic phase transition in magnetocaloric-effect Ni-Mn-Sn alloys, Phys. Rev. B 79 (2009) 144407. https://doi.org/10.1103/PhysRevB.79.144407.

[2] A. Planes, L. Mañosa, M. Acet, Magnetocaloric effect and its relation to shape-memory properties in ferromagnetic Heusler alloys, J. Phys. Condens. Matter 21 (2009) 233201. https://doi.org/10.1088/0953-8984/21/23/233201.

[3] J. Liu, N. Scheerbaum, S. Kauffmann-Weiss, O. Gutfleisch, NiMn-Based Alloys and Composites for Magnetically Controlled Dampers and Actuators, Adv. Eng. Mater. 14 (2012) 653–667. https://doi.org/10.1002/adem.201200038.

[4] I. Takeuchi, O.O. Famodu, J.C. Read, M.A. Aronova, K.-S. Chang, C. Craciunescu, S.E. Lofland, M. Wuttig, F.C. Wellstood, L. Knauss, A. Orozco, Identification of novel compositions of ferromagnetic shape-memory alloys using composition spreads, Nat. Mater. 2 (2003) 180–184. https://doi.org/10.1038/nmat829.

[5] Y. Sutou, Y. Imano, N. Koeda, T. Omori, R. Kainuma, K. Ishida, K. Oikawa, Magnetic and martensitic transformations of NiMnX (X=In, Sn, Sb) ferromagnetic shape memory alloys, Appl. Phys. Lett. 85 (2004) 4358–4360. https://doi.org/10.1063/1.1808879.

[6] H.E. Karaca, I. Karaman, B. Basaran, D.C. Lagoudas, Y.I. Chumlyakov, H.J. Maier, On the stress-assisted magnetic-field-induced phase transformation in Ni_2MnGa ferromagnetic shape memory alloys, Acta Mater. 55 (2007) 4253–4269. https://doi.org/10.1016/j.actamat.2007.03.025.

[7] S. Chadov, X. Qi, J. Kübler, G.H. Fecher, C. Felser, S.C. Zhang, Tunable multifunctional topological insulators in ternary Heusler compounds, Nat. Mater. 9 (2010) 541–545. https://doi.org/10.1038/nmat2770.

[8] R. Weht, W.E. Pickett, Half-metallic ferrimagnetism in Mn_2VAl, Phys. Rev. B 60 (1999) 13006–13010. https://doi.org/10.1103/PhysRevB.60.13006.

[9] G.D. Liu, X.F. Dai, H.Y. Liu, J.L. Chen, Y.X. Li, G. Xiao, G.H. Wu, Mn_2CoZ ($Z =$ Al, Ga, In, Si, Ge, Sn, Sb) compounds: Structural, electronic, and magnetic properties, Phys. Rev. B 77 (2008) 014424. https://doi.org/10.1103/PhysRevB.77.014424.

[10] M. Kratochvílová, D. Král, M. Dušek, J. Valenta, R.H. Colman, O. Heczko, M. Veis, Fe_2MnSn– Experimental quest for predicted Heusler alloy, J. Magn. Magn. Mater. 501 (2020) 166426. https://doi.org/10.1016/j.jmmm.2020.166426.

[11] B. Dahal, A. Al Maruf, S. Prophet, Y. Huh, P.V. Lukashev, P. Kharel, Electronic, magnetic, and structural properties of Fe_2MnSn Heusler alloy, AIP Adv. 10 (2020) 015118. https://doi.org/10.1063/1.5127671.

[12] R. Gauß, O. Gutfleisch, Magnetische Materialien — Schlüsselkomponenten für neue Energietechnologien, in: P. Kausch, J. Matschullat, M. Bertau, H. Mischo (Eds.), Rohst. Ges. Entwickl., Springer Berlin Heidelberg, Berlin, Heidelberg, 2016: pp. 99–118. https://doi.org/10.1007/978-3-662-48855-3_8.

[13] K.P. Skokov, O. Gutfleisch, Heavy rare earth free, free rare earth and rare earth free magnets - Vision and reality, Scr. Mater. 154 (2018) 289–294. https://doi.org/10.1016/j.scriptamat.2018.01.032.

[14] M.R. Felez, A.A. Coelho, S. Gama, Magnetic properties of $Mn_{3-x}Fe_xSn$ compounds with tuneable Curie temperature by Fe content for thermomagnetic motors, J. Magn. Magn. Mater. 444 (2017) 280–283. https://doi.org/10.1016/j.jmmm.2017.08.028.

[15] T. Jungwirth, X. Marti, P. Wadley, J. Wunderlich, Antiferromagnetic spintronics, Nat. Nanotechnol. 11 (2016) 231–241. https://doi.org/10.1038/nnano.2016.18.

[16] K. Yakushiji, K. Saito, S. Mitani, K. Takanashi, Y.K. Takahashi, K. Hono, Current-perpendicular-to-plane magnetoresistance in epitaxial $Co_2MnSi∕$ $Cr∕$ Co_2MnSi trilayers, Appl. Phys. Lett. 88 (2006) 222504. https://doi.org/10.1063/1.2207987.

[17] C. Felser, G.H. Fecher, B. Balke, Spintronics: A Challenge for Materials Science and Solid-State Chemistry, Angew. Chem. Int. Ed. 46 (2007) 668–699. https://doi.org/10.1002/anie.200601815.

[18] A. Karle, The thermomagnetic Curie-motor for the conversion of heat into mechanical energy, Int. J. Therm. Sci. 40 (2001) 834–842. https://doi.org/10.1016/S1290-0729(01)01270-4.

[19] C.S. Alves, F.C. Colman, G.L. Foleiss, G.T.F. Vieira, W. Szpak, Numerical simulation and design of a thermomagnetic motor, Appl. Therm. Eng. 61 (2013) 616–622. https://doi.org/10.1016/j.applthermaleng.2013.07.053.

[20] L.D.R. Ferreira, C.V.X. Bessa, I. Da Silva, S. Gama, A heat transfer study aiming optimization of magnetic heat exchangers of thermomagnetic motors, Int. J. Refrig. 37 (2014) 209–214. https://doi.org/10.1016/j.ijrefrig.2013.09.010.

[21] K. Murakami, M. Nemoto, Some experiments and considerations on the behavior of thermomagnetic motors, IEEE Trans. Magn. 8 (1972) 387–389. https://doi.org/10.1109/TMAG.1972.1067406.

[22] Y. Takahashi, T. Matsuzawa, M. Nishikawa, Fundamental performance of the disc-type thermomagnetic engine, Electr. Eng. Jpn. 148 (2004) 26–33. https://doi.org/10.1002/eej.10359.

[23] C.S. Alves, F.C. Colman, G.L. Foleiss, W. Szpak, G.T.F. Vieira, A.C. Bento, Simulation of solar Curie wheel using NiFe alloy and Gd, Int. J. Refrig. 37 (2014) 215–222. https://doi.org/10.1016/j.ijrefrig.2013.09.031.

[24] Y.W. Yin, M. Raju, W.J. Hu, J.D. Burton, Y.-M. Kim, A.Y. Borisevich, S.J. Pennycook, S.M. Yang, T.W. Noh, A. Gruverman, X.G. Li, Z.D. Zhang, E.Y. Tsymbal, Q. Li, Multiferroic tunnel junctions and ferroelectric control of magnetic state at interface (invited), J. Appl. Phys. 117 (2015) 172601. https://doi.org/10.1063/1.4913753.

[25] E. Krén, J. Paitz, G. Zimmer, É. Zsoldos, Study of the magnetic phase transformation in the Mn_3Sn phase, Phys. BC 80 (1975) 226–230. https://doi.org/10.1016/0378-4363(75)90066-2.

[26] Y. Liu, B. Zhou, C. Wu, H. Peng, J. Wang, X. Su, Experimental Investigation of the Isothermal Section of the Fe-Mn-Sn System at 723 K, J. Phase Equilibria Diffus. 39 (2018) 280–289. https://doi.org/10.1007/s11669-018-0630-7.

[27] B. Fayyazi, K.P. Skokov, T. Faske, I. Opahle, M. Duerrschnabel, T. Helbig, I. Soldatov, U. Rohrmann, L. Molina-Luna, K. Güth, H. Zhang, W. Donner, R. Schäfer, O. Gutfleisch, Experimental and computational analysis of binary Fe-Sn ferromagnetic compounds, Acta Mater. 180 (2019) 126–140. https://doi.org/10.1016/j.actamat.2019.08.054.

[28] B. Fayyazi, K.P. Skokov, T. Faske, D.Y. Karpenkov, W. Donner, O. Gutfleisch, Bulk combinatorial analysis for searching new rare-earth free permanent magnets: Reactive crucible melting applied to the Fe-Sn binary system, Acta Mater. 141 (2017) 434–443. https://doi.org/10.1016/j.actamat.2017.09.036.

[29] M.F.J. Boeije, L. Van Eijck, N.H. Van Dijk, E. Brück, Structural and magnetic properties of hexagonal (Mn,Fe)$_{3-\delta}$Ga, J. Magn. Magn. Mater. 433 (2017) 297–302. https://doi.org/10.1016/j.jmmm.2017.02.058.

[30] N.H. Sung, F. Ronning, J.D. Thompson, E.D. Bauer, Magnetic phase dependence of the anomalous Hall effect in Mn$_3$Sn single crystals, Appl. Phys. Lett. 112 (2018) 132406. https://doi.org/10.1063/1.5021133.

[31] G.J. Zimmer, E. Kren, C.D. Graham, J.J. Rhyne, INVESTIGATION OF THE MAGNETIC PHASE TRANSFORMATION IN Mn$_3$Sn, in: Chicago, IL, USA, 1972: pp. 513–516. https://doi.org/10.1063/1.3699489.

[32] G.J. Zimmer, E. Krén, H.C. Wolfe, C.D. Graham, J.J. Rhyne, Magnetic Structure of DO$_{19}$ Type Compunds, in: AIP Conf. Proc., AIP, Denver, Colorado (USA), 1973: pp. 1379–1383. https://doi.org/10.1063/1.2946799.

[33] H. Ohmori, S. Tomiyoshi, H. Yamauchi, H. Yamamoto, Spin structure and weak ferromagnetism of Mn$_3$Sn, J. Magn. Magn. Mater. 70 (1987) 249–251. https://doi.org/10.1016/0304-8853(87)90427-6.

[34] J. Sticht, K.-H. H ck, J. K bler, Non-collinear itinerant magnetism: the case of Mn$_3$Sn, J. Phys. Condens. Matter 1 (1989) 8155–8176. https://doi.org/10.1088/0953-8984/1/43/016.

[35] P.J. Brown, V. Nunez, F. Tasset, J.B. Forsyth, P. Radhakrishna, Determination of the magnetic structure of Mn$_3$Sn using generalized neutron polarization analysis, J. Phys. Condens. Matter 2 (1990) 9409–9422. https://doi.org/10.1088/0953-8984/2/47/015.

[36] P. Radhakrishna, J.W. Cable, Magnetic excitations in the triangular antiferromagnet Mn$_3$Sn, J. Magn. Magn. Mater. 104–107 (1992) 1065–1066. https://doi.org/10.1016/0304-8853(92)90492-7.

[37] J.W. Cable, N. Wakabayashi, P. Radhakrishna, A neutron study of the magnetic structure of Mn$_3$Sn, Solid State Commun. 88 (1993) 161–166. https://doi.org/10.1016/0038-1098(93)90400-H.

[38] J.W. Cable, N. Wakabayashi, P. Radhakrishna, Magnetic excitations in the triangular antiferromagnets Mn$_3$Sn and Mn$_3$Ge, Phys. Rev. B 48 (1993) 6159–6166. https://doi.org/10.1103/PhysRevB.48.6159.

[39] F. Weitzer, P. Rogl, The Mn-Nd-Sn system (manganese-neodymium-tin), J. Phase Equilibria 14 (1993) 676–681. https://doi.org/10.1007/BF02667879.

[40] W.J. Feng, D. Li, W.J. Ren, Y.B. Li, W.F. Li, J. Li, Y.Q. Zhang, Z.D. Zhang, Glassy ferromagnetism in Ni_3 Sn-type $Mn_{3.1}Sn_{0.9}$, Phys. Rev. B 73 (2006) 205105. https://doi.org/10.1103/PhysRevB.73.205105.

[41] D. Zhang, B. Yan, S.-C. Wu, J. Kübler, G. Kreiner, S.S.P. Parkin, C. Felser, First-principles study of the structural stability of cubic, tetragonal and hexagonal phases in Mn_3 Z (Z=Ga, Sn and Ge) Heusler compounds, J. Phys. Condens. Matter 25 (2013) 206006. https://doi.org/10.1088/0953-8984/25/20/206006.

[42] T.F. Duan, W.J. Ren, W.L. Liu, S.J. Li, W. Liu, Z.D. Zhang, Magnetic anisotropy of single-crystalline Mn_3Sn in triangular and helix-phase states, Appl. Phys. Lett. 107 (2015) 082403. https://doi.org/10.1063/1.4929447.

[43] S. Nakatsuji, N. Kiyohara, T. Higo, Large anomalous Hall effect in a non-collinear antiferromagnet at room temperature, Nature 527 (2015) 212–215. https://doi.org/10.1038/nature15723.

[44] Y. Taguchi, Y. Oohara, H. Yoshizawa, N. Nagaosa, Y. Tokura, Spin Chirality, Berry Phase, and Anomalous Hall Effect in a Frustrated Ferromagnet, Science 291 (2001) 2573–2576. https://doi.org/10.1126/science.1058161.

[45] V. Baltz, A. Manchon, M. Tsoi, T. Moriyama, T. Ono, Y. Tserkovnyak, Antiferromagnetic spintronics, Rev. Mod. Phys. 90 (2018) 015005. https://doi.org/10.1103/RevModPhys.90.015005.

[46] S. Tomiyoshi, Y, Yamaguchi, Magnetic Structure and Weak Ferromagnetism of Mn_3Sn Studied by Polarized Neutron Diffraction, J. Phys. Soc. Jpn. 51 (1982) 2478–2486. https://doi.org/10.1143/JPSJ.51.2478.

[47] M. Singh, S. Bhan, Contribution to the Fe-Sn system, J. Mater. Sci. Lett. 5 (1986) 733–735. https://doi.org/10.1007/BF01730231.

[48] C.W. Pan, M.P. Hung, Y.H. Chang, Magnetic properties of mechanically alloyed Fe_3Sn, Mater. Sci. Eng. A 185 (1994) 147–152. https://doi.org/10.1016/0921-5093(94)90938-5.

[49] B.C. Sales, B. Saparov, M.A. McGuire, D.J. Singh, D.S. Parker, Ferromagnetism of Fe_3Sn and Alloys, Sci. Rep. 4 (2014) 7024. https://doi.org/10.1038/srep07024.

[50] G. Trumpy, E. Both, C. Djéga-Mariadassou, P. Lecocq, Mössbauer-Effect Studies of Iron-Tin Alloys, Phys. Rev. B 2 (1970) 3477–3490. https://doi.org/10.1103/PhysRevB.2.3477.

[51] H. Giefers, M. Nicol, High pressure X-ray diffraction study of all Fe–Sn intermetallic compounds and one Fe–Sn solid solution, J. Alloys Compd. 422 (2006) 132–144. https://doi.org/10.1016/j.jallcom.2005.11.061.

[52] C. Echevarria-Bonet, N. Iglesias, J.S. Garitaonandia, D. Salazar, G.C. Hadjipanayis, J.M. Barandiaran, Structural and magnetic properties of hexagonal Fe_3Sn prepared by non-equilibrium techniques, J. Alloys Compd. 769 (2018) 843–847. https://doi.org/10.1016/j.jallcom.2018.07.257.

[53] O.Yu. Vekilova, B. Fayyazi, K.P. Skokov, O. Gutfleisch, C. Echevarria-Bonet, J.M. Barandiarán, A. Kovacs, J. Fischbacher, T. Schrefl, O. Eriksson, H.C. Herper, Tuning the magnetocrystalline anisotropy of Fe_3Sn by alloying, Phys. Rev. B 99 (2019) 024421. https://doi.org/10.1103/PhysRevB.99.024421.

[54] Y. Song, Y. Hao, S. Wang, J. Zhang, Q. Huang, X. Xing, J. Chen, Complicated magnetic structure and its strong correlation with the anomalous Hall effect in Mn_3Sn, Phys. Rev. B 101 (2020) 144422. https://doi.org/10.1103/PhysRevB.101.144422.

[55] E. Krén, G. Kádár, Neutron diffraction study of Mn_3Ga, Solid State Commun. 8 (1970) 1653–1655. https://doi.org/10.1016/0038-1098(70)90484-9.

[56] S. Tomiyoshi, Polarized Neutron Diffraction Study of the Spin Structure of Mn_3Sn, J. Phys. Soc. Jpn. 51 (1982) 803–810. https://doi.org/10.1143/JPSJ.51.803.

[57] G. Trumpy, E. Both, C. Djéga-Mariadassou, P. Lecocq, Mössbauer-Effect Studies of Iron-Tin Alloys, Phys. Rev. B 2 (1970) 3477–3490. https://doi.org/10.1103/PhysRevB.2.3477.

[58] J. Liu, S. Zuo, X. Zheng, Y. Zhang, T. Zhao, F. Hu, J. Sun, B. Shen, Magnetic transition behavior and large topological Hall effect in hexagonal $Mn_{2-x}Fe_{1+x}Sn$ (x = 0.1) magnet, Appl. Phys. Lett. 117 (2020) 052407. https://doi.org/10.1063/5.0011570.

[59] J. Liu, S.L. Zuo, J. Shen, Y. Zhang, Y. Zhang, Z.X. Li, X.Q. Gao, H.F. Kang, T.Y. Zhao, F.X. Hu, J. Sun, B.G. Shen, Large topological Hall effect and in situ observation of magnetic domain structures in the Mn_2FeSn compound, Mater. Today Phys. 29 (2022) 100871. https://doi.org/10.1016/j.mtphys.2022.100871.

[60] L. Van Eijck, L.D. Cussen, G.J. Sykora, E.M. Schooneveld, N.J. Rhodes, A.A. Van Well, C. Pappas, Design and performance of a novel neutron powder diffractometer: PEARL at TU Delft, J. Appl. Crystallogr. 49 (2016) 1398–1401. https://doi.org/10.1107/S160057671601089X.

[61] H.M. Rietveld, A profile refinement method for nuclear and magnetic structures, J. Appl. Crystallogr. 2 (1969) 65–71. https://doi.org/10.1107/S0021889869006558.

[62] J. Rodríguez-Carvajal, Recent advances in magnetic structure determination by neutron powder diffraction, Phys. B Condens. Matter 192 (1993) 55–69. https://doi.org/10.1016/0921-4526(93)90108-I.

[63] Z. Klencsár, Mössbauer spectrum analysis by Evolution Algorithm, Nucl. Instrum. Methods Phys. Res. B. 129 (1997) 527–533. https://doi.org/10.1016/S0168-583X(97)00314-5.

[64] G. Kresse, J. Furthmüller, Efficient iterative schemes for *ab initio* total-energy calculations using a plane-wave basis set, Phys. Rev. B 54 (1996) 11169–11186. https://doi.org/10.1103/PhysRevB.54.11169.

[65] J.P. Perdew, K. Burke, M. Ernzerhof, Generalized Gradient Approximation Made Simple, Phys. Rev. Lett. 77 (1996) 3865–3868. https://doi.org/10.1103/PhysRevLett.77.3865.

[66] J.P. Perdew, K. Burke, M. Ernzerhof, Generalized Gradient Approximation Made Simple [Phys. Rev. Lett. 77, 3865 (1996)], Phys. Rev. Lett. 78 (1997) 1396–1396. https://doi.org/10.1103/PhysRevLett.78.1396.

[67] M. Methfessel, A.T. Paxton, High-precision sampling for Brillouin-zone integration in metals, Phys. Rev. B 40 (1989) 3616–3621. https://doi.org/10.1103/PhysRevB.40.3616.

[68] G. Kresse, D. Joubert, From ultrasoft pseudopotentials to the projector augmented-wave method, Phys. Rev. B 59 (1999) 1758–1775. https://doi.org/10.1103/PhysRevB.59.1758.

[69] P.E. Blöchl, Projector augmented-wave method, Phys. Rev. B 50 (1994) 17953–17979. https://doi.org/10.1103/PhysRevB.50.17953.

[70] P.E. Blöchl, O. Jepsen, O.K. Andersen, Improved tetrahedron method for Brillouin-zone integrations, Phys. Rev. B 49 (1994) 16223–16233. https://doi.org/10.1103/PhysRevB.49.16223.

[71] L. Cho, M.S. Kim, Y.H. Kim, B.C. De Cooman, Influence of Minor Alloying Elements on Selective Oxidation and Reactive Wetting of CMnSi TRIP Steel during Hot Dip Galvanizing, Metall. Mater. Trans. A 45 (2014) 4484–4498. https://doi.org/10.1007/s11661-014-2394-y.

[72] L. Cho, E.J. Seo, G.S. Jung, D.W. Suh, B.C. De Cooman, Surface Selective Oxidation of Sn-Added CMnSi TRIP Steel, Metall. Mater. Trans. A 47 (2016) 1705–1719. https://doi.org/10.1007/s11661-016-3331-z.

[73] J.M. Sosa, D.E. Huber, B. Welk, H.L. Fraser, Development and application of MIPAR^{TM}: a novel software package for two- and three-dimensional microstructural characterization, Integrating Mater. Manuf. Innov. 3 (2014) 123–140. https://doi.org/10.1186/2193-9772-3-10.

[74] T. Ghosh, S. Agarwal, P.K. Mukhopadhyay, Structural and magnetic properties of $Mn_{50}Fe_{50-x}Sn_x$ (x=10, 15 and 20) alloys, J. Magn. Magn. Mater. 418 (2016) 260–264. https://doi.org/10.1016/j.jmmm.2016.04.022.

[75] Y. Yang, Z. Li, Z. Li, J. Yang, B. Yang, Y. Dong, H. Yan, Y. Zhang, C. Esling, X. Zhao, L. Zuo, Microstructural Feature and Magnetocaloric Effect of $Mn_{50}Ni_{40.5}In_{9.5}$ Melt-Spun Ribbons, Crystals 7 (2017) 289. https://doi.org/10.3390/cryst7100289.

[76] J. Guo, M. Zhong, W. Zhou, Y. Zhang, Z. Wu, Y. Li, J. Zhang, Y. Liu, H. Yang, Grain Size Effect of the γ Phase Precipitation on Martensitic Transformation and Mechanical Properties of Ni–Mn–Sn–Fe Heusler Alloys, Materials 14 (2021) 2339. https://doi.org/10.3390/ma14092339.

[77] F. Zhang, K. Westra, Q. Shen, I. Batashev, A. Kiecana, N. Van Dijk, E. Brück, The second-order magnetic phase transition and magnetocaloric effect in all-d-metal NiCoMnTi-based Heusler alloys, J. Alloys Compd. 906 (2022) 164337. https://doi.org/10.1016/j.jallcom.2022.164337.

[78] T. Hori, H. Niida, Y. Yamaguchi, H. Kato, Y. Nakagawa, Antiferromagnetic to ferromagnetic transition of DO_{19} type $(Mn_{1-x}Fe_x)_3Sn_{1-\delta}$, J. Magn. Magn. Mater. 90–91 (1990) 159–160. https://doi.org/10.1016/S0304-8853(10)80053-8.

[79] X.Q. Zheng, X.P. Shao, J. Chen, Z.Y. Xu, F.X. Hu, J.R. Sun, B.G. Shen, Giant magnetocaloric effect in $Ho_{12}Co_7$ compound, Appl. Phys. Lett. 102 (2013) 022421. https://doi.org/10.1063/1.4788706.

[80] P.K. Rout, P.V.P. Madduri, S.K. Manna, A.K. Nayak, Field-induced topological Hall effect in the noncoplanar triangular antiferromagnetic geometry of Mn_3Sn, Phys. Rev. B 99 (2019) 094430. https://doi.org/10.1103/PhysRevB.99.094430.

[81] T. Gottschall, K.P. Skokov, M. Fries, A. Taubel, I. Radulov, F. Scheibel, D. Benke, S. Riegg, O. Gutfleisch, Making a Cool Choice: The Materials Library of Magnetic Refrigeration, Adv. Energy Mater. 9 (2019) 1901322. https://doi.org/10.1002/aenm.201901322.

[82] W. Hanggai, O. Tegus, H. Yibole, F. Guillou, Structural and magnetic phase diagrams of $MnFe_{0.6}Ni_{0.4}(Si,Ge)$ alloys and their giant magnetocaloric effect probed by heat capacity measurements, J. Magn. Magn. Mater. 494 (2020) 165785. https://doi.org/10.1016/j.jmmm.2019.165785.

[83] H. Ojiyed, M. Van Den Berg, I. Batashev, Q. Shen, N. Van Dijk, E. Brück, Magnetocaloric properties of $Mn_5(Si,P)B_2$ compounds for energy harvesting applications, J. Alloys Compd. 978 (2024) 173485. https://doi.org/10.1016/j.jallcom.2024.173485.

[84] V.K. Pecharsky, K.A. Gschneidner, Jr., Giant Magnetocaloric Effect in $Gd_5(Si_2Ge_2)$, Phys. Rev. Lett. 78 (1997) 4494–4497. https://doi.org/10.1103/PhysRevLett.78.4494.

[85] K.A. GschneidnerJr, V.K. Pecharsky, A.O. Tsokol, Recent developments in magnetocaloric materials, Rep. Prog. Phys. 68 (2005) 1479–1539. https://doi.org/10.1088/0034-4885/68/6/R04.

[86] V.K. Pecharsky, K.A. Gschneidner, Magnetocaloric effect from indirect measurements: Magnetization and heat capacity, J. Appl. Phys. 86 (1999) 565–575. https://doi.org/10.1063/1.370767.

[87] V. Franco, J.S. Blázquez, A. Conde, Field dependence of the magnetocaloric effect in materials with a second order phase transition: A master curve for the magnetic entropy change, Appl. Phys. Lett. 89 (2006) 222512. https://doi.org/10.1063/1.2399361.

[88] J.Y. Law, V. Franco, L.M. Moreno-Ramírez, A. Conde, D.Y. Karpenkov, I. Radulov, K.P. Skokov, O. Gutfleisch, A quantitative criterion for determining the order of magnetic phase transitions using the magnetocaloric effect, Nat. Commun. 9 (2018) 2680. https://doi.org/10.1038/s41467-018-05111-w.

[89] N.H. Van Dijk, Landau model evaluation of the magnetic entropy change in magnetocaloric materials, J. Magn. Magn. Mater. 529 (2021) 167871. https://doi.org/10.1016/j.jmmm.2021.167871.

[90] R.H. Petrucci, General chemistry : principles and modern applications, 10th ed, Pearson Prentice Hall, Toronto, 2010. https://tudelft.on.worldcat.org/oclc/322170391.

[91] O. Eriksson, A. Svane, Isomer shifts and hyperfine fields in iron compounds, J. Phys. Condens. Matter 1 (1989) 1589–1599. https://doi.org/10.1088/0953-8984/1/9/005.

[92] M. Ghafari, H. Hahn, T. Feng, R. Kruk, M. Yan, On the relationship between magnetic moment and nuclear magnetic hyperfine field of ^{57}Fe, Hyperfine Interact. 242 (2021) 2. https://doi.org/10.1007/s10751-021-01725-7.

[93] T. Nagamiya, Triangular Spin Ordering in Mn$_3$Sn and Mn$_3$Ge, J. Phys. Soc. Jpn. 46 (1979) 787–792. https://doi.org/10.1143/JPSJ.46.787.

[94] T. Nagamiya, S. Tomiyoshi, Y. Yamaguchi, Triangular Spin Configuration and Weak Ferromagnetism of Mn$_3$Sn and Mn$_3$Ge, J. Phys. Soc. Jpn. 42 (1982) 385–388. https://doi.org/10.1016/0038-1098(82)90159-4.

Supplementary Material for Chapter 7
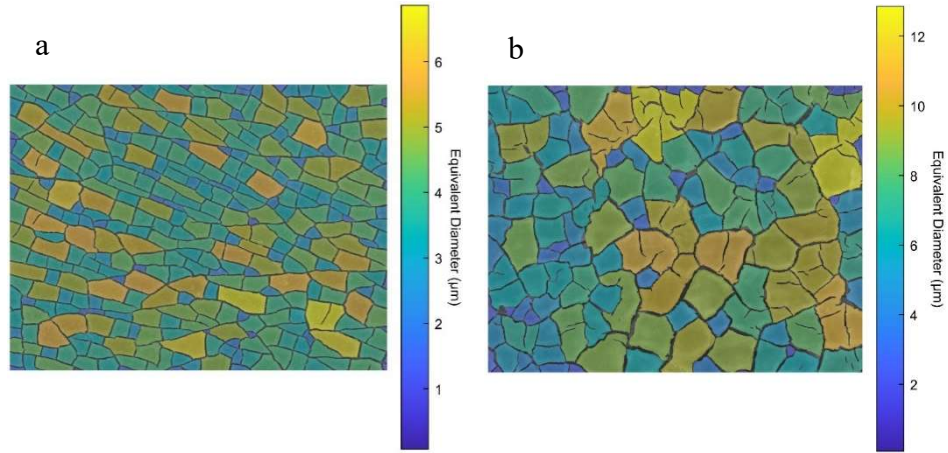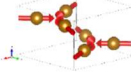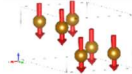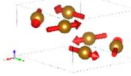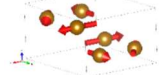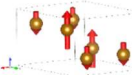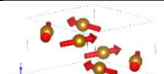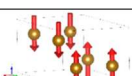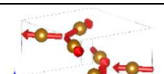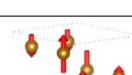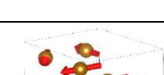
Fig. S7.1. Microstructure of the hexagonal $Mn_{3-x}Fe_xSn$ (x = 0.8 and 1.4) compounds. (a) $Mn_{2.2}Fe_{0.8}Sn$. (b) $Mn_{1.6}Fe_{1.4}Sn$.
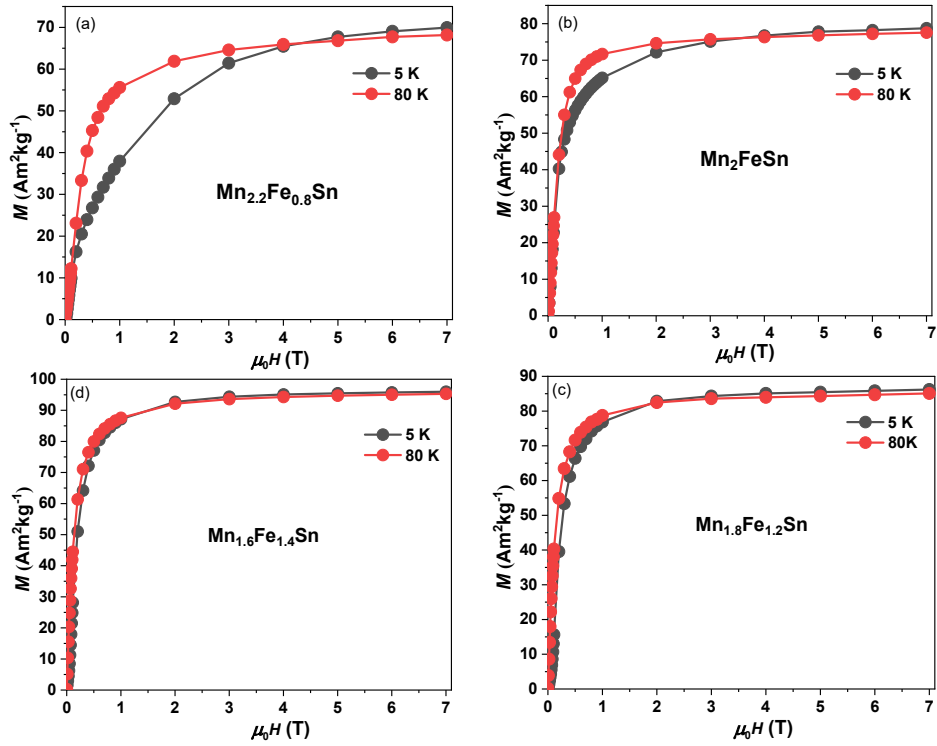
Fig. S7.2. Magnetization as a function of magnetic field for $Mn_{3-x}Fe_xSn$ ($0.8 \leq x \leq 1.4$) at 5 K and 80 K.

Table S7.1. Representational analysis results for space group 194 (hexagonal $P6_3/mmc$ symmetry) with propagation vector **k** = (0,0,0) and one magnetic site at 6*h* given by BASIREPs (part for Winplotr suite). For each symmetry operation the possible magnetic ordering was given: antiferromagnetic (AFM) or ferromagnetic (FM).

Irreducible Representation	Magnetic 6*h* site	
	Φ in *a-b* plane	Φ in *c* axis
Γ_1	AFM (star)	-
Γ_2	-	FM
Γ_3	AFM (spiral)	-
Γ_4	AFM (triangular)	-
Γ_5	-	AFM (layer)
Γ_6	AFM (spiral)	-
Γ_7	-	AFM (layer)
Γ_8	AFM (star)	-
Γ_9	-	AFM (layer)
Γ_{10}	FM	-

Fig. S7.4. Magnetization as a function of magnetic field for the oriented powder $Mn_{1.6}Fe_{1.4}Sn$ compound measured along the easy axis (field oriented direction) at different temperatures.
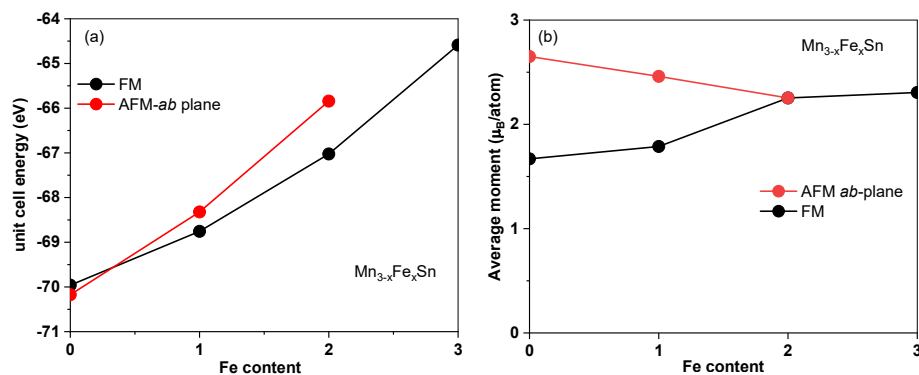
Fig. S7.5. Density functional theory (DFT) calculation results for (a) the unit-cell energy and (b) the magnetic moment per atom as a function of the Fe content x.

Summary

The growing global energy demand and the problem of global warming highlight the need for sustainable and energy-efficient technologies. Magnetic refrigeration offers a promising alternative to traditional compressor-based systems. To meet the Net Zero scenario, 600 million heat pumps must supply 20% of global building heating by 2030. The MCMs are at the heart of such systems, as exemplified by $(Mn,Fe)_2(P,Si)$ alloys, which are cost-effective, rare-earth-free, non-toxic, and feature a tuneable Curie temperature near room temperature. This study also explores novel, eco-friendly material systems, including $YNi_{4-x}Co_xSi$ and $(Mn,Fe)_3Sn$, aiming to achieve a significant magnetocaloric effect near room temperature.

The characterization of latent heat in the first-order magnetic phase transition in giant magnetocaloric Fe-rich $(Mn,Fe)_2(P,Si)$ compounds is presented in **chapter 4**. From an application point of view, to evaluate the MCE for the simultaneous increases in Mn and Si in $(Mn, Fe)_2(P, Si)$ compounds, we employed an indirect calorimetry method to determine both ΔS and ΔT_{ad}. The results demonstrate that the simultaneous increase in Mn and Si concentrations led to a 40% increase in the $|\Delta S|$ value, and a more pronounced ΔT_{hys} at higher concentrations of Mn and Si, indicating a strengthening of the first-order magnetic transition (FOMT). To investigate the underlying mechanisms of latent heat (L) and transformation strain energy (U) associated with the FOMT from a fundamental scientific point of view, we conducted two distinct types of calorimetry measurements that enable a separation of the latent heat and the specific heat, and simultaneously quantify the elastic transformation strain energy by temperature-dependent X-ray diffraction (XRD). The results indicate a direct correlation between latent heat (L) and elastic transformation strain energy (U) in the $(Mn,Fe)_2(P,Si)$ compounds, indicating that the transformation strain energy is the dominant factor for the magnetoelastic coupling. Additionally, the application of an external magnetic field was found to progressively diminish the first-order nature of the transition, with both L and ΔT_{hys} decreasing proportional with field and ultimately vanishing at the critical endpoint of the phase line.

Bridging the gap between microscopic and macroscopic descriptions of the first-order magneto-elastic field-induced transition in $(Mn,Fe)_2(P,Si)$ is studied in **chapter 5**. We have investigated the field-induced transition in the first-order magnetoelastic ferromagnetic transition of a polycrystalline $Mn_{0.60}Fe_{1.30}P_{0.66}Si_{0.34}$ sample. To elucidate the underlying mechanisms linking the microscopic and macroscopic physical properties during this field-induced transition, we conducted a series of comprehensive experiments, including X-ray

magnetic circular dichroism (XMCD) measurements, coupled with simultaneous Hall probe magnetometry, magnetostriction, and bulk SQUID magnetometry. The temperature- and field-induced transitions, measured up to 7 T, reveal the existence of a critical end point at an applied field of 5.2-5.6 T, where the first-order magnetoelastic transition shifts to a supercritical state without hysteresis. The field-dependent XMCD signals obtained from both micro-beams and a macro-beam exhibit significant differences, indicating that the mechanisms governing the field-induced transition are strongly influenced by local conditions, such as grain orientation, variations in chemical composition, and local strain. Our results indicate that a reconstruction based on the sum of micro-beam signals provides a quantitatively representative macro-beam signal that aligns with the macroscopic bulk magnetic properties.

The spin structure, magnetic and magnetocaloric properties of $YNi_{4-x}Co_xSi$ compounds have been studied in **chapter 6**. First of all, our results demonstrate that the ferromagnetic-to-paramagnetic transition is a second-order magnetic phase transition. X-ray diffraction experiments and magnetic measurements on field-oriented polycrystalline materials confirm the presence of relatively strong magneto-crystalline anisotropy for the Co-rich compositions ($x = 3.5$, 3.75 and 4.0), with the the c axis as the easy axis for the magnetisation direction and the a-b plane as the hard magnetic direction. Neutron powder diffraction experiments confirmed a simple ferromagnetic (FM) spin structure aligned with the c axis and a preference of Ni atoms for the $3g$ magnetic site. The magnetic properties are significantly influenced by the Ni/Co ratio. An evident reduction in the mean Co magnetic moment at the $3g$ site, as well as a decrease in saturation magnetization and Curie temperature, was observed with increasing Ni concentrations.

The microstructure, complex spin structure and magnetic properties of Fe doped $Mn_{3-x}Fe_xSn$ have been explored as a potential candidate for room temperature magnetic heat pump application in **chapter 7**. Our results reveal a complex spin configuration in the Mn_2FeSn compound that depends on the temperature. From neutron powder diffraction the low-temperature transition at T_S is attributed to a spin reorientation. Below T_S, both ferromagnetic (FM) and antiferromagnetic (AFM) states coexist and are uniformly distributed. Above T_S, the spin structure transitions to a FM configuration with spins aligned in the a-b plane. For compounds with $x = 1.2$ and 1.4, a spin model was derived, where the FM component with spins along the c axis undergoes a reorientation into a FM structure with spins in the a-b plane upon crossing T_S. Magnetic properties were evaluated in both random and oriented powders, revealing an easy-plane anisotropy at room temperature. The Curie temperature can be tuned within the

130

desired range of 250-396 K by varying the Mn/Fe ratio. DFT calculations of the magnetic moments of Mn and Fe in Mn_2FeSn, as well as the trends in average magnetic moment and unit-cell energy with different Fe concentration, are in good agreement with the present experimental results. From the neutron diffraction (ND) experimental results, we determined that the effective magnetic moment on the 6h site is 2.37(6) μ_B for Mn_2FeSn compounds, which is consistent with DFT calculations that indicate that the average magnetic moment of the Mn and Fe atoms is 2.46 μ_B.

This thesis paves the way for further understanding of GMCE materials that exhibit a first-order magnetic transition (FOMT) and the development of novel MCMs. As observed in Chapters 6 and 7, identifying new promising materials for magnetic heat pump applications remains a challenging task. In fact, these two new systems do not yet rival the performance of the existing giant magnetocaloric effect (GMCE) materials. In contrast, Fe_2P-based materials remain one of the most promising candidates for optimal use in real applications. While the interactions occur at the atomic length scale, there is a lack of investigation at the microscopic scale. Therefore, in this study, we employed XAS/XMCD to examine the magnetic properties at the microscopic scale of the field-induced transition at the Fe K edge, thereby bridging the gap between the microscopic and macroscopic bulk properties.

Samenvatting

De toenemende wereldwijde vraag naar energie en het probleem van de opwarming van de aarde benadrukken de noodzaak voor duurzame en energie-efficiënte technologieën. Magnetische koeling biedt een veelbelovend alternatief voor traditionele compressor-gebaseerde systemen. Om het Net Zero-scenario te bereiken, moeten 600 miljoen warmtepompen tegen 2030 20% van de wereldwijde verwarming van gebouwen leveren. De magnetocalorische materialen (MCM's) zijn het hart van dergelijke systemen, zoals geïllustreerd door (Mn,Fe)$_2$(P,Si) legeringen, die kosteneffectief, zonder zeldzame aardmetalen, niet-toxisch zijn en een instelbare Curie-temperatuur nabij kamertemperatuur hebben. Deze studie verkent ook nieuwe, milieuvriendelijke materiaalsystemen, waaronder YNi$_{4-x}$Co$_x$Si en (Mn,Fe)$_3$Sn, met als doel een significant magnetocalorisch effect nabij kamertemperatuur te bereiken.

De karakterisering van latente warmte in de eerste-orde magnetische faseovergang in de gigantische magnetocalorische Fe-rijke (Mn,Fe)$_2$(P,Si) verbindingen wordt gepresenteerd in **hoofdstuk 4**. Vanuit toepassingsperspectief, om het MCE van de gelijktijdige verhogingen van Mn en Si in (Mn, Fe)$_2$(P, Si) verbindingen te evalueren, hebben we een indirecte calorimetrie-methode toegepast om zowel ΔS als ΔT_{ad} te bepalen. De resultaten toonden aan dat de gelijktijdige verhoging van de concentraties Mn en Si leidde tot een stijging van 40% in de $|\Delta S|$-waarde, en een sterkere ΔT_{hys} bij hogere concentraties van Mn en Si, wat duidt op een versterking van de FOMT. Vanuit fundamenteel wetenschappelijk perspectief, om de onderliggende mechanismen van latente warmte (L) en transformatie-spanningsenergie (U) geassocieerd met de eerste-orde magnetische overgang (FOMT) te onderzoeken, hebben we twee verschillende soorten calorimetrie-metingen uitgevoerd om latente warmte en specifieke warmte afzonderlijk te bepalen, en de elastische transformatie-spanningsenergie gekwantificeerd door temperatuurafhankelijke röntgendiffractie (XRD). Als resultaat werd een directe correlatie tussen latente warmte (L) en elastische transformatie-spanningsenergie (U) vastgesteld in de (Mn, Fe)$_2$(P, Si) verbindingen, wat aangeeft dat transformatie-spanningsenergie de belangrijkste factor is voor de magneto-elastische koppeling. Bovendien bleek de toepassing van een extern magnetisch veld de eerste-orde aard van de overgang geleidelijk te verminderen, waarbij zowel L als ΔT_{hys} proportioneel afnamen en uiteindelijk verdwenen bij het kritische eindpunt.

Het overbruggen van de kloof tussen microscopische en macroscopische beschrijvingen van de eerste-orde magneto-elastische veldgeïnduceerde overgang in (Mn,Fe)$_2$(P,Si) wordt bestudeerd in **hoofdstuk 5**. We hebben de veldgeïnduceerde overgang in de eerste-orde magneto-elastische

ferromagnetische overgang van een polycrystalline $Mn_{0.60}Fe_{1.30}P_{0.66}Si_{0.34}$ monster onderzocht. Om de onderliggende mechanismen te verduidelijken die de microscopische en macroscopische fysische eigenschappen tijdens deze veldgeïnduceerde overgang met elkaar verbinden, hebben we een reeks uitgebreide experimenten uitgevoerd, waaronder metingen van de absorptie van gepolariseerde röntgenstraling, gekoppeld aan gelijktijdige Hall-sonde-magnetometrie, magnetostrictie en bulk SQUID-magnetometrie op de $Mn_{0.60}Fe_{1.30}P_{0.66}Si_{0.34}$ verbinding. De temperatuur- en veldgeïnduceerde overgangen, gemeten tot 7 T, onthullen het bestaan van een kritiek eindpunt bij een aangelegd veld van 5,2–5,6 T, waarbij de eerste-orde magneto-elastische overgang verschuift naar een superkritische toestand zonder hysterese. De veldafhankelijke XMCD-signalen verkregen van zowel micro-bundels als een macro-bundel vertonen aanzienlijke verschillen, wat aangeeft dat de mechanismen die die bepalend zijn voor de veldgeïnduceerde overgang sterk beïnvloed worden door lokale omstandigheden, zoals de oriëntatie van de korrels, variaties in chemische samenstelling en lokale spanning. Onze resultaten geven aan dat de reconstructie op basis van de som van de micro-bundel een kwantitatief representatief macro-bundelsignaal oplevert dat in overeenstemming is met de macroscopische bulk-magnetische eigenschappen.

De spinstructuur, magnetische en magnetocalorische eigenschappen van $YNi_{4-x}Co_xSi$ verbindingen zijn bestudeerd in **hoofdstuk 6**. Ten eerste hebben onze resultaten aangetoond dat de ferromagnetische naar paramagnetische overgang een tweede-orde magnetische faseovergang is. Röntgendiffractie-experimenten en magnetische metingen op veld-georiënteerde polycristallijne materialen bevestigen de aanwezigheid van relatief sterke magneto-kristallijne anisotropie aan de Co-rijke zijde ($x = 3.5$, 3.75 en 4.0), met de c-as als de gemakkelijke as voor de magnetisatie richting en het a-b vlak als de moeilijke magnetische richting. Neutronenpoederdiffractie-experimenten bevestigden dat de eenvoudige FM-spinstructuur uitgelijnd is met de c-as en de voorkeur van Ni-atomen voor de 3g magnetische site. De magnetische eigenschappen worden sterk beïnvloed door de Ni/Co-ratio. Een duidelijke vermindering van het gemiddelde Co-magnetische moment op de 3g-site, evenals een afname van de verzadigingsmagnetisatie en de Curie-temperatuur, werd waargenomen met toenemende Ni-concentraties.

De microstructuur, complexe spinstructuur en magnetische eigenschappen van Fe-gedoopte $Mn_{3-x}Fe_xSn$ zijn onderzocht als een potentiële kandidaat voor toepassingen in warmtepompen op kamertemperatuur in **hoofdstuk 7**. Onze resultaten onthullen een complexe spinconfiguratie in de Mn_2FeSn-verbinding die afhankelijk is van de temperatuur. Neutronenpoederdiffractie bevestigde dat de overgang bij lage temperatuur bij TS wordt toegeschreven aan een spinheroriëntatie. Onder T_S co-existeren zowel ferromagnetische (FM) als antiferromagnetische (AFM) toestanden die gelijkmatig zijn verdeeld. Boven T_S gaat de spinstructuur over naar een FM-configuratie met spins uitgelijnd in het a-b vlak. Voor verbindingen met $x =$

1,2 en 1,4 werd een nieuw spinmodel afgeleid, waarbij de FM-component met spins langs de *c*-as een heroriëntatie ondergaat naar een FM-structuur met spins in het *a-b* vlak bij het overschrijden van T_S. De magnetische eigenschappen werden geëvalueerd in zowel willekeurige als georiënteerde poeders, waarbij een easy-plane anisotropie bij kamertemperatuur werd onthuld. De Curie-temperatuur kan worden aangepast binnen het gewenste bereik van 250-396 K door de Mn/Fe-ratio te variëren. DFT-berekeningen van de magnetische momenten van Mn en Fe in Mn_2FeSn, evenals de trends in het gemiddelde magnetische moment en de eenheidscelenergie bij verschillende Fe-concentraties, komen goed overeen met de huidige experimentele resultaten. Uit neutronendiffractie (ND) experimenten bepaalden we dat het effectieve magnetische moment op de 6*h* site 2.37(6) μ_B is voor Mn_2FeSn verbindingen, wat in overeenstemming is met de DFT-berekeningen die suggereren dat het gemiddelde magnetische moment van de Mn- en Fe-atomen 2.46 μ_B is.

Dit proefschrift baant de weg voor een dieper begrip van GMCE-materialen die een eerstegraads magnetische overgang (FOMT) vertonen, evenals voor de ontwikkeling van nieuwe magnetocalorische materialen (MCM's). Zoals besproken in hoofdstukken 6 en 7, blijft het identificeren van veelbelovende nieuwe materialen voor toepassingen in magnetische warmtepompen een uitdagende taak. Deze twee nieuwe systemen evenaren momenteel nog niet de prestaties van de bestaande materialen met een gigantisch magnetocalorisch effect (GMCE). Daarentegen blijven op Fe_2P gebaseerde materialen tot de meest veelbelovende kandidaten behoren voor optimaal gebruik in praktische toepassingen. Hoewel de interacties plaatsvinden op een atomaire lengteschaal, is er een gebrek aan onderzoek op microscopisch niveau. Daarom hebben we in deze studie gebruikgemaakt van XAS/XMCD om de magnetische eigenschappen op microscopische schaal van de veld-geïnduceerde overgang aan de Fe *K*-edge te onderzoeken, en zo de kloof te overbruggen tussen de microscopische eigenschappen en de macroscopische bulkgedragingen.

Acknowledgements

My PhD journey, which has spanned four years, is now approaching its conclusion. Looking back, I began my PhD during the pandemic, arriving in the Netherlands on December 7, 2020, with both excitement for the unknown and anticipation for a completely new experience. However, the transition was far from easy. In my first year, due to the lockdown of COVID-19, I struggled to adapt to the online systems and overcome the language barrier, making the adjustment particularly challenging for me during that period. After a full year, everything gradually returned to normal, allowing me to accelerate my progress to complete this thesis. Here, I would like to take this opportunity to sincerely thank everyone who has supported and inspired me during my time in Delft. Their guidance and encouragement have been invaluable, and this work would not have been possible without their contributions.

First of all, I would like to sincerely thank my supervisor, **Prof. Dr. Niels van Dijk**, for giving me the opportunity to pursue my PhD in the FAME group. Since our first meeting in September 2019 at IMNU in Hohhot, it was a natural decision for me to continue my PhD under your guidance. I have to say thanks for your one-minute interview at IMNU. When I handed you a printed copy of my first JMMM paper, you asked me to summarize its key highlights within one minute. Despite my best efforts, I couldn't complete it in time. That experience taught me the importance of always being prepared to deliver a concise summary of my work. After you returned to the Netherlands, you sent me an email summarizing the key highlights of my work from your perspective. Your passion, enthusiasm, and sense of responsibility were truly inspiring and left a lasting impression on me. Finally, in December 2020, I joined your group as the youngest PhD candidate. I have really enjoyed working with you, especially during my first year PhD when you offered me six individual lectures on the theory of magnetism. Those lectures were invaluable and had a profound impact on my understanding and academic growth. Thank you for introducing me to synchrotron and neutron techniques. Apologies, I was a "tourist" at that time (June 2022). Since then, I've learned that being a "tourist" once in my life is enough. Your insightful thinking consistently encouraged me to dive deeper into scientific questions, rather than merely scratching the surface. My own research interests have evolved, greatly influenced by your extensive research experience. I gained a lot from every discussion with you, as your explanations provided perspectives that I had not seen before. Especially when I was struggling to identify new types of MCMs (279 samples), you reminded me that thinking deeply is more important than simply working hard. Without this advice, I would not have reached this point, and I will carry it with me forever. Moreover, apart from scientific research, you also shared stories of Europe and the Netherlands with me. The trip exploration of Amsterdam remains a cherished memory. Thanks for showing us new land and new life in Amsterdam, and thanks both you and your girlfriend **Cécile**.

I would like to address my special thanks to my co-supervisor **Prof. Dr. Ekkes Brück** for having accepted me as PhD candidate in your group. Your extensive knowledge, open-mindedness, patience, and scientific optimism make you an exceptional supervisor and famous in MCE field. I am deeply grateful for the comments and discussions we have had. Your unwavering support, encouragement, and highly supportive attitude have given me the confidence to overcome any challenges I encountered along the way. Thanks for offering me the opportunity to attend excellent international conferences, which have helped me develop my network in the field. Especially after my first publication, you told

136

Katja Garina, **Yueer Li**, **Lassi Tiihonen** for sharing their research and for the pleasant and insightful conversations we've had.

I also would like to express my sincere gratitude to the students I have supervised: **Jomi Baggerman**, **Cas Hahnraths**, **Tim**, **Duran Açikel**, **Tomas Paquot**. Working with each of you in exploring new MCE materials has been both a joyful and deeply rewarding experience. Your dedication and hard work throughout the research process and the remarkable progress you achieved by the time of your graduation have filled me with pride and excitement for your future endeavors. I am truly grateful for the opportunity to collaborate with you and will always cherish the memories of our time together. Each of you has made a lasting impact on my approach to both teaching and research, and I have no doubt that your future accomplishments will continue to inspire those around you.

My sincere thanks go to my colleagues in the MCE group. A special thanks to **Diego Pineda Quijano**, who worked on a different research direction but always generously shared his insights during group meetings. I truly appreciate all the simulation results you provided. It was also a great experience traveling to Bielefeld for MCE workshop with you. I am also thankful to **Anika Kiecana**, **Qi Shen** for their help with SEM/EDS measurements, **Giovanni**, **Brammert**, **Stijn**, **Maarten**, **Ivan**, **Fengqi**, **Ziying**, **Xinmin**, **Justin**, **Wouter**, **Nassim**, **Yorick**, **Floris**, **Annika** and **Defang** for the great experience of working together as a team. Thanks to **Øyvind** for the great experiments we have had at ESRF last year and for the insightful scientific discussions we shared throughout. **Ilse** and **Nicole**, thank you for your support. Every conference attendance and communication with HR wouldn't have been possible without your assistance. I also want to express my gratitude to **Jan Leen Kloosterman**, **Wim Bouwman**, **Stephan Eijt**, **Henk Schut** and **Anna Smith**. I feel honoured to have spent time with you during my academic journey. I am also deeply thankful for the friendly moments and enjoyable interactions shared with Dr. **Jouke Heringa**, **Ben Harrison**, Dr. **Martijn de Boer**, Dr. **Michel Thijs**, Dr. **Swapna Ganapathy**, **Indu Dhiman**, **Tom McCoy**, **Maik Butterling**, **Frans Ooms**, **Fan Chao**, **Shengnan Zhang**, **Zhu Cheng**, **Xavier Kouoi**, **Chenglong Zhao**, **Qidi Wang**, **Zhaolong Li**, **Xuehang Wang**, **Hao Wang**. Thank you all for being part of my journey and for making it a truly memorable and rewarding experience.

Furthermore, I would like to thank the members of my doctoral graduation committee: Prof. **Nora Dempsey**, Prof. **Katia Pappas**, Prof. **Mina Shahi** and Prof. **Maria Santofimia** for their time, interest and helpful comments.

I would like to sincerely thank my master's supervisor, Prof. **Tegus**, for guiding me into the field of magnetocaloric research and for being a source of unwavering guidance throughout my academic journey. Your mentorship has enriched me not only with academic knowledge but also with a life philosophy that will stay with me long into the future. I also extend my warmest thanks to your wife, **Dagula**, whose kindness and support brought me a comforting sense of home during my time away from my own family.

I want to express my sincere gratitude to my friend Dr. **Hamutu** for the wonderful experience of working together over the past seven years, I have learned a lot from you. Thank you so much for picking me up from Schiphol Airport when I first arrived—it meant a lot to me. We shared the same office for three years and lived in the same apartment for a year, during which we had many enjoyable moments, from discussing academic questions to sharing everyday life experiences. I'm also grateful to your

girlfriend, **Uyinga**, for the warm invitation to Wageningen. **Yiliqi** and **Narsu**, thank you for welcoming us into your home to celebrate the Christmas. Narisu's culinary skills and talent for photography are truly impressive, and thanks to you, we were able to enjoy delicious food and capture many beautiful moments together. **Darkhan**, **Virgilio**, **Suye**, **Tala**, **Gandir** and **Habur**, the time spent with you has always been filled with joy and laughter. Wishing all of you a bright and wonderful future ahead. **Francisco** and **Cony** you are among my dear international friends—thank you so much for the invitation and for coming to our home to celebrate Christmas together. I also really appreciate the lovely activities you organized for us to explore Delft. Wishing you all the best with your research. **Lijuan** and **Wieles** every conversation with you has been relaxed and enjoyable. I wish you both a bright and successful career ahead. **Baljinnyam** and **Jula**, thank you for always being so welcoming. I really appreciate you teaching me how to drive in the Netherlands. Wishing your family filled with happiness and joy, and may your son, **Tomoo**, grow up strong, healthy, and full of promise.

This special paragraph is dedicated to my beloved family for their unwavering love, support, and encouragement. I am especially deeply indebted to my **parents**, who raised me with love and instilled in me the confidence to believe in myself and face every challenge with courage. Thanks to my sister **Hairhan** and her family for their selfless support over the years and for taking care of our parents, allowing me to pursue my dreams without worry. To my beloved nephews, **Biligbadar** and **Turbadar**, you are the first of the next generation in our family and your arrival has brought us endless joy. May you grow up strong, healthy, and full of promise. Last, but certainly not least, my most beloved thanks to my girlfriend **Urlige** who has always stood by me and shared with me both the great and the difficult moments. As we journey through life together, I look forward to a bright future filled with shared dreams, support and cherished memories. Your presence brings joy and meaning to my life. Thanks a lot for your effort.

Please accept my thanks to everyone who has been part of my life!

Hanggai

March 2025

List of Publications

Publications related to the PhD study

[1]. **W. Hanggai**, N.H. van Dijk, E. Brück, *Structural and magnetic properties of $YNi_{4-x}Co_xSi$ alloys*, Journal of Alloys and Compounds 986 (2024) 174116.

[2]. **W. Hanggai**, O. Hamutu, G.A. de Wijs, I. Dugulan, N.H. van Dijk, E. Brück, *Complex Spin Structure and Magnetic Phase Transition of $Mn_{3-x}Fe_xSn$ Alloys*, under review.

[3]. **W. Hanggai**, H. Yibole, F. Guillou, C. Kwakernaak, N.H. van Dijk, E. Brück, *Preparation of Fe-rich giant magnetocaloric $(Mn,Fe)_2(P,Si)$ ribbons and calorimetric analysis of the first-order magnetic transition*, under review.

[4]. **W. Hanggai**, Ø. Rørbakken, A. Aubert, K. Skokov, F. Guillou, H. Yibole, A. Rogalev, F. Wilhelm, N.H. van Dijk, E. Brück, *Bridging the gap between micro- and macroscopic descriptions of 1st-order magneto-elastic field induced transitions*, in preparation.

[5]. **W. Hanggai**, Ø. Rørbakken, B. Suye, N.H. van Dijk, E. Brück, *Evolution of n_{max} with applied magnetic field and estimation of the critical end point in $(Mn,Fe)_2(P,Si)$ compounds*, in preparation.

[6]. B. Nuendute, **W. Hanggai**, H. Yibole, B. Tana, O. Tegus, F. Guillou, *Drastic Influence of Synthesis Conditions on Structural, Magnetic, and Magnetocaloric Properties of $Mn(Fe,Ni)(Si,Al)$ Compounds*, Crystals 2022, 12, 233.

[7]. H. Yibole, B. Lingling-Bao, J.Y. Xu, H. Alata, O. Tegus, **W. Hanggai**, N.H. van Dijk, E. Brück, F. Guillou, *$(Fe,Co)_2(P,Si)$ rare-earth free permanent magnets: From macroscopic single crystals to submicron-sized particles*, Acta Materialia 221 (2021) 117388.

[8]. H. Yibole, L. Shanshan, B. Narsu, F. Guillou, B. Detlefs, P. Glatzel, **W. Hanggai**, A. Kiecana, N.H. van Dijk, E. Brück, *Magnetic moments and electronic structure evolution in $(Mn,Fe)_2(P,Si)$ single crystals from X-ray emission spectroscopy*, under review.

Publications related to the Master study

[1]. **W. Hanggai**, O. Tegus, H. Yibole, F. Guillou, *Structural and magnetic phase diagrams of MnFe$_{0.6}$Ni$_{0.4}$(Si,Ge) alloys and their giant magnetocaloric effect probed by heat capacity measurements*, Journal of Magnetism and Magnetic Materials 494 (2020) 165785.

[2]. **W. Hanggai**, O. Tegus, H. Yibole, F. Guillou, Z.Q. Ou, *Effects of Fe Doping on Structural and Magnetic Properties of MnFe$_x$Ni$_{1-x}$Si Alloy*, Journal of Inner Mongolia Normal University 02 (2019) 001.

[3]. H. Yibole, **W. Hanggai**, Z.Q. Ou, R. Hamane, V. Hardy, F. Guillou. *Magnetic properties, anisotropy parameters and magnetocaloric effect of flux grown MnFe$_4$Si$_3$ single crystal*, Journal of Magnetism and Magnetic Materials 504 (2020) 166597.

Conference presentations

1. Oral presentation: **W.Hanggai**, N.H. van Dijk, E. Brück, *et al.* "Magnetic properties and calorimetric measurements of the FOMT in giant magnetocaloric (Mn,Fe)$_2$(P,Si)", 2025 IEEE Conference on Advances in Magnetics (AIM 2025).

2. Poster presentation: **W.Hanggai**, N.H. van Dijk, E. Brück, *et al.* "Giant magnetocaloric materials (Mn,Fe)$_{1.9}$(P,Si) for application in magnetic heat pumps", Dresden Days on Magnetocalorics 2023.

3. Oral presentation: **W.Hanggai**, N.H. van Dijk, E. Brück, *et al.* "Synthesis of Room Temperature Magnetocaloric (Mn,Fe)$_{1.9}$(P,Si) Compounds by Melt Spinning", 24th International Conference on Solid Compounds of Transition Elements (SCTE 2024).

4. Poster presentation: **W.Hanggai**, N.H. van Dijk, E. Brück, *et al.* "Magnetic Structural and Magnetic Properties of Hexagonal Mn$_{3-x}$Fe$_x$Sn Prepared by Melt-Spun Techniques", 13th Joint European Magnetic Symposia (JEMS 2023).

5. Oral presentation: **W.Hanggai**, N.H. van Dijk, E. Brück, *et al.* "Microstructure and Micromagnetic Properties of Magnetocaloric Materials (Mn,Fe)$_{1.9}$(P,Si)" 10th IIR International Conference on Caloric Cooling and Applications of Caloric Materials (THERMAG 2024).

6. Poster presentation: **W.Hanggai**, N.H. van Dijk, E. Brück, *et al.* "Optimization in Room Temperature Magnetocaloric Materials (MnFe)$_{1.9}$(PSi) Fe-Rich Compounds", 12th Joint European Magnetic Symposia (JEMS 2022).

7. Oral presentation: **W.Hanggai**, Niels. van Dijk, Ekkes. Brück, *et al.* "Separation of the Latent Heat Associated with the First-Order Magnetic Transition in Giant Magnetocaloric (Mn,Fe)$_2$(P,Si) Compounds", 2024 MCE workshop at Bielefeld university.

8. Poster presentation: **W.Hanggai**, N.H. van Dijk, E. Brück, *et al.* "Exploration of new magnetocaloric materials Y(Ni,Co)$_4$Si for application in magnetic heat pumps, NOW Physics, the Netherlands, 2023.

Curriculum Vitae

Hanggai, born on 29 June 1995 in Inner Mongolia, China. From 2013 to 2017, he pursued his B.Sc. studies in physics at the College of Physics and Electronic Information of Inner Mongolia Normal University. He was honored as outstanding graduate student for his graduation in 2017. In the same year, he started his master in Condensed Matter Physics in the same university. He obtained his M.Sc. in 2020 after completing the thesis entitled "Phase transition and magnetic properties of transition metal-based first-order phase transition materials" under the supervision of Prof. dr. O. Tegus.

Motivated by a growing interest in functional materials, he began his PhD research on magnetocaloric materials in December 2020 under the supervision of Prof. Dr. E. Brück and Prof. Dr. N. H. van Dijk, within the Fundamental Aspects of Materials and Energy (FAME) section of the Department of Radiation Science and Technology at Delft University of Technology, Delft, the Netherlands. His PhD research focused on the development of tailored magnetocaloric materials for application in magnetic heat pump systems. The outcomes of this research are presented in this thesis and have also been disseminated through several publications in international peer-reviewed journals.